UNIVERSITY OF CALIFORNIA
SANTA CRUZ

CHARACTERIZATION OF THE BACKGROUND DUE TO LEPTON SCATTERING TO THE $\chi^{\pm} \to \chi^{0}\,\pi^{\pm}$ DISAPPEARING TRACK SIGNATURE WITH THE ATLAS DETECTOR AT THE LHC

A dissertation submitted in partial satisfaction of the
requirements for the degree of

DOCTOR OF PHILOSOPHY

in

PHYSICS

by

Maxwell C. Baugh

December 2019

The Dissertation of Maxwell C. Baugh
is approved:

Professor Bruce Schumm, Chair

Professor Jason Nielsen

Professor Michael Hance

Quentin Williams
Acting Vice Provost and Dean of Graduate Studies

Table of Contents

List of Figures

List of Tables

Abstract

Characterization of the Background due to Lepton Scattering to the $\chi^{\pm} \to \chi^0 \pi^{\pm}$ Disappearing Track Signature with the ATLAS Detector at the LHC

by

Maxwell C. Baugh

Supersymmetry models in which the lightest particle is pure-wino or pure-higgsino have chargino next-to-lightest-particles (NLSP) nearly mass-degenerate with the lightest neutralino, resulting in a lifetime long enough to produce hits in the Pixel Detector but not long enough to produce a full track; this is called the "disappearing track signature". Electrons and muons which traverse the Pixel Detector and Coulomb scatter at a steep angle and therefore fail to be reconstructed as electrons or muons are a significant background to this signature; this is the "lepton scatter background". This lepton scatter background was characterized using $36\,\mathrm{fb}^{-1}$ of integrated luminosity of proton-proton collisions at $\sqrt{s} = 13\,\mathrm{TeV}$ center-of-mass energy in the ATLAS Detector. Electrons were found to dominate at lower transverse momentum whereas at above about $100\,\mathrm{GeV}$ the contributions are similar. Comparison with a representative pure-wino Monte Carlo model suggests a minimum threshold of $p_T > 100\,\mathrm{GeV}$ should be used in the full analysis.

To Friends, Family, and the Future

Acknowledgments

There are many people I would like to thank, for a variety of reasons.

First of all I would like to thank my advisor Bruce Schumm for advising me through the PhD program at UCSC. In the same vein, I would like to thank the Committee members Jason Nielsen and Mike Hance for general guidance working in ATLAS and for helping to significantly improve the quality of this dissertation. Rounding out the explicit research acknowledgements, Matthew Gignac has been a tremendous help with this analysis, this work would not have happened without his assistance.

I would also like to thank my many friends and family who have made grad school much more tolerable. Single sentences cannot really express how significant all of you have been, but in the interest of saving space that's all I can write here.

Jen, for all the fun and for always being there even from across the country.

Daniel, for all of the great in-depth conversations, inner-tube water polo, and eleventh hour assistance.

Natasha, for all of the good-natured humor and general life advice.

Jake, for being the social center and providing a counterweight when I lean too far to the side.

Tayler, for a refreshing perspective and all of the fun track workouts.

Ross, for great physics conversations and even better puns.

Jennifer, for being my favorite former student ;P

Devon, for all the nerding-out, as well as the coding assistance.

Mel, for always being a positive presence.

Kelsey and Alexey, for keeping me sane during the early years of grad school.

To my Riverside Bros: Aaron, Caleb, Keith, Nathan, and Hondo, for all the nonsensical fun over the years.

And of course to my parents, whose unending support has provided the bedrock necessary to pursue this degree.

May the Force be with you all!

Chapter 1

Introduction and Background

1.1 Introduction

The history of Particle Physics is one of ever-increasing quantities of materials, energy, scientists, engineers, and money being directed towards the discovery and investigation of the deepest and most fundamental laws and constituents of Nature. Rutherford arguably began this endeavour when he fired alpha particles at gold foil and consequently discovered the atomic nucleus, showing that atoms are not indivisible but are indeed composed of smaller particles. The 1920s saw the development of Quantum Mechanics, with Heisenberg showing certain pairs of observables cannot be simultaneously measured to arbitrarily high precision [96] and Schrodinger providing the wave equation which now bears his name [139]. Experiments in the 1930s found the positron [12] predicted by Dirac [65] in the first foray into relativistic quantum mechanics, as well as the neutron, which determines an element's specific isotope. This

decade also marked the discovery of the nuclear chain reaction, the first example of Einstein's famous equation $E = mc^2$ large enough to worry about, a discovery which would have tremendous impact in the following decade. In the late 1940s, Quantum Electrodynamics was developed as the first Quantum Field Theory by Richard Feynman [72], Julian Schwinger [142], and Sin-Itiro Tomonaga [151]. The European Organization for Nuclear Research, or CERN, was founded in the 1950s for the purposes of investigating the deep internal structure of matter via colliding particle beams, leading to the discovery of the $W^{\pm}$ and Z vector bosons of the electroweak interaction. By the time I was born, the Standard Model had been well-established and there remained only three missing pieces: the top quark, the tau neutrino, and the Higgs boson. The discovery of the top quark by the D0 collaboration at Fermilab in 1995 [1], the tau neutrino by the DONUT Collaboration at Fermilab in 2000 [105], and the subsequent discovery of the Higgs boson by the ATLAS and CMS collaborations at CERN in 2012 [44] [55], completed the Standard Model.

But the party is far from over, because although the Standard Model has passed every direct experimental test it is known from astronomical observations that as much as 95% of the content of the universe is not included in the Standard Model. Starting in the 1930s with observations of galaxy cluster motions [11], then later observations of galactic rotation curves [136], we have become increasingly aware of the fact that galaxies seem to harbor far more mass than can be accounted for with visible matter. The extra mass must be from some sort of matter which does not interact electromagnetically, which astronomers dubbed "dark matter." A bigger surprise came in 1998 when observations

of distant supernovae showed the expansion of the universe to be accelerating [135] [132] in direct opposition to the pull of gravity; although the field equations of General Relativity allow for a cosmological constant term which can cause an accelerating expansion [67], most scientists had assumed this term to be zero prior to the discovery of the accelerating expansion. The equations of General Relativity are non-renormalizable and cannot be quantized in the same manner as the other fundamental interactions, which raises one of the greatest ironies of Physics: gravity, the fundamental interaction with which we are most intimately familiar and the study of which lay at the core of the Scientific Revolution, is completely absent from the Standard Model.

Despite the prosaic name, the Standard Model contains many parameters some consider to be "unnatural". Chief among these is the mass of the Higgs boson, which quantum corrections should drive to the Planck scale roughly 16 orders of magnitude larger than the highest it could actually be (unitarity bound: [64], Planck scale: [118]). It has long been recognized that this "Higgs Hierarchy Problem" could be solved with an appropriate balancing between fermions and bosons, a sort of "supersymmetry" between the two classes of fundamental particles which can exist in a universe with 3 spatial dimensions. As an added bonus, the framework of Supersymmetry provides a natural dark matter candidate. The ATLAS experiment at the Large Hadron Collider at CERN has been designed to probe for new physics, including possibly Supersymmetry, which may reveal itself at the high energy proton-proton and heavy nuclei collisions which occur there. This dissertation will characterize a background to the disappearing track signature well motivated by many SUSY models, beginning with brief theoretical background,

then describing the ATLAS Detector and the reconstruction techniques for the various physics objects, then finally the analysis itself.

1.2 The Standard Model

The Standard Model of Particle Physics describes the known fundamental matter particles (fermions) and their non-gravitational interactions as a Lagrangian over the local gauge group $SU(3)_c \times SU(2)_L \times U(1)_Y$. One of the pillars upon which the Standard Model of Particle Physics is built is Noether's Theorem, which associates to every differentiable symmetry of the action a conserved quantity, in a generalization of the conservation laws found in Lagrangian and Hamiltonian classical mechanics [128]. The most salient manifestations of Noether's Theorem are the conservation of energy, momentum, and angular momentum, caused by invariance with respect to translations in time, translations in space, and rotation, respectively. The examples of space, time, and rotation are all external degrees of freedom corresponding to the Poincaré group, which is the set of isometries of Minkowski spacetime, but internal degrees of freedom can exist as well, and this is where the concept of *gauge symmetry* or *gauge invariance* comes in. Gauge invariance was first encountered with the electromagnetic field in the 19^{th} century, when the vector and scalar potentials $\vec{A}$ and ϕ were noted to contain terms which did not affect the dynamics of a system but could influence how difficult the calculations were; at the time, the force fields $\vec{E}$ and $\vec{B}$ were considered to be fundamental, with the $\vec{A}$ and ϕ just handy calculational tools. In the mid-20^{th} century,

the *Aharonov-Bohm Effect* [3] confirmed the existence of the vector potential as a real entity independent of its use as a calculational tool. The principle of gauge invariance means the form of an interaction is entirely determined by the symmetry group and requires the theory to be invariant under transformations of a generic member of said symmetry group.

The fundamental matter particles in our universe are Dirac fermions, meaning they have half-integer spin and consequently are subject to the Exclusion Principle, which forbids two fermions from occupying the same state. Imposing gauge invariance on the Lagrangian for Dirac fermions automatically produces the gauge bosons which mediate interactions between particles. The structure of the gauge interactions is determined by the Lie algebra of the relevant group, $SU(3)$ for the strong interaction, $SU(2) \times U(1)$ for the electroweak interaction. The associated boson fields are as follows:

$$SU(3)_c \rightarrow G_\mu^a,\ a \in 1, 2, ..., 8 \tag{1.1}$$

are the gluon fields, and

$$SU(2)_L \rightarrow W_\mu^a,\ a \in 1, 2, 3 \tag{1.2}$$

and

$$U(1)_Y \rightarrow B_\mu \tag{1.3}$$

are the electroweak gauge bosons. The strong and electroweak interactions of the Standard Model are mediated by the spin-1 vector bosons described above. Both the photon (γ) and the gluon (g) are massless, although the color confinement of the strong interaction means only electromagnetism has macroscopic range.

Consider the effect of a generic local gauge transformation[1] on an $SU(2)_L \times U(1)_Y$ doublet

$$\boldsymbol{L} \rightarrow \boldsymbol{L'} = \exp\left\{ \left(ig'\chi(x)\frac{Y_L}{2} + ig\boldsymbol{\alpha}(\boldsymbol{x}) \cdot \frac{\boldsymbol{\tau}}{2} \right) \mathbf{L} \right\} \tag{1.4}$$

and a similarly generic local transformation on $U(1)_Y$

$$\phi_R^l \rightarrow (\phi_R^l)' = \exp\left\{ \left(ig'\chi(x)\frac{Y_R^l}{2} \right) \phi_R^l \right\} \tag{1.5}$$

In these equations, χ and $\boldsymbol{\alpha}$ are phase rotations dependent upon the local spacetime point x, $\boldsymbol{\tau}$ are the generators of $SU(2)$, and g, g', Y_L, andY_R^l are the strengths of the interactions. These transformations, combined with the requirement that the Physics arising from this Lagrangian be independent of gauge, necessitate the following covariant derivatives for the electroweak interaction:

$$\mathcal{D}_\mu = \partial_\mu - \frac{1}{2}ig'B_\mu Y_L - \frac{1}{2}ig\boldsymbol{W_\mu} \cdot \boldsymbol{\tau} \tag{1.6}$$

and

$$\mathcal{D}_\mu = \partial_\mu - \frac{1}{2}ig'B_\mu Y_R^l \tag{1.7}$$

The new gauge fields B_μ and $\boldsymbol{W}_\mu$ correspond to the $U(1)_Y$ and $SU(2)_L$ components, respectively, and are chosen so as to keep the electroweak Lagrangian invariant under generic transformations of the overall $SU(2)_L \times U(1)_Y$ group. These gauge fields have the following transformation properties:

$$\boldsymbol{W}_\mu(x) \rightarrow \boldsymbol{W'_\mu}(x) = \boldsymbol{W}_\mu + \partial_\mu\boldsymbol{\alpha}(\boldsymbol{x}) + g\boldsymbol{W}_\mu(x) \times \boldsymbol{\alpha}(\boldsymbol{x}) \tag{1.8}$$

[1] A local gauge transformation is one which can vary the fields at all points in spacetime independently, therefore *local* gauge invariance is a much more strict requirement than *global* gauge invariance

and

$$B_\mu \to B'_\mu = B_\mu + \frac{1}{g'}\partial_\mu \chi(x) \tag{1.9}$$

with $\boldsymbol{\alpha(x)}$ and $\chi(x)$ representing the same local phase rotations as before. This leads to the gauge boson Lagrangian term:

$$\mathcal{L}_{\text{gaugeboson}} = -\frac{1}{4}\boldsymbol{F}_{\mu\nu}\boldsymbol{F}^{\mu\nu} - \frac{1}{4}B_{\mu\nu}B^{\mu\nu} + \frac{1}{2}M^2\boldsymbol{W}_\mu\boldsymbol{W}^\mu \tag{1.10}$$

where $\boldsymbol{F}^{\mu\nu}$ and $B^{\mu\nu}$ are the field tensors, defined as:

$$\boldsymbol{F}^{\mu\nu} = \partial^\mu \boldsymbol{W}^\nu - \partial^\nu \boldsymbol{W}^\mu + g\boldsymbol{W}^\mu \times \boldsymbol{W}^\nu \tag{1.11}$$

and

$$B^{\mu\nu} = \partial^\mu B^\nu - \partial^\nu B^\mu \tag{1.12}$$

And therein lies the problem: the first two terms in the gauge boson Lagrangian are clearly gauge invariant, but the third one is not *unless* $M = 0$. This is where the Higgs mechanism comes in. The Higgs mechanism breaks electroweak symmetry via the introduction of a complex scalar doublet, mixing the vector boson fields B^μ and W^μ to produce the massless photon A^μ and the massive Z^μ and $W^\pm$, which carry the electromagnetic and weak interactions, respectively [97] [70]. The Higgs mechanism introduces a chiral doublet as described in the following equation:

$$\phi = \begin{pmatrix} \phi^+ \\ \\ \phi^0 \end{pmatrix} = \frac{1}{\sqrt{2}} \begin{pmatrix} \phi^1 + i\phi^2 \\ \\ \phi^3 + i\phi^4 \end{pmatrix} \Rightarrow \begin{pmatrix} H_u^+ & H_u^0 \\ \\ H_d^- & H_d^0 \end{pmatrix} \tag{1.13}$$

The u and d subscripts mean *up* and *down*, respectively, and correspond to the relative direction of the weak isospin. The Higgs mechanism mixes the fundamental W^μ and B^μ

to produce the physical $W^{\pm}$, A^{μ}, and Z^{μ} states, with the charged components defined by $W^{\pm} = \frac{1}{\sqrt{2}}(W^1 \mp iW^2)$, and the neutral components defined as:

$$A^{\mu} = \cos(\theta_W)B^{\mu} + \sin(\theta_W)W^3$$

$$Z^{\mu} = -\sin(\theta_W)B^{\mu} + \cos(\theta_W)W^3$$

The term θ_W is the "weak mixing angle", also known as the "Weinberg angle" in reference to Steven Weinberg, who together with Sheldon Glashow and Abdus Salam developed Electroweak Theory back in the 1960s [86][138][153]. Electroweak symmetry is spontaneously broken by assigning the ground state of the Higgs field:

$$\Phi_0 = \frac{1}{\sqrt{2}} \begin{pmatrix} 0 \\ \\ v \end{pmatrix}. \tag{1.14}$$

The process of this mixing causes both of the charged and one of the neutral fields of the Higgs doublet to be absorbed by the W and Z bosons, providing them with mass and a longitudinal polarization degree of freedom. The fourth field becomes the spin-0 Higgs boson H, recently discovered with a mass of 125 GeV [44] [55].

The electrically neutral part of the Standard Model Higgs potential for a complex field H is:

$$V = m_H^2|H|^2 + \lambda|H|^4, \tag{1.15}$$

which is required to have a non-vanishing vacuum expectation value (vev) at the minimum of the potential. The minimum of the potential is at

$$\frac{\partial V}{\partial H} = 2m_H^2|H| + 4\lambda|H|^3 = 0 \rightarrow \langle H \rangle = \sqrt{\frac{-m_H^2}{2\lambda}} \tag{1.16}$$

But this isn't the end of the story: the Higgs field interacts with all of the other fields and these interactions provide "corrections" to the Higgs mass. For example, a Dirac fermion (say, an electron) with mass m_f and coupling to the Higgs of $-\lambda_f H\bar{f}f$ contributes a correction term:

$$\Delta m_H^2 = -\frac{|\lambda_f|^2}{8\pi^2}\Lambda_{UV}^2 + ... \tag{1.17}$$

where Λ_{UV} is the ultraviolet cut-off scale at which new physics must enter the theory [118]. This is where things get more interesting, because it was known by the mid-1970s that certain processes, such as $WW \to WW$ scattering, would violate unitarity if the mass of the Higgs boson were much greater than about 1 TeV [64]. This feature, known as the unitarity bound, provided ironclad mathematical reasons to expect the discovery of either a light Higgs or some sort of new physics at about the TeV-scale. If we assume Λ_{UV} is near the Planck scale, then the correction term has a multiplier *over a dozen orders of magnitude* larger than the highest mass which preserves unitarity, requiring an extremely precise cancellation to get the Higgs boson mass into the allowed range. The Standard Model is summarized in Figure 1.1.

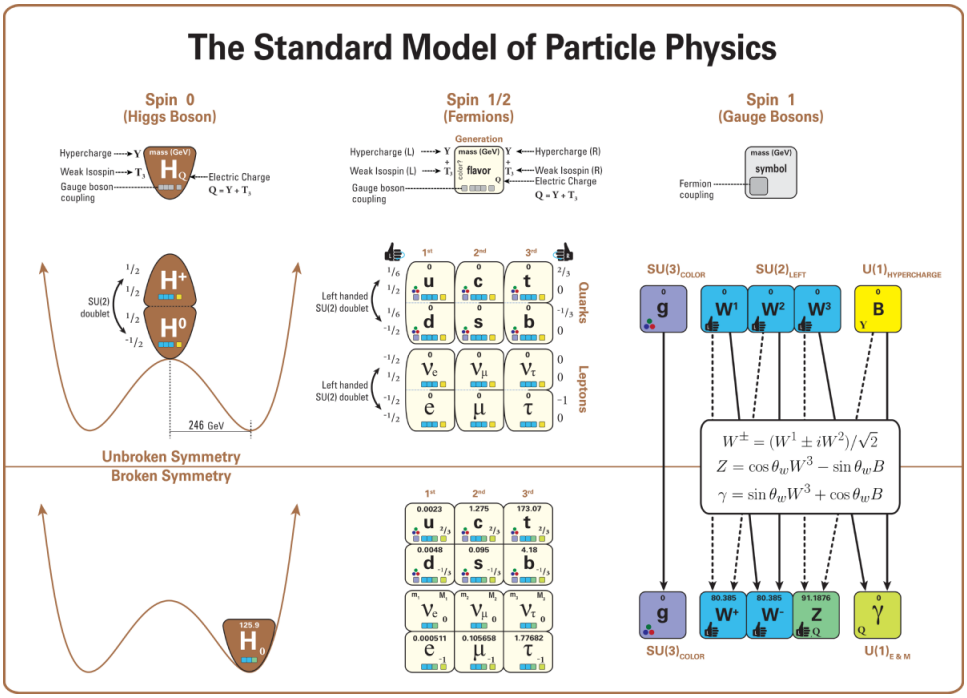

Figure 1.1: Summary of the Standard Model. Image Credit: Latham Boyle, `https://commons.wikimedia.org/w/index.php?curid=45839544`

1.3 Supersymmetry

Fortunately, bosons and fermions contribute oppositely to the mass of the Higgs boson, so the existence of fermion partners for each boson and boson partners for each fermion would generally result in a light Higgs boson, provided the partner-particles are similar in mass; we call this boson-fermion matching "Supersymmetry". Supersymmetry (SUSY) is a proposed spacetime symmetry which extends the Standard Model symmetry group to $SO(10)_{\text{SUSY}}$, with an associated transformation operator Q which carries half-integer spin and therefore converts between bosons and fermions:

$$Q\,|\text{Fermion}\rangle = |\text{Boson}\rangle\,, \quad Q\,|\text{Boson}\rangle = |\text{Fermion}\rangle\,. \tag{1.18}$$

It was proven by Haag, Lopuszański, and Sohnius that the Supersymmetry algebra is the most generic possible extension of the Standard Model "Poincaré times $SU(3)_c \times SU(2)_L \times U(1)_Y$" group which still satisfies certain deep requirements of QFT [90]. Supersymmetry does not just allow for a Higgs with mass below the unitarity bound, it *prefers* the Higgs mass to be substantially below the unitarity bound, so the 2012 discovery of a Higgs boson with a mass of only 125 GeV is tantalizing though far from definitive.

Standard Model particles and their Supersymmetric partners fall into irreducible representations of the overall SUSY Lie Algebra called *supermultiplets*. The Supersymmetry generators Q and $Q^\dagger$ commute with the generators of the Standard Model gauge transformations, therefore members of the same supermultiplet must have

the same electric charge, weak isospin, and color degrees of freedom. It can also be shown theoretically [118] that two states $|\Omega\rangle$ and $|\Omega'\rangle$ inhabiting the same supermultiplet must have the same mass, which is a problem because there are no known pairs of particles with precisely the same mass and quantum numbers but differing by one half-integer of spin. This apparent absence of Supersymmetric particles means that if Supersymmetry exists in our universe it must be a broken symmetry.

Since its inception in the 1970s the space of Supersymmetry models has undergone its own period of exponential inflation, the vast majority of which lay beyond the scope of this dissertation, though the interested reader can find abundant reference material; some broad classes of Supersymmetry models are Planck-Mediated Supersymmetry Breaking (PMSB) [107], Gauge-Mediated Supersymmetry Breaking (GMSB) [85], and Anomaly-Mediated Supersymmetry Breaking (AMSB) [103].

The lightest supersymmetric particle (LSP) must be stable because of R-parity [71]:

$$R = (-1)^{3(B-L)+2s} \tag{1.19}$$

where B is baryon number, L is lepton number, and s is spin. All Standard Model particles have $R = +1$ and all SUSY particles have $R = -1$, therefore Supersymmetric particles must be produced in pairs and the decay of a Supersymmetric particle must include another Supersymmetric particle. This means if Supersymmetry is real then the cosmos must still have all of the LSPs created in the Big Bang or through the decay

of heavier Supersymmetric particles.

Astronomical observations going back nearly a century indicate the presence of an enormous amount of "dark matter", which does not emit or absorb any electromagnetic radiation, in our universe, outweighing ordinary matter by roughly six to one [11] [136]. In the early 1980s it was realized that the LSP can serve as the dark matter particle [24]. In order to function as dark matter, this LSP must be electrically-neutral, which rules out the sleptons and the squarks, as well as color-neutral [149], ruling out the gluino as well.

Supersymmetric particles have been ruled out experimentally up to the electroweak scale of $\mathcal{O}(100\,\mathrm{GeV})$, which naturally raises the question of "why are there no supersymmetric particles lighter than the electroweak gauge bosons?". It is possible only one supermultiplet is accessible, while all the rest live at mass-scales beyond the reach of any near-term human technology. This is described in the paper [130]. An appealing feature of a neutralino LSP is that it is a natural dark matter candidate, being massive (non-relativistic), electrically-neutral, and color-neutral.

The electroweakinos are the supersymmetric partners of the electroweak gauge and Higgs boson fields. Supersymmetry exists above the scale of electroweak symmetry breaking, meaning the electroweakinos are partners of the fundamental W^μ, B^μ, and H fields, which then mix during electroweak symmetry breaking to form the four

neutralinos and two charginos. The neutralino mass matrix at tree level is:

$$\mathbb{M}_{\chi} = \begin{pmatrix} M_1 & 0 & -\frac{g' v_d}{\sqrt{2}} & \frac{g' v_u}{\sqrt{2}} \\ 0 & M_2 & \frac{g v_d}{\sqrt{2}} & -\frac{g v_u}{\sqrt{2}} \\ -\frac{g' v_d}{\sqrt{2}} & \frac{g v_d}{\sqrt{2}} & 0 & -\mu \\ \frac{g' v_u}{\sqrt{2}} & -\frac{g v_u}{\sqrt{2}} & -\mu & 0 \end{pmatrix}. \tag{1.20}$$

The parameters g and g' are the coupling constants of the $SU(2)$ and $U(1)$ gauge groups, respectively, while v_u and v_d are the vacuum expectation values of the neutral components of the Higgs doublet, M_1 and M_2 are the soft-SUSY breaking bare masses of the bino and wino, respectively, and μ is the vector-like mass parameter of the Higgs doublet superfield [106].

If the wino mass term is much smaller than the bino and higgsino mass terms, $|M_2| << M_1, \mu$, then the lightest neutralino (the LSP) and chargino (the NLSP) become almost pure-wino. This causes the lightest neutralino and chargino to be mass degenerate at tree-level, with radiative corrections from loop diagrams of the Standard Model electroweak gauge bosons giving a slightly greater mass to the chargino. These loop corrections have been calculated to two-loop order, and for a wide range of neutralino masses provide a mass gap of $\approx 165\,\text{MeV}$ [101], as seen in Figure 1.2. The decay width is given by the equation:

$$\Gamma(\tilde{\chi}_1^{\pm} \to \tilde{\chi}_1^0 \pi^{\pm}) = \frac{2G_F^2}{\pi} \cos\theta_c{}^2 f_\pi^2 \Delta m_{\tilde{\chi}_1}^3 \left(1 - \frac{m_\pi^2}{\Delta m_{\tilde{\chi}_1}^2}\right)^{\frac{1}{2}}, \tag{1.21}$$

where G_F, θ_c, f_π, and m_π are the Fermi coupling constant, the Cabbibo angle, the

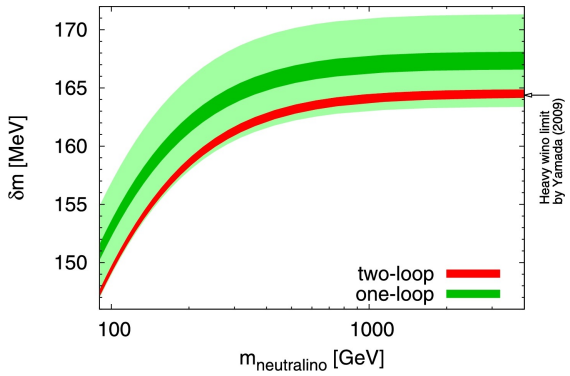

Figure 1.2: Chargino - Neutralino Mass Gap for pure-wino LSP [101]

pion decay constant ($\approx 130\,\mathrm{MeV}$), and the pion mass, respectively. Plugging in $\Delta m = 165\,\mathrm{MeV}$ and converting to a lifetime via $\Gamma\tau = \hbar$ we get $\tau_{\tilde{\chi}_1^\pm} \approx 0.2\,\mathrm{ns}$, or a decay length of $c\tau = \mathcal{O}(\mathrm{cm})$.

If instead the higgsino mass term is the smallest, $|\mu| << M_1, M_2$, then the lightest neutralino and chargino are nearly pure higgsino. At tree level the mass splitting between chargino and neutralino is approximately $\frac{m_Z^2}{2M_{1,2}}$ [118], which by assumption is negligibly small. As with the (nearly) pure wino LSP, radiative corrections from the Standard Model electroweak gauge bosons contribute an additional mass difference

$$\Delta m_+|_{rad} = \frac{\alpha_2}{4\pi} m_{\chi^\pm} \sin(\theta_W)^2 f(\frac{m_Z}{m_{\chi^\pm}}), \tag{1.22}$$

with $\alpha_2 \equiv \frac{g^2}{4\pi}$ where g is the $SU(2)$ coupling constant, θ_W is the weak mixing angle, m_Z is the Z boson mass, and the function $f(x)$ is defined by:

$$f(x) = 2\int_0^1 dt(1+t)\ln(1+\frac{x^2(1-t)}{t^2}). \tag{1.23}$$

For higgsino masses between 200 GeV and 1500 GeV this results in a mass gap of 280 − 350 MeV [124]. The corresponding decay length goes as [150]

$$c\tau = 1.1\,\mathrm{cm}\left(\frac{\Delta m_+}{300\,\mathrm{MeV}}\right)^{-3}\left[1-\frac{m_{\pi^\pm}^2}{\Delta m_+^2}\right]^{-\frac{1}{2}}. \tag{1.24}$$

This is not quite as long as the nearly pure wino case, but is still long enough to allow the possibility of charginos reaching the Pixel Detector. This provides a distinct signature in the ATLAS Detector: a track begins to form but disappears prior to reaching the Semi-Conductor Tracker. This is called the "disappearing track signature", and it's quite possible that this is the only Supersymmetry signature visible at the LHC. It is the background to this signature we are characterizing in this analysis.

The diagrams for chargino production in Anomaly-Mediated Supersymmetry Breaking are in Figure 1.3, and more details about AMSB can be found in Appendix A.

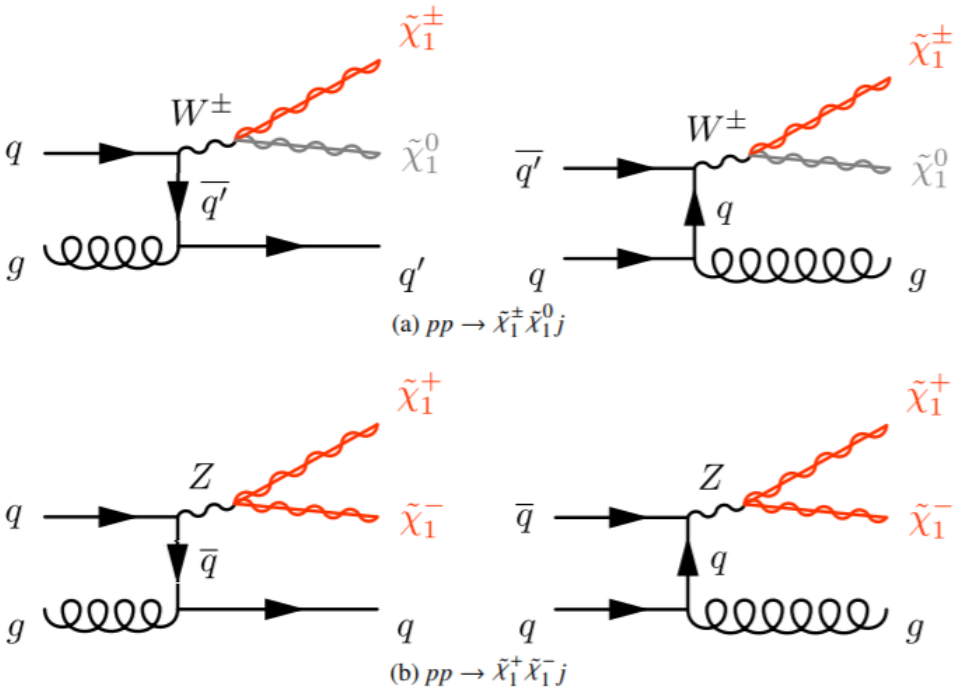

Figure 1.3: Chargino Production Diagrams

Chapter 2

The LHC and the ATLAS Detector

2.1 The Large Hadron Collider

The Large Hadron Collider (LHC) is located in a ring with a 27 kilometer circumference along the French-Swiss border near Geneva, built to accelerate and collide protons and heavy ions at ultra-relativistic energies. The machine is buried about 100 m underground to shield the detectors from cosmic rays and minimize the impact on the landscape, in the same tunnel as the preceding LEP I and II electron-positron colliders. The decision to re-use the LEP ring was made primarily to save on construction costs, as drilling through solid earth is expensive, but this did have drawbacks. All charged particles emit synchrotron radiation when their trajectories are curved, but the power emitted scales as $P \propto m^{-4}$, making lighter particles much more difficult to maintain at high energy around curves as compared to more massive particles. LEP was therefore constructed as an octagon, with RF cavities along the straight sections to propel the

electrons and tight corners to minimize synchrotron losses. The LHC is limited by the bending power of the magnets. Had the tunnel been built originally for protons, the corners would have been more gradual, reducing the magnet strength necessary to control the beams and therefore allowing for a somewhat increased available beam energy. Counter-rotating beams of protons or heavy ions, typically lead nuclei, collide in four intersection points around the ring at the sites of the four main detectors: ATLAS, CMS, ALICE, and LHCb. ATLAS and CMS are the two larger, general-purpose detectors, while the others are specialized to analyze specific processes, with ALICE focusing on heavy-ion collisions and LHCb optimized for B meson decays.

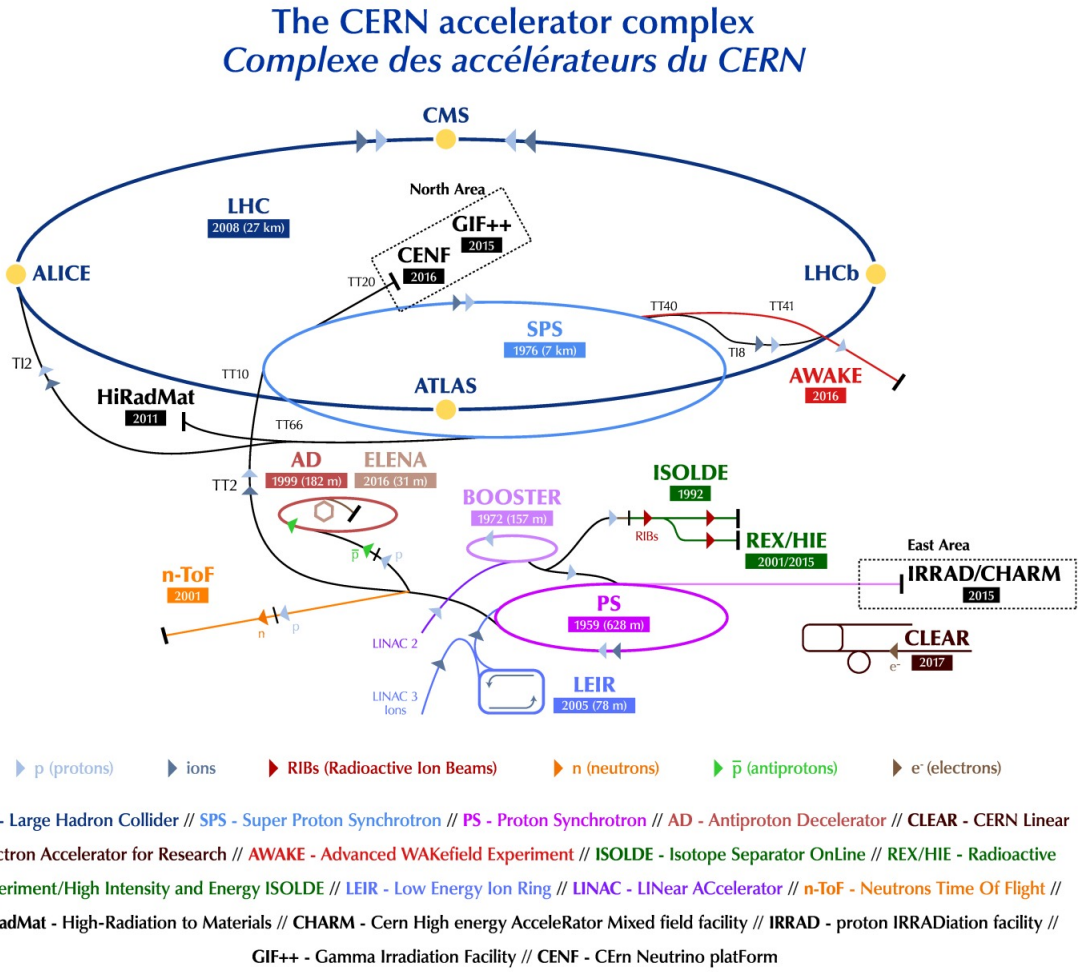

Figure 2.1: The CERN Accelerator Complex [91]

2.2 The ATLAS Detector

The ATLAS Detector is one of two general-purpose detectors at the Large Hadron Collider [15], the other being CMS. From the interaction point outward[1], the sub-detectors of ATLAS are: the Inner Detector, the Electromagnetic Calorimeter, the Hadronic Calorimeter, and the Muon Spectrometer. ATLAS has forward-backward and axial symmetry about the collision point, with several varieties of barrel and end-cap detectors. The Inner Detector consists of four pixel layers, from 3 cm out to 12 cm in radius and pseudorapidity $|\eta| < 2.5$, the silicon-strip detector (SCT) from 30 cm to 52 cm covering up to $|\eta| < 2.5$ in pseudorapidity, and the Transition Radiation Tracker (TRT) from 56 to 108 cm. A thin superconducting solenoid provides a constant axial magnetic field of strength 2 T to bend the paths of all charged particles traversing the detector.

[1] ATLAS uses a right-handed coordinate system, with the x-axis pointed towards the center of the LHC ring, the y-axis pointed towards the sky and the z-axis pointed along the beam. The spherical θ and ϕ coordinates are defined in the conventional way, with the azimuthal angle ϕ being measured in the xy-plane as the angle from the x-axis and the polar angle θ measuring the angle from the positive z-axis. However, the polar angle is often ignored in favor of the pseudorapidity η, defined as $\eta = -\ln(\tan(\frac{\theta}{2}))$. The observables E_T, p_T, and E_T^{miss} are all defined in the xy-plane, and the distance measure ΔR in the $\eta\phi$-space is defined as $\Delta R = \sqrt{(\Delta\eta)^2 + (\Delta\phi)^2}$.

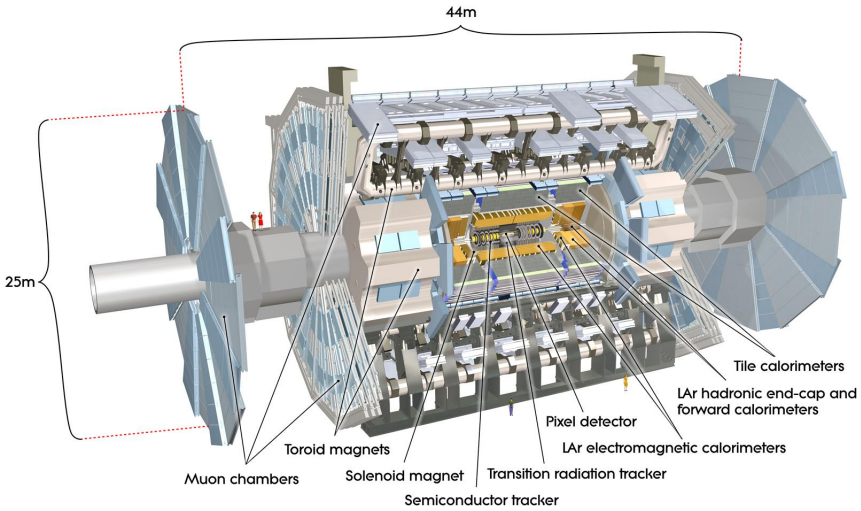

Figure 2.2: The ATLAS Detector [53]

2.2.1 Inner Detector

The Inner Detector is immersed in a magnetic field of strength 2 T along the beam axis, produced by a solenoid running between the TRT and the Electromagnetic Calorimeter. The Pixel Detector and SCT both have a range of $|\eta| < 2.5$ and the TRT covers $|\eta| < 2.0$.

The inner-most portion of the Inner Detector are the four Pixel Detector layers which together have more than 92 million readout channels [47]. The innermost layer, called the "Insertable B-Layer" or IBL, has typical pixel dimensions of $50\,\mu\text{m} \times 250\,\mu\text{m}$ in the transverse and longitudinal directions, respectively, with a sensor thickness of about $200\,\mu\text{m}$ [49]. The pixels in the other layers are a bit larger, $50\,\mu\text{m} \times 400\,\mu\text{m} \times 250\,\mu\text{m}$

for transverse, longitudinal, and thickness. The Pixel detector has a hit efficiency of about 99% and intrinsic accuracies of the Pixel layers are $10\,\mu$m in $R-\phi$ and $115\,\mu$m in z. The Pixel Detectors measure the amount of charge in each pixel by timing how long the signal pulse from a passing charged particle remains above a threshold, because the time over threshold increases monotonically with the deposited energy; this is known as the "Time-over-Threshold" (ToT) method.

The SCT also uses silicon detectors, but organized as strips instead of pixels, and it has a similarly high hit efficiency of $\approx 99\%$, along with resolutions of $17\,\mu$m in $R-\phi$ and $580\,\mu$m in z [50]. The silicon strips are double-layered, with one layer running parallel to the beam and the other layer rotated by 40 mrad; this allows for the $3D$ position of the hit to be reconstructed, with the SCT typically measuring 4 space-points per track. The barrel of the SCT has four layers, while the endcaps have nine annular disks around the beamline [50].

The TRT, consists of roughly $300,000$ straws of 2 mm radius filled with a mix of Xe-CO2-O2 gas and a wire running through the center of each tube [52]. The wire is held at a potential of $\approx 1.4\,$kV, which causes ions produced by passing charged particles to accelerate towards it producing a signal amplified by a factor of $\mathcal{O}(10^4)$. The front-end electronics amplify and digitize the ionization signal using two thresholds, a low-threshold for tracking hits and a high one for transition radiation. The width of the signal above threshold is directly related to how far the track is from the wire

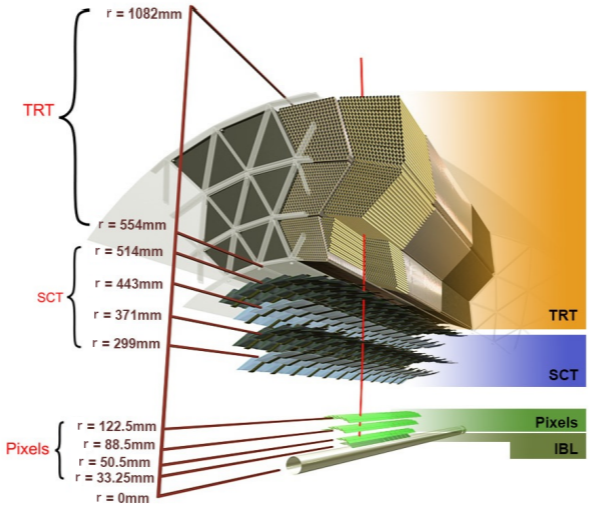

Figure 2.3: Inner Detector [53]

because of the time it takes the ions to reach the wire, with precision timing allowing a position resolution of $\approx 130\,\mu$m. The straw tubes are embedded in mats of fine polypropelene/polyethylene fibers to produce transition radiation. A relativistic charged particle passing between media with different dielectric constants can produce transition radiation in the soft x-ray range of a few keV, which subsequently ionizes the gas in the straws triggering comparatively large avalanches which exceed the high-threshold. The probability for a charged particle to produce photons of sufficient energy is proportional to $\gamma = \frac{E}{m}$, so an electron will be more than 200 times more likely to produce the necessary transition radiation than a $\pi^{\pm}$ at the same energy, thus discriminating between electrons and pions independently of the calorimeters. A charged particle passing through the Inner Detector will typically produce 4 hits on the Pixel Detector, 8 in the SCT, and 36 in the TRT. A cross-section of the Inner Detector in Run 2 can be found in Figure 2.3.

2.2.2 Electromagnetic Calorimeter

Outside the Inner Detector is the Electromagnetic Calorimeter, which detects energy deposits primarily from electrons, positrons, and photons. The ECal has a barrel component covering the range $|\eta| < 1.475$ and an endcap component extending to $1.375 < |\eta| < 3.2$, along with a presampler covering $|\eta| < 1.8$ to correct for photon and electron energy losses in the upstream portion of the detector. Within the barrel the ECal is split into three layers: layer 1 is finely-segmented in η with strips of $\Delta\eta \times \Delta\phi = \frac{0.025}{8} \times 0.1$ to provide solid position resolution and distinguish photons originating from events of interest vs the double-peak from $\pi^0 \to \gamma\gamma$ decays; layer 2, where the majority of the energy is deposited, is composed of cells of size $\Delta\eta \times \Delta\phi = 0.025 \times 0.025$ and is 16 radiation lengths thick; layer 3 is more coarse-grained with cells of size $\Delta\eta \times \Delta\phi = 0.05 \times 0.025$ and measures the tail-end of electromagnetic showers. These layers are all constructed with alternating lead absorber plates and electrodes bathed in liquid argon (LAr) in an accordion-like arrangement to maximize coverage [16].

The energy resolution of the Electromagnetic Calorimeter is [16]:

$$\frac{\sigma(E)}{E} = \frac{10\%}{\sqrt{E}} \oplus \frac{0.3}{E} \oplus 0.4\% \tag{2.1}$$

Each of the terms in the above equation corresponds to a different source of uncertainty. The first is the "stochastic" term, which arises from the fact that the number of track segments within the shower, which is directly proportional to the calorimeter output, scales with the square-root of the energy of the incident particle; this is the dominant uncertainty at energies below . The second is the "noise" term, representing electronic

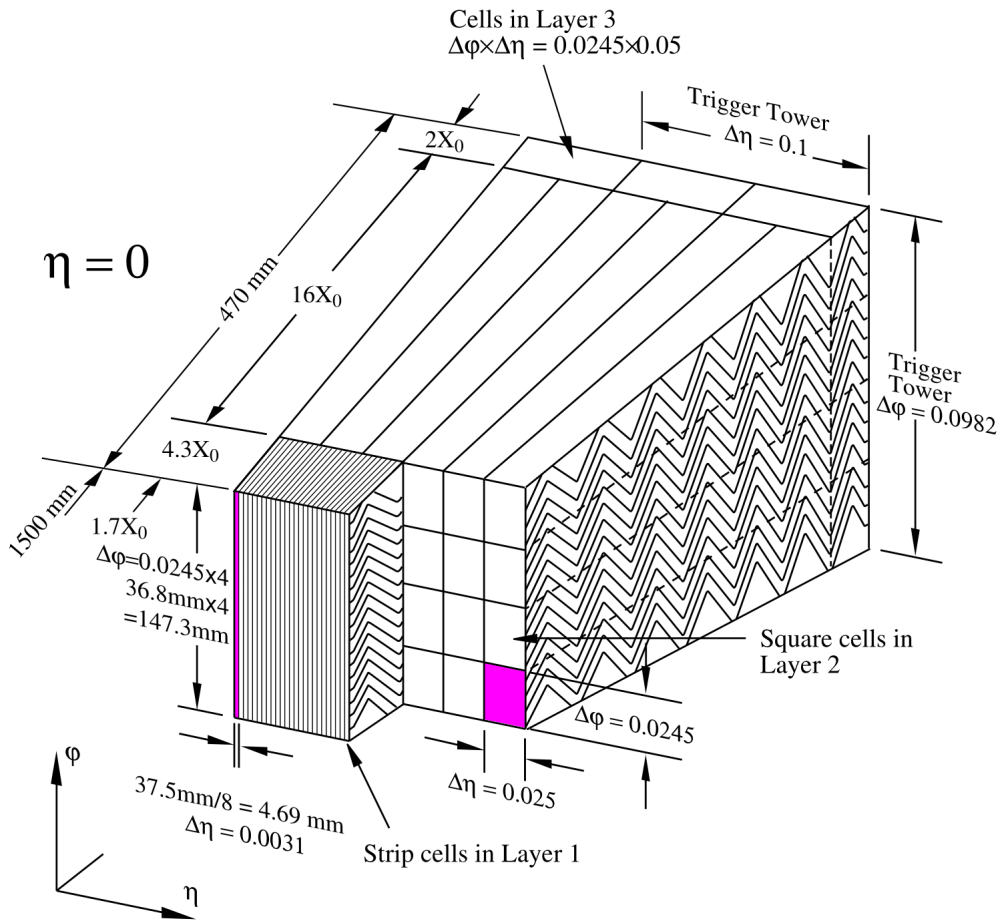

Figure 2.4: Electromagnetic Calorimeter Barrel [39]

noise in the readout chain. The last term is the "constant" term, which includes energy-independent uncertainties such as the nonuniform geometry of the detector; this term dominates at high energies. The symbol $\oplus$ means the terms are added in quadrature, $R = x \oplus y \rightarrow R^2 = x^2 + y^2$. For example, this means a 100 GeV particle will have a resolution of $\frac{\sigma(E)}{E} = 1\% \oplus 0.003 \oplus 0.4\% = 1.1\%$, whereas a 10 GeV particle will have a relative uncertainty of $\frac{\sigma(E)}{E} = 40\%$.

2.2.3 Hadronic Calorimeter

Beyond the ECal is the Hadronic Calorimeter or HCal, which is similarly broken up into a barrel covering $|\eta| < 1.7$ and endcap covering $1.7 < |\eta| < 3.2$. The HCal barrel ($|\eta| < 1.0$) and extended barrel ($0.8 < |\eta| < 1.7$), collectively the "TileCal", use steel absorber plates and scintillating tile active material arranged in three readout layers, with the inner two layers having a granularity of $\Delta\eta \times \Delta\phi = 0.1 \times 0.1$ and the outer one with a granularity of $\Delta\eta \times \Delta\phi = 0.2 \times 0.1$ [39]. Out to $|\eta| < 1.7$ the HCal uses plastic scintillating tiles along with steel absorber plates, with wavelength-shifting fibers delivering light from the scintillating tiles to the photomultiplier tubes (PMTs), which each collect the light from several nearby tiles. The analog signals from the PMTs are amplified and shaped before being sampled and digitized by a 10-bit analog-to-digital converter (ADC) every 25 ns. Assorted calibration systems allow the TileCal to maintain a precision for the electromagnetic scale of about 1% across its entire length.

The HCal endcap uses copper as the absorber and LAr as the active material, with the finest granularity matching that of the barrel section. In the endcap region, $1.5 < |\eta| < 3.2$, LAr is used along with copper absorbers, and the Forward Calorimeter also uses LAr with copper and tungsten absorbers to cover the range $3.1 < |\eta| < 4.9$. The analog signals from the LAr calorimeters are digitally sampled once per bunch crossing over four bunch crossings, and at the 25 ns bunch spacing has sensitivity to up to 24 preceding bunch-crossings, making it sensitive to out-of-time pile-up from

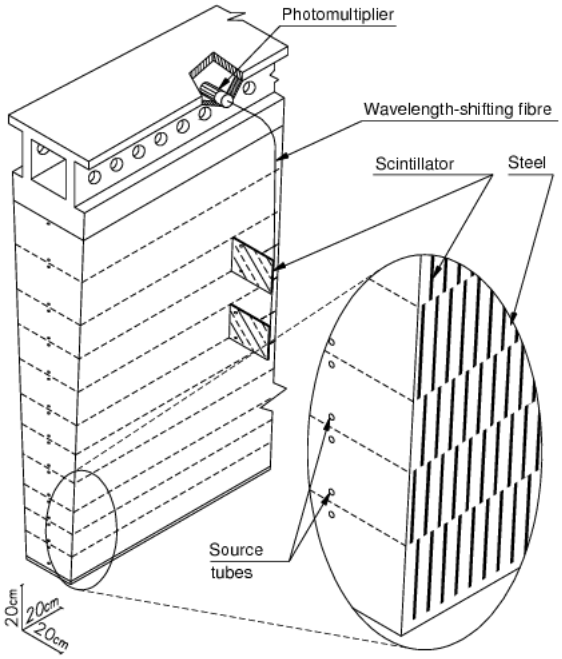

Figure 2.5: Hadronic Tile Calorimeter [39]

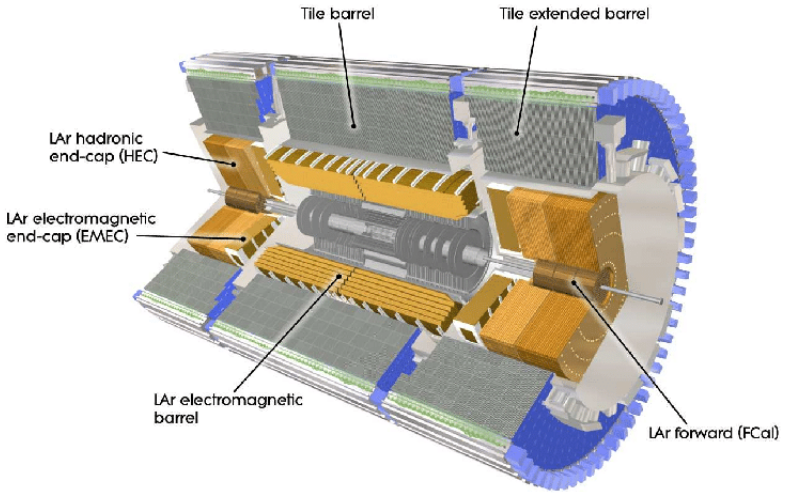

Figure 2.6: ATLAS Calorimeters [39]

many previous collisions. This sensitivity is mitigated by the fast Tile calorimeter. The responses of the calorimeters were measured using $\pi^{\pm}$ and electron test beams prior to the start of LHC operations and were found to be [48]:

$$\frac{\sigma_E}{E} = \frac{10\%}{\sqrt{\frac{E}{\text{GeV}}}}, \text{ Electromagnetic Calorimeter}$$
$$\frac{\sigma_E}{E} = \frac{56\%}{\sqrt{\frac{E}{\text{GeV}}}} \oplus 6\%, \text{ Hadronic Calorimeter Barrel}$$
$$\frac{\sigma_E}{E} = \frac{70\%}{\sqrt{\frac{E}{\text{GeV}}}} \oplus 6\%, \text{ Hadronic Calorimeter EndCap}$$

2.2.4 Muon Spectrometer

The Muon Spectrometer is the outermost subdetector of ATLAS, measuring muons out to a range of $|\eta| < 2.7$ via several different mechanisms. The physical material of the inner detectors and calorimeters provide more than 100 radiation lengths of attenuation between the interaction point and the Muon Spectometer with the Tile-

Cal alone providing more than seven interaction lengths of shielding from pions [48], eliminating all other Standard Model particles. The Muon Spectrometer is capable of independently measuring the momenta of muons down to $p_T \approx 3\,\text{GeV}$ [48]. As with the interior subdetectors, the Muon Spectrometer is split into a barrel and two endcap sections, with the former covering $|\eta| < 1.05$ and the latter $1.05 < |\eta| < 2.7$. Three superconducting air-core toroidal magnets provide the magnetic field, with a bending integral of $2.5\,\text{T}\cdot\text{m}$ in the barrel and up to $6\,\text{T}\cdot\text{m}$ in the endcaps.

Out to $|\eta| = 2.0$ the MS is instrumented with three layers of monitored drift tubes (MDTs), each of which provides six to eight η measurements along the muon's trajectory, with single-hit precision of $\approx 80\,\mu\text{m}$; for $|\eta| > 2.0$, the innermost MDT is replaced with a quadruplet layer of cathode strip chambers (CSCs), with single-hit precision of $\approx 60\,\mu\text{m}$; this replacement is made because the CSCs have superior timing resolution and are better able to withstand the higher event rates at high-η.

Within the barrel region, triggering and precision (η, ϕ) measurements are made by Resistive Plate Chambers (RPCs), arranged in three doublet layers. Resistive Plate Chambers consist of metallic strips on parallel electrode plates to detect ionization in a gas mixture, and have an intrinsic time resolution of 1.5 ns. For most of the endcap, from $1.0 < |\eta| < 2.4$, Thin-Gap Chambers (TGCs) arranged with one triplet layer and two doublet layer provide similar capability; typical spatial resolution for the RPCs and TGCs is $5 - 10\,\text{mm}$. Thin-Gap Chambers are multi-wire proportional chambers with

shorter wire-to-cathode than wire-to-wire distance, and intrinsic time resolution of 4 ns. The total time resolution, accounting for signal propagation and electronics-processing time, for both RPCs and TGCs is between $15-25$ ns, quick enough to tag the individual bunch-crossing responsible for a given muon.

The central toroidal magnetic field extends out to $|\eta| < 1.4$ with the end-cap magnetic field covering the region $1.6 < |\eta| < 2.7$; the transition region from $1.4 < |\eta| < 1.6$ is affected by both magnetic fields and is where the precision of the detector is the weakest. Muon Drift Tubes (MDTs) are used across most of the η range of the MS for precision measurement of the muons in the bending direction of the magnetic field in η. Cathode Strip Chambers (CSCs) are used in the range $2.0 < |\eta| < 2.7$ in the innermost layer, while Resistive Plate Chambers and Thin-Gap Chambers are used for triggering and to measure the ϕ-coordinate in the barrel and endcap, respectively.

The precision of the Muon Spectrometer was measured in 2010 using $Z \to \mu\mu$ collision data and found to be [123]:

$$\frac{\sigma_{p_T}}{p_T} = 0-6\% \left(\frac{4\text{GeV}}{p_T}\right) \oplus 4-9\% \oplus 23-30\% \left(\frac{p_T}{\text{TeV}}\right), \tag{2.2}$$

again with weaker performance in the transition region than in either the barrel or the endcaps. The Inner Detector provides superior resolution for low-p_T muons, with the Muon Spectrometer gaining the advantage above ≈ 30 GeV.

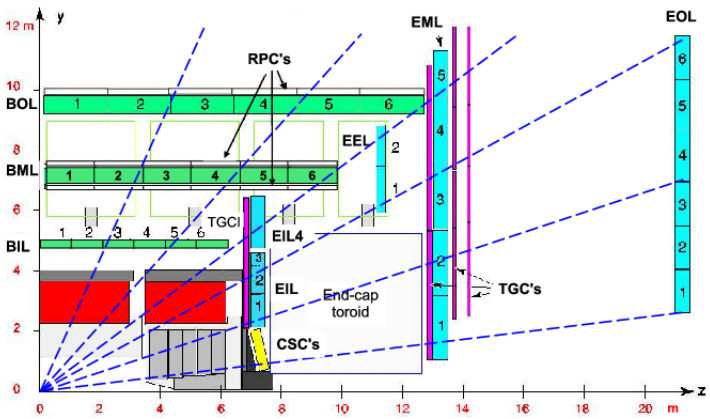

Figure 2.7: Muon Spectrometer (profile) [141]

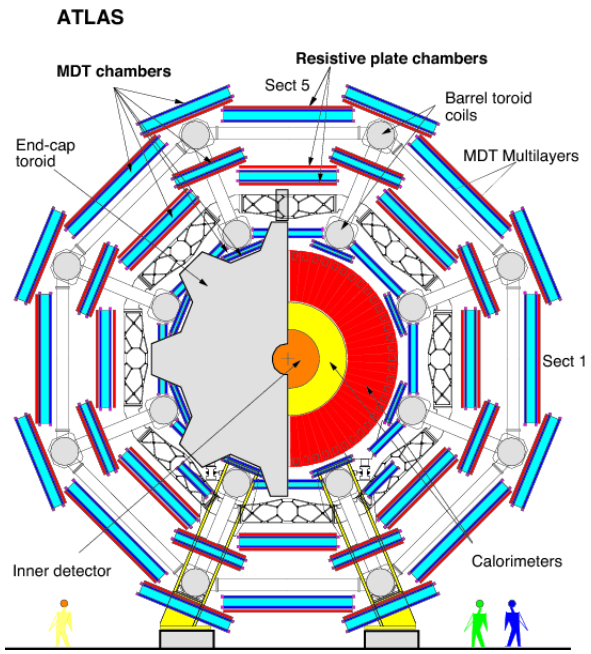

Figure 2.8: Muon Spectrometer (cross-section) [39]

2.2.5 Trigger System

The LHC beams have a bunch spacing of only 25 ns, corresponding to a bunch-crossing rate of 40 MHz; with an average of 25 proton-proton collisions per bunch-crossing ("pile-up") and each event requiring $\approx$ 1.6 MB, this would correspond to 1600 $\frac{\text{TB}}{\text{s}}$ if *everything* were recorded. To mitigate the deluge, ATLAS utilizes a two-level trigger system, a low-level hardware trigger and a high-level software-defined trigger, which together reduce the overall event rate to about 1 kHz. The hardware-based level-one (L1) trigger is coarse-grained and utilizes the Calorimeters and Muon Spectrometer, using up to 2.5 μs to decide whether or not to pass an event along to the second trigger level, filtering out enough events to reduce the data rate to about 100 kHz. The software-based high-level-trigger (HLT) utilizes the full granularity of the detector and has about 200 ms to decide whether or not an event should be recorded; this reduces the event rate from 100 kHz to 1 kHz.

Chapter 3

Data Collection and Simulated Events

This analysis made use of a Z tag-and-probe strategy using lepton triggers, while the main analysis requires a E_T^{miss} trigger. The closure test, done to check that the Transfer Factors are process-independent, required the use of Monte Carlo production of both $Z \to \ell\ell$ and $W \to \ell\nu$ processes. Finally, a few representative pure wino samples were produced with Monte Carlo to estimate the disappearing track sensitivity given the background due to lepton scatters.

The raw data were recorded in ATLAS in 2015 and 2016 at a center of mass energy of 13 TeV with a bunch spacing of 25 ns and a peak instantaneous luminosity of $2.2 \times 10^{34}\,\text{cm}^{-2}\text{s}^{-1}$. Data is taken in two minute "luminosity blocks" of collisions with a variety of quality checks to ensure the data within a block is usable for physics analyses. Collections of luminosity blocks satisfying the quality requirements are organized into "Good Run Lists" for use by physics analysis groups. This analysis made use of the

following Good Run Lists:

- data15_13TeV.periodAllYear_DetStatus-v105-pro22-13_Unknown_PHYS_Susy_AllGood_DisappearingTrack.xml
- data16_13TeV.periodAllYear_DetStatus-v105-pro22-13_Unknown_PHYS_Susy_AllGood_DisappearingTrack.xml

This analysis made use of SHERPA VV, W+jets, and $Z \to \nu\nu$ Monte Carlo samples simulated with SHERPA v2.2.1 or v2.2.2 [26], depending on the exact process. Fully leptonic and semileptonic processes are calculated at NLO accuracy in QCD for up to one additional parton and at LO accuracy for up to three additional partons. Samples for the loop-induced processes $gg \to VV$ are generated using LO matrix elements for up to one additional parton for both fully leptonic and semileptonic final states. Matrix element calculations are matched and merged with the SHERPA parton shower based on Catani-Seymour dipoles [88, 140] using the MEPS@NLO prescription [98, 99, 35, 100]. The virtual QCD corrections are provided by the OPENLOOPS library [34, 63]. The electroweak $VVjj$ samples are simulated with the Sherpa v2.2.2 generator with LO-accurate matrix elements matched to the parton shower using the MEPS@LO prescription. The `NNPDF3.0nnlo` set of PDFs is used [127] along with the dedicated set of tuned parton-shower parameters established by the SHERPA authors to generate the samples. The production of V+jets, including $Z \to \nu\nu$, is simulated with SHERPA v2.2.1 generator with NLO accuracy for up to two jets and LO accuracy for up to four jets, calculated with the Comix [88] and OPENLOOPS libraries. They are matched with the SHERPA parton shower using the MEPS@NLO prescription using the set of tuned parameters developed by the SHERPA authors. The `NNPDF3.0nnlo` set of PDFs is used and the samples are normalized to a next-to-next-to-leading-order

(NNLO) prediction. The precise Monte Carlo and data sets used in this analysis can be found in Tables F.2, F.3, F.6 and F.8.

Monte Carlo samples of the $Z \to \ell\ell$ process are produced with the PowhegBox v1 [79] at NLO accuracy. PowhegBox is interfaced to Pythia8 8.186 [122] for the parton shower modelling and hadronization, with parameters set according to the `AZNLO` tune [42] with the `CTEQ6L1` PDF set used for the parton shower [133]. QED final-state radiation effects are simulated via Photos++ (v3.52) [89]. The specific $Z \to \ell\ell$ samples used in this analysis can be found in Table F.1.

The production of $t\bar{t}$ events is modelled using the PowhegBox [80, 125, 79, 5] v2 generator at NLO with the NNPDF3.0NLO [127] parton set of distribution functions (PDF) and the h_{damp} parameter[1] set to 1.5 m_{top}. The events are interfaced to Pythia8.230 [147] to model the parton shower, hadronization, and underlying event, with parameters set according to the A14 tune [17] and using the `NNPDF2.3lo` set of PDFs [19]. The decays of bottom and charm hadrons are performed by EvtGen v1.6.0 [61]. The specific samples used in this analysis can be found in Table F.7. The associated production of top-quarks with W bosons (tW) is modelled using the PowhegBox [134, 125, 79, 5] v2 generator at NLO in QCD using the five-flavor scheme and the `NNPDF3.0nlo` set of PDFs [127]. The diagram removal scheme [82]

[1]The h_{damp} parameter is a resummation damping factor and one of the parameters that controls the matching of Powheg matrix elements to the parton shower and thus effectively regulates the high-p_T radiation against which the $t\bar{t}$ system recoils.

is used to remove interference and overlap with $t\bar{t}$ production. The events are interfaced to Pythia8.230 [147] using the A14 tune and the `NNPDF2.3lo` set of PDFs [19]. The specific samples used in this analysis can be found in Table F.5.

The SUSY signal samples used for determining the signal region and estimating the expected sensitivity were all created using Release 21.0 of the ATLAS offline software and were generated during the official MC16a production campaign. All samples were generated at $\sqrt{s} = 13\,\text{TeV}$ with a single configuration of the ATLAS Detector [129] and are simulated with GEANT4 [2] [51].

The signal MC samples used to evaluate expected sensitivity were generated with MadGraph 5 v2.6.2 interfaced to Pythia8.230 and EvtGen v.1.6.0 with `A14` `NNPDF2.3lo` parton distribution functions (PDFs). These samples are reconstructed based on the ATLAS MC16a configuration and using a detector simulation based on GEANT4 with pileup consistent with what is observed in Run 2 data. The mean chargino lifetime $\tau_{\chi^\pm}$ is fixed and charginos are forced to decay via $\chi^\pm \to \chi^0 + \pi^\pm$ following the standard exponential decay with $\tau_{\chi^\pm}$ in the rest frame. Samples with $\tau_{\chi^\pm} = 0.2\,\text{ns}$, $\tau_{\chi^\pm} = 1.0\,\text{ns}$, $\tau_{\chi^\pm} = 4.0\,\text{ns}$, and $\tau_{\chi^\pm} = 10.0\,\text{ns}$ were produced over a mass range from about 400 GeV to about 700 GeV. The MC signal samples used in the analysis are in Table F.4.

The Z tag-and-probe, closure, and signal region selection stages, to be de-

scribed in Section 6.3, Chapter 7.3, and Chapter 5, respectively, make use of the data samples selected by triggers defined in Tables 3.1, 3.2, and 3.3. All of the triggers described in these tables are "High Level Triggers" as described in Section 2.2.5.

Electrons
HLT_e24_lhmedium_L1EM20VH
HLT_e60_lhmedium
HLT_e120_lhloose
HLT_e26_lhtight_nod0_invarloose
HLT_e60_lhmedium_nod0
HLT_e140_lhloose_nod0

Table 3.1: Set of electron triggers used in Z tag-and-probe selection

Muons	
Run Number: 276262 - 284484	Run Number: 297730 - 300279
HLT_mu20_iloose_L1MU15	HLT_mu26_ivarmedium
HLT_mu40	HLT_mu50

Table 3.2: Set of muon triggers used in Z tag-and-probe selection

Run Number Range	Trigger
276262 - 284484	HLT_xe70
296939 - 302872	HLT_xe90_mht_L1XE50
302919 - 303892	HLT_xe100_mht_L1XE50
303943 - 320000	HLT_xe110_mht_L1XE50
320000 - 331975	HLT_xe110_pufit_L1XE55

Table 3.3: E_T^{miss} Triggers

The total integrated luminosity of the collected data is about $36\,\text{fb}^{-1}$, split between $3.4\,\text{fb}^{-1}$ in 2015 and $32.6\,\text{fb}^{-1}$ in 2016, the uncertainty on the integrated luminosity is $\pm 2.1\%$ [114].

Chapter 4

ATLAS Object Reconstruction

The ATLAS Detector reconstructs events based on the signal generated by several stable final state particles: e, γ, μ, π, K, protons and neutrons. Note the μ, π, and K are treated as final state particles because their long lifetimes give them ample time to clear the detector prior to decaying.

4.1 Standard Tracks

The core of the ATLAS Physics program is the identification and reconstruction of charged-particle tracks from the collision point, the primary job of the Inner Detector. The standard tracking algorithm begins with space-points from hits in the Pixel Detector and the SCT, combining these into track-segments which are extrapolated out into the TRT. The track parameters after each active detector element (pixel, strip, or straw) are determined using a combined fit with the Kalman filtering method [83] applied to account for multiple-scattering as the particle traverses the material and

magnetic field of the detector. For the Pixel detector, a space point is determined by a single hit, whereas the SCT combines the hits on both layers of the strip to create a single space-point [46]. Three space-points from the Pixel and SCT detectors are required to seed tracks because this allows for the maximum possible set of tracks while still allowing a crude momentum estimate to be made. "Purity" is defined as the fraction of track seeds which result in good quality tracks and varies significantly between the different sub-detectors of the ID. It is used to determine the order in which different seeds are considered: SCT-only goes first, then Pixel only, then finally mixed-subdetector seeds. Purity is maximized via requirements on the seed-dependent momentum and impact parameter measurements, and is further improved by requiring at least one additional space-point to be compatible with a given seed. These purity requirements eliminate most spurious space-point combinations before the Kalman filter is used, lightening the computational load. The Kalman filter then creates track candidates by incorporating the remaining Pixel and SCT space-points, effectively capturing virtually all of the tracks from primary particles. Nevertheless, there is still ample potential for space-points to be claimed by multiple tracks, requiring resolution of these ambiguities.

Ambiguity resolution is achieved by scoring the track candidates using criteria such that a high score is more likely to correspond to a genuine charged-particle, as one would naïvely expect. Clusters assigned to a track are weighted according to the subdetector resolution and expected cluster multiplicity, the χ^2 of the fit is used as an indicator of the candidate likelihood, and holes in either the Pixel or SCT lower the score. The logarithm of the transverse momentum monotonically improves a track score as transverse

momentum rises, because higher-p_T tracks are more likely to be real, and because there tend to be large numbers of low-p_T tracks with incorrectly-assigned clusters.

Shared clusters, compatible with multiple candidate tracks but incompatible with *merged* clusters, must also be handled by the ambiguity resolver. A given track candidate must have no more than two shared clusters, and a cluster can be shared by no more than two track candidates. For clusters shared between multiple track candidates, priority is given to ones already addressed by the ambiguity solver. Here we are defining d_0^{BL} to be the transverse impact parameter with respect to the beamline, and z_0^{BL} is the displacement along the beamline from the interaction point *at the point where* d_0^{BL} *is measured*, and θ is the polar angle of the track. Finally, basic quality requirements are applied to all track candidates, with any failure causing the candidate to be rejected:

- $p_T > 400\,\text{MeV}$
- $|\eta| < 2.5$ (must be within the Inner Detector)
- At least 7 Pixel + SCT Clusters (12 are expected)
- Maximum of either 1 shared Pixel cluster or 2 shared SCT clusters within the same layer
- No more than two holes between the Pixel and SCT
- No more than one hole in the Pixel detector
- $|d_0^{BL}| < 2.0\,\text{mm}$

- $|z_0^{BL} \sin\theta| < 3.0\,\text{mm}$

Merged clusters are caused by multiple charged particles passing within the resolution of the active material layer. They are identified using a neural network capable of distinguishing single-hit clusters from double and triple-plus clusters; however the neural network is not able to break merged clusters into sub-clusters corresponding to the individual charged particles. To mitigate the false-positive rate, the neural network is consulted only in cases where the cluster is actually used by multiple tracks. The neural network can be confused by the inherent physical interactions when a charged-particle passes through the thin silicon layers, for example emitting δ-rays which make the energy deposit appear larger than expected for a single particle. Because particle tracks tend to diverge as they propagate outward, if two track candidates compete for candidate merged clusters on consecutive layers of the Pixel detector then the inner cluster will be considered as merged if the outer one is classified as merged.

The final step is a high-resolution track fit using all available information, performed on all the high-quality tracks that pass through ambiguity resolution unmodified. Additional neural networks improve the accuracy of the cluster position and uncertainty measurements [36], pinpointing the clusters and their resolutions for the final fit. This step is saved for last because it is computationally-expensive.

After the inside-out extrapolation described above, an outside-in algorithm is applied to TRT hits and remaining silicon hits, extrapolating inwards towards the

collision point instead of away from it. Of primary importance are the track parameters at the *perigee* point, the point along the reconstructed track which is closest to the beamline. The parameter d_0 is the point of closest approach in the transverse plane, and has a resolution of $\approx 10\,\mu$m, while the parameter z_0 is the point of closest approach to the primary vertex along the beamline, and it has a resolution of $\approx 100\,\mu$m.

4.2 Tracklets

The standard tracks described above are fully reconstructed from hits throughout the entire Inner Detector. Pixel tracklets in contrast are constructed only from hits on the four pixel layers, without any contribution from the SCT or the TRT. Pixel tracklets are reconstructed using a "second pass" tracking algorithm which uses only space-points not associated with tracks found by earlier reconstruction algorithms. Tracklets are seeded using only pixel detector space-points, with an explicit rejection of SCT hits known as the "disappearing track" requirement. The transverse momentum and pseudorapidity thresholds are $p_T > 5\,\text{GeV}$ and $|\eta| < 2.2$, respectively. We require there to be at least four pixel hits with no holes, and the tracklet must not share any hits with other tracks. The impact parameter requirements for tracklets are the same as those applied to standard tracks, with the magnitude of the transverse and longitudinal impact parameters being less than $10\,\mu$m and $250\,\mu$m, respectively. Additional criteria are set in the offline selection. Overall tracklets must meet the following requirements:

1. $p_T > 5\,\text{GeV}$

2. $0.1 < |\eta| < 1.9$

3. Number of hits:

   - $N_{\text{Blayer}} \geq 1$, if hits are expected
   - $N_{\text{PixelHits}} \geq 4$ and $N_{\text{ContributedPixelLayers}} \geq 4$
   - $N_{\text{SCTHits}} = 0$
   - $N^{Si}_{\text{Holes}} = 0$
   - $N^{Pixel}_{\text{Outliers}} = 0$ and $N^{Pixel}_{\text{SpoiltHits}} = 0$ and $N^{Pixel}_{\text{GangedFlaggedFakeHits}} = 0$

4. $|\frac{d_0}{\sigma(d_0)}| < 2$ and $|z_0 \sin(\theta)| < 0.5\,\text{mm}$

5. Track-based isolation: $\frac{p_T^{cone40}}{p_T} < 0.04$, with p_T^{cone40} defined as the sum of the p_T of all standard tracks with $p_T > 1\,\text{GeV}$ which pass the "Loose" track selection criteria[1] within a cone of radius $\Delta R < 0.4$ of the tracklet

6. Good χ^2 quality: $Pr\left(\frac{\chi^2}{N_{DoF}}\right) > 0.1$, where N_{DoF} is "Number of Degrees of Freedom"

7. A tracklet must have $p_T > 20\,\text{GeV}$ and have the highest p_T among isolated tracklets within the event

8. Object isolation: $\Delta R > 0.4$ between the tracklet and any jets, electrons, muons, or muon spectrometers tracks, for those objects of sufficient transverse momentum

[1] Loose tracks satisfy: $p_T > 400\,\text{MeV}$, $|\eta| < 2.5$, $N_{Si-Hits} \geq 7$, Number of shared modules ≤ 1, $N^{Si}_{\text{Holes}} < 2$, $N^{Pixel}_{\text{Holes}} \leq 1$ [152]

- Jet: $p_T > 50\,\text{GeV}$
- Electrons and Muons: $p_T > 10\,\text{GeV}$
- Muon Spectrometer tracks: $p_T > 0\,\text{GeV}$

The η requirements are due to a gap in the muon detector ($|\eta| > 0.1$) and the physical extent of the TRT ($|\eta| < 1.9$). Requirements on the number of pixel holes[2], outliers[3], spoilt hits[4], and ganged flagged fake hits[5] are to reduce the number of fakes; criteria 5 - 8 also serve to eliminate fake tracklets, as well as keeping the tracklet isolated. Muon spectrometer tracks are reconstructed using only muon spectrometer hits, and all tracks within the "MuonSpectrometerTrackParticles" container are used for overlap removal (Section 4.7) between the tracklet and muon spectrometer tracks.

4.3 Electrons

Electron reconstruction begins with the identification of energy depositions in the Electromagnetic Calorimeter (ECal). A sliding-window algorithm [68] searches for clusters of size $\Delta\eta \times \Delta\phi = 3 \times 5$ elements, in units of 0.025×0.0245, where the combined transverse energy exceeds the threshold of $E_T > 2.5\,\text{GeV}$. If two such clusters are detected within an area of 5×9 tower elements and they differ by more than 10% in total transverse energy, the cluster with the greatest total energy is retained; if the total energy difference is less than 10%, then the cluster which has the single greatest-E_T

[2] A hole is defined as a detector surface without any associated hit where one is expected.

[3] Outliers are hits associated to a track but deemed too far from the fitted track

[4] Spoilt hits are hits with broad errors, usually produced by neighboring tracks or pure noise not actually affiliated with the track in question.

[5] Ganged flagged fake hits are ganged pixel hits which have been flagged as fake

central tower element is retained; in both cases, the lesser cluster is ignored.

The next phase of electron reconstruction is the track reconstruction in the Inner Detector (ID). Track reconstruction begins with the identification of at least three space-points within the Pixel Detector and Semiconductor Tracker (SCT), the latter of which requires clusters from both stereo views to reconstruct a $3D$ point. These three space-points form the track seeds for the tracking algorithm, which proceeds in three phases: pattern recognition, ambiguity resolution, and TRT extension. Pattern recognition begins with a "pion hypothesis" for modeling the energy loss of the particle through the detector material. Track seeds which fail to be fit with this hypothesis yet exceed the $p_T > 1\,\mathrm{GeV}$ threshold and are within the region of interest of an ECal cluster are subsequently tested against an "electron hypothesis". Either hypothesis is evaluated using the ATLAS Global Fit χ^2 Track Fitter algorithm. Track candidates with at least 4 silicon detector hits and loose matching to ECal clusters are subsequently fit with a Gaussian-sum filter (GSF) algorithm, designed to more accurately account for the energy losses of charged particles passing through the layers of the detector. To be considered "loosely matched", the track candidate must satisfy the following requirements: $|\eta_{\mathrm{cluster}} - \eta_{\mathrm{track}}| < 0.05$ and $-0.20 < q \times [\Delta\phi(\mathrm{cluster}, \mathrm{track})] < 0.05$ or $-0.1 < \Delta\phi_{res} < 0.05$, where $\Delta\phi_{res}$ is the azimuthal separation between the ECal cluster position as evaluated by the second layer and the position of the track at the level of the second layer as projected from perigee with the energy rescaled to that of the ECal cluster and then multiplied by the electric charge q. The $\Delta\phi$ requirement is asymmetric because bremsstrahlung losses for a particle in a magnetic field are more likely

to change the particle's ϕ position in one direction than the other; multiplying the $\Delta\phi$ requirement by the electric charge compensates for positively-charged particles curving oppositely relative to negative-charged ones within the same magnetic field.

The final stage in electron-candidate reconstruction is the matching of the track candidate with the ECal cluster and the determination of the overall size of the given ECal cluster. The matching is functionally similar to the earlier matching though with a stricter $\Delta\phi$ requirement: $-0.1 < q \times [\Delta\phi(\text{cluster}, \text{track})] < 0.05$; the alternative criterion, $-0.1 < \Delta\phi_{res} < 0.05$, remains the same. Electron candidates are those with associated tracks and at least 4 silicon detector hits and no secondary vertex association. The primary is chosen from the set of electron candidates based on the $\Delta\eta$ and $\Delta\phi$ of the extrapolated tracks vs the cluster barycenter in the second layer of the ECal, the number of hits within the SCT and the number of Pixel hits. Candidates originating from a secondary vertex with no pixel hits are considered to be a photon conversion and classified as photon candidates. The final ECal clusters are determined using the same sliding-window algorithm as described previously but extended to either 3×7 units in the barrel or 5×5 units in the endcap. The energy of the final electron candidate is calculated from the ECal cluster, while its trajectory in η and ϕ is determined from the best-matching track candidate. For this analysis, electron candidates are selected using "LooseAndBLayerLLH" [69] quality requirements, as well as $E_T > 10\,\text{GeV}$ and $|\eta| < 2.47$. Electrons used in lepton Control Regions (signal Electrons) are also required to pass "LooseTrackOnly" isolation and "TightLLH" quality. In this analysis, electrons

designated as "signalElectrons", used for both the Z tag-and-probe and the Control Region, satisfy the criteria in Table 4.1: Another class of electrons, "baseElectrons", is

$E_T > 10.0\,\text{GeV}$
$\lvert\eta\rvert < 2.47$
electron is tight
$\frac{ptcone20}{p_T} < 0.10$
$d_0 < 1.0$
$z_0 < 2.0$

Table 4.1: Signal Electron Criteria

also used in the Z tag-and-probe portion of the analysis, these electrons must only pass the criteria in Table 4.2.

$E_T > 10.0\,\text{GeV}$
$\lvert\eta\rvert < 2.47$

Table 4.2: Base Electron Criteria

4.4 Muons

As with electron reconstruction, muon reconstruction involves input from multiple sub-detectors, in this case the Inner Detector and the Muon Spectrometer.

Reconstruction within the Muon Spectrometer begins with the identification of individual segments in the different layers of the device. Within each MDT layer a Hough transform [102] is used to identify straight-line hit trajectories in the bending plane of the detector. In addition to triggering, the RPCs/TGCs provide measurement of the coordinate orthogonal to the bending plane. The Cathode Strip Chambers (CSCs) reconstruct segments using a combinatorial algorithm in the η and ϕ detector planes. The track segments produced by the different layers are then integrated together using segment-seeded combinatorial search, starting initially with the middle layers as those typically have more hits, then expanding to including the inner and outer layers. Segment selection is done using hit multiplicity and fit quality criteria; segments are matched to each other according to relative positions and angles. Outside the transition region $1.4 < |\eta| < 1.6$ a track candidate must have at least two segments to be considered, but within the transition region a single high-quality segment is sufficient. Overlap removal is used to handle cases when multiple track candidates include the same segments, though to ensure high efficiency for close-by muons all candidates are retained in cases where only the third layer differs. The track candidates are then evaluated using a global χ^2 fit, made more robust by dropping hits with especially large contributions to the χ^2 value and refitting without them as well as adding in additional plausible hits missing from the initial segments being added in and refit.

There are four muon *types* defined according to which sub-detectors and algorithms are used to reconstruct them, although only the Combined Muons concern

us here. Combined Muons are defined as those which have been reconstructed by the Inner Detector and the Muon Spectrometer independently and then fit using a global χ^2 fit, again made robust via the addition (deletion) of plausible hits missing from the track candidate (hits with unusually large impact on the fit). Typically, the global fit procedure is done from the outside-in, extrapolating MS track candidates inwards to the Inner Detector, with an inside-out fit done next to complement it.

This analysis is primarily concerned with Combined (CB) Muons, which utilize three variables to distinguish them from the light-hadron decay background. These variables are:

- $\frac{q}{p}$ significance: the absolute value of the difference in ratios as measured by the Inner Detector and Muon Spectrometer divided by the sum in quadrature of the uncertainties of those measurements. Symbolically: $\sigma(\frac{q}{p}) = \frac{\left|\left(\frac{q}{p}\right)_{ID} - \left(\frac{q}{p}\right)_{MS}\right|}{\sigma\left(\frac{q}{p}\right)^2_{ID} + \sigma\left(\frac{q}{p}\right)^2_{MS}}$
- ρ': the magnitude of the difference between the transverse momentum measurements of the Inner Detector and Muon Spectrometer, divided by the transverse momentum of the combined fit. Symbolically: $\rho' = \frac{|p_T^{ID} - p_T^{MS}|}{p_T^{Global}}$
- χ^2: the normalized χ^2 of the combined track fit

Within the Inner Detector, combined muons must have at least 1 Pixel hit, at least 5 SCT hits, and fewer than 3 Pixel or SCT holes. Within the region of full TRT acceptance, ($0.1 < |\eta| < 1.9$), at least 10% of hits from the original track must be retained in the final version. This analysis makes use of two classes of muons, high-

quality “signalMuons” and lower-quality “baseMuons”, with signalMuons used for both the Z tag-and-probe and the Control Region. As with the electrons, the Z tag-and-

$p_T > 10.0\,\text{GeV}$
$\lvert\eta\rvert < 2.5$
$ptcone20 < 1.80\,\text{GeV}$
$d_0 < 0.2$
$z_0 < 1.0$

Table 4.3: Signal Muon Criteria

probe portion of this Analysis makes use of a second, broader class called “baseMuons”, which only have the p_T and η requirements without isolation impact parameter criteria as seen in Tables 4.3 and 4.4.

$p_T > 10.0\,\text{GeV}$
$\lvert\eta\rvert < 2.5$

Table 4.4: Base Muon Criteria

4.5 Jets

Jets are narrow cones of hadrons produced via the process of hadronization when color-charged particles are ejected from the collision point. Because the LHC is a hadron collider, jets are a ubiquitous feature of collision events and therefore accurate

jet measurement and reconstruction are critical for most of the physics programs in ATLAS.

Topological clusters (topo-clusters) [54], sets of adjacent cells with energy above threshold, are seeded by calorimeter cells with energy at least 4 times higher than the background from estimated electronic and pile-up noise, with neighboring cells containing at least twice the background level added in and then all immediately adjacent cells with any energy content added as well. A splitting algorithm is applied to split topo-clusters into at most two local maxima. Calorimeter cell energies are measured at the level of the energy deposited by electromagnetically-interacting particles. The topo-clusters are fed into an anti-k_t algorithm [32], provided they exceed a threshold of $p_T > 7\,\text{GeV}$.

The entire range of the Inner Detector, ($|\eta| < 2.5$) is used to identify tracks for matching with jets, with quality requirements for each ID sub-detector applied. These reconstructed tracks are required to have $p_T > 500\,\text{MeV}$ and be associated with the hard-scatter vertex, defined as the primary vertex with at least two associated tracks and the largest sum of p_T^2 of associated tracks. Ghost association, in which tracks are treated as four-vectors of infinitesimal magnitude during the jet reconstruction phase, assigns the tracks to the jets with which they are clustered.

Muon Spectrometer segments geometrically associated to jet clusters are used as proxies for the uncaptured jet energy, carried away by charged particles not fully absorbed in the calorimeters. As with tracks in the Inner Detector, these MS segments

are ghost associated to the jet clusters.

To mitigate the effects of cosmic rays and large calorimeter noise, jets are required to pass the "loose" isolation criteria described in the paper [40]. Acceptance cuts of $p_T > 20\,\text{GeV}$ and $|\eta| < 2.8$ are applied, as well as a default jvt(0.59) to signal jets.

4.6 E_T^{miss}

Not all particles leave traces within the ATLAS detector: the Standard Model neutrinos sail through the detector without leaving a trace, as do any Beyond Standard Model (BSM) particles which could plausibly contribute to dark matter. But these particles must still obey the fundamental translational invariance of space: momentum must be conserved, allowing otherwise invisible particles to be detected as imbalances in the collective transverse momentum of the particles which *are* directly detected.

Two categories of objects go into E_T^{miss} reconstruction: *hard objects*, based on fully-reconstructed and calibrated objects, and *soft objects*, based on reconstructed tracks associated to the hard-scatter vertex but not to any hard objects. Hard objects include photons, charged leptons, and jets, while soft objects are low energy scattered particles arising from the same underlying event or from pile-up. Photons and jets are reconstructed using calorimeter clusters, electrons and τ-leptons are reconstructed via

ID tracks and calorimeter clusters, and muons are reconstructed by ID tracks matched with MS tracks. In order to prevent multi-counting the same objects, a strict hierarchy is imposed on hard-object reconstructions, with low-priority objects being fully rejected if they share calorimeter signals with high-priority ones. Electrons have top priority, then photons, then hadronically-decaying taus (τ_{had}), then finally jets. Muons, being reconstructed from ID and MS tracks with little deposit in the calorimeters, don't typically have much overlap with the other hard objects, although non-isolated muons sometimes overlap with τ_{had} and jets.

The missing transverse momentum is calculated from the transverse momenta of the selected jet and lepton candidate objects described above, along with tracks which are not associated with such objects (called "track soft term"):

$$\vec{p_T}^{miss} = -\sum \vec{p_T}^{jet} - \sum \vec{p_T}^{electron} - \sum \vec{p_T}^{muon} - \sum \vec{p_T}^{track}; \tag{4.1}$$

the METMaker package [37] removes any object overlap. The magnitude of $\vec{p_T}^{miss}$ is E_T^{miss}, and soft tracks are defined as:

1. passed "TightPrimary" track selection
2. $|\frac{d_0}{\sigma(d_0)}| < 2$
3. $|z_0 \sin(\theta)| < 3.0\,\text{mm}$
4. For isolated high-p_T tracks, either of the following are satisfied:
   - $\frac{E_T^{clus10}}{p_T} < 0.1$ and $|\frac{\sigma(\frac{q}{p})}{\frac{q}{p}}| < 0.1$

- $\frac{E_T^{clus10}}{p_T} > 0.65$ and $|\frac{\sigma(\frac{q}{p})}{\frac{q}{p}}| < 0.4$

5. For non-isolated high-p_T track, either of these are satisfied:

- $\frac{E_T^{clus10}}{(p_T + p_T^{cone20})} > 0.6$
- $\frac{p_T}{(p_T + p_T^{cone20})} < 0.6$

Pixel tracklets are not included in the E_T^{miss} track soft term calculation.

4.6.1 E_T^{miss} with Invisible Leptons

Part of this analysis is concerned with leptons which fail to be reconstructed due to scattering in the Inner Detector. In this case the relevant E_T^{miss} calculation is done treating these electrons and muons as if they are invisible. This use of E_T^{miss} with invisible leptons will be discussed in Chapter 7.1.

4.7 Overlap Removal

When there is overlap between the aforementioned physics objects, one object will be removed according to the following hierarchy:

1. If an electron candidate and a muon candidate share the same ID track, the muon is removed if the muon is a calo-muon and the electron is removed otherwise

2. If an electron candidate and a jet are found within $\Delta R < 0.2$, they are treated as one electron and the jet is removed

3. If an electron candidate and a jet are found within $\Delta R < 0.4$, they are classified as one jet and the electron is removed

4. If a muon candidate and a jet are ghost-associated or found within $\Delta R < 0.2$, they are classified as one muon and the jet is removed as long as the number of tracks with $p_T > 500\,\text{MeV}$ associated to the jet is less than three

5. If a muon candidate and a jet are found within $\Delta R < 0.4$, they are classified as one jet and the muon is removed

4.8 Event Cleaning

Detector Error Veto: Rejection of bad or corrupted events due to detector error is an ATLAS-wide recommendation.

Bad Jet Cleaning: First, an event is rejected if any jets fail to pass the loose jet cleaning ("LooseBad") requirement. Second, events are rejected if the leading jet fails to pass the tight jet cleaning ("TightBad") requirement or if it has $|\eta| > 2.4$. The cleaning criterion is for reducing the non-collision background and the leading jet must be within the Inner Detector region because Inner Detector track information is used in the "TightBad" requirement.

Bad Muon Event Veto: Badly reconstructed muons can affect the E_T^{miss} calculation, particularly in the tails, therefore the event is rejected if a baseline muon before overlap removal satisfies this condition: $\left(\frac{\sigma(\frac{q}{p})}{\frac{q}{p}}\right) > 0.4$.

Bad Muon $E_T^{\mathbf{miss}}$ Cleaning: Some poorly reconstructed muons will get past the above bad muon event veto, so we eliminate events which meet the following criterion:

$$\frac{E_T^{\text{miss,muon}}}{E_T^{\text{miss}}} \cos\Big(\phi(E_T^{\text{miss,muon}}) - \phi(E_T^{\text{miss}})\Big) > 0.5 \tag{4.2}$$

where $E_T^{\text{miss,muon}}$ is the muon component of E_T^{miss}, the negative vector sum of the muon $\vec{p_T}$.

Chapter 5

Signal Region Selection

The signal region selection for this analysis is simple relative to most ATLAS SUSY searches because most of the discriminating power comes from the tracklet definition. Object Reconstruction is described in detail in Chapter 4.

A lepton veto, rejecting any events with electron or muon candidates, is applied to reduce the background from $t\bar{t}$ and $W/Z+$ jets, and at least one isolated tracklet, as described in Section 4.2, with $p_T > 20\,\text{GeV}$ is required. These requirements, together with the event cleaning described in Section 4.8, constitute the "Event Pre-selection".

The kinematic selection criteria were determined first and foremost by the efficiency of the E_T^{miss} trigger, which reaches maximum efficiency at about 200 GeV. In order to boost the charginos coming from the primary vertex, we require a hard jet with $p_T > 150\,\text{GeV}$, and to reduce the QCD background we require the up-to

four highest-p_T jets above a threshold of 50 GeV to be separated from the E_T^{miss} by $|\Delta\phi(jet, E_T^{\text{miss}})| > 1.0$. The ATLAS Disappearing Track group further justified these specific thresholds via comparison between a representative AMSB 600 GeV $\chi^{\pm}$ model and several Standard Model backgrounds scaled to the full Run 2 data, as seen in the following figures. For E_T^{miss}, we can see in Figure 5.1 that the chargino signal has a strong turn-on at around 200 GeV while the backgrounds have a significant contribution with $E_T^{\text{miss}} < 200$ GeV, thus we require $E_T^{\text{miss}} > 200$ GeV to enhance signal over background. Because the E_T^{miss} in the signal arises from recoil against a jet, this is accompanied by a matching jet with $p_T^{\text{leadjet}} > 150$ GeV in order to boost the system. As a result, the great majority of the signal has a leading jet $p_T^{\text{leadjet}} > 150$ GeV so we place a cut here, as shown in Figure 5.2. Finally, in order to suppress the QCD background, each of the up to four jets with $p_T > 50$ GeV must be well-separated from the E_T^{miss}. We thus require that the minimum $\Delta\phi(jet, E_T^{\text{miss}})$ over these up-to four jets be greater than 1.0, as shown in Figure 5.3. The full set of selection criteria is summarized in Table 5.1.

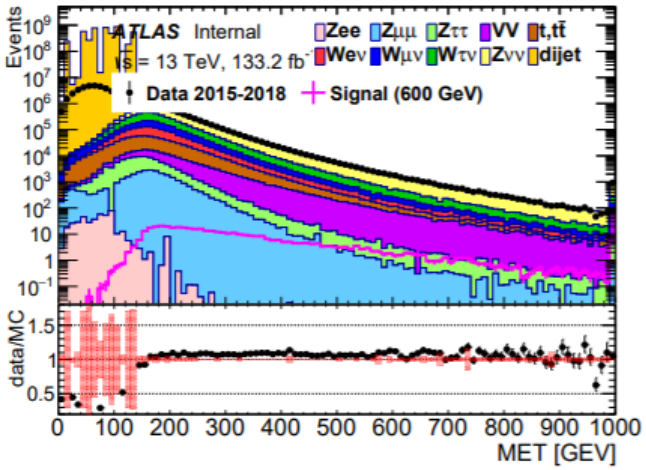

(a) $E_{\mathrm{T}}^{\mathrm{miss}}$

Figure 5.1: $E_T^{\mathrm{miss}} > 200\,\mathrm{GeV}$ Cut

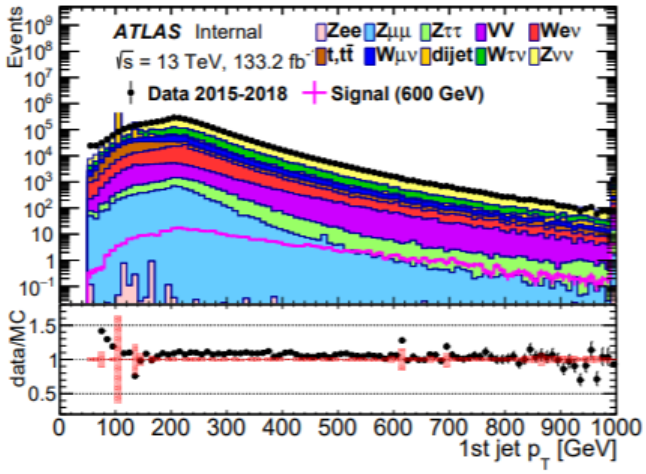

(b) 1st jet p_{T}

Figure 5.2: Lead Jet $p_T > 150\,\mathrm{GeV}$ Cut

Pre-selection
GoodRunList
Reject if lead jet passes "BadTight" selection
Reject if any jet passes "BadLoose" selection
E_T^{miss} Trigger
Reject if electron or muon candidates present (lepton veto)
Main Selection
Must have 1 tracklet
$E_T^{\text{miss}} > 200\,\text{GeV}$
$p_T^{\text{leadjet}} > 150\,\text{GeV}$
$\lvert\Delta\phi(jet, E_T^{\text{miss}})\rvert > 1.0$ for up to 4 jets with $p_T > 50\,\text{GeV}$

Table 5.1: Event Preselection and Main Selection

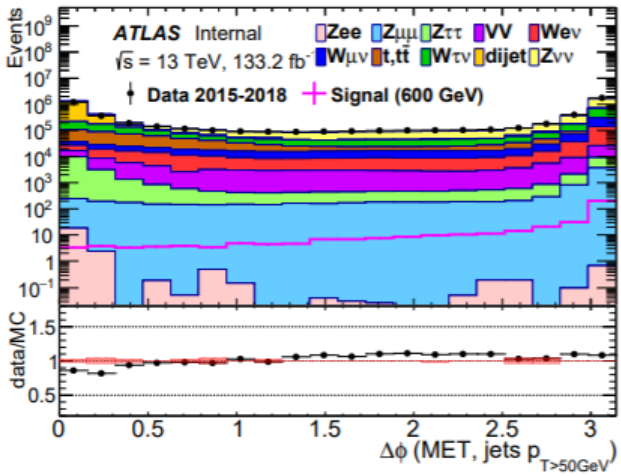

(c) $\Delta\phi_{\text{min}}^{\text{jet}-\text{E}_{\text{T}}^{\text{miss}}}$

Figure 5.3: $|\Delta\phi(\text{Jet}, E_T^{\text{miss}})| > 1.0$ Cut

Chapter 6

Defining the Lepton Transfer Factors

The major thrust of this dissertation is an analysis characterizing and quantifying the lepton scatter background to the chargino disappearing track signature. This is done by defining a Single Lepton Control Region, orthogonal to the chargino Signal Region and using a transfer factor to estimate the number of lepton scatters within the Signal Region itself.

6.1 Motivation

As described in the introductory chapters, the signal we are searching for is generated by near-degenerate electroweakinos with masses of a few hundred GeV, capable of being directly produced at the LHC. The near-degeneracy grants the chargino a lifetime sufficient to traverse the Pixel Detector before decaying to a neutralino and a charged pion before reaching the SCT. The key signature of this process is a disappearing

track: a partial track through the Pixel Detector without any continuation in the rest of the ATLAS Detector. Electrons and muons which Coulomb scatter off nuclei at a steep angle after leaving several consecutive pixel hits are a major background to this signature that must be characterized in order to properly search for this process, and by extension evaluate the validity of nearly-degenerate gaugino models. Below we describe the method used to estimate the lepton scatter background for the 2015 and 2016 Run 2 data.

6.2 Description of the Background Estimation Approach

This analysis determines and utilizes a Transfer Factor and a Single Lepton Control Region in order to estimate the lepton scatter background for the disappearing track signature. The Transfer Factor represents the probability that a lepton (electron or muon) is mistakenly reconstructed as a signal-quality tracklet. A Z tag-and-probe method is used to estimate the Transfer Factor, as a function of lepton η and p_T, from Run 2 data taken in 2015 and 2016 (see Section 3). Events are selected in the Single Lepton Control Region, and the number of lepton scatters which would mimic a disappearing track, binned in p_T and η, is estimated by multiplying bin-by-bin the number of events in the Control Region by the Transfer Factor. This process is done separately for electrons and muons, and the results are then summed together to provide an overall estimate of the background.

The validity of the method is supported using a Closure Test performed solely with Monte Carlo samples. Uncertainties resulting from non-closure were incorporated directly into the Transfer Factor along with the uncertainties in the direct calculation of the Transfer Factor. The uncertainties in the parameters used for the smearing of lepton transverse momentum, to be described in Section 7.4, were treated as a systematic uncertainty envelope around the nominal expected background.

6.3 Z tag-and-probe Methodology: Determining the Transfer Factor

Our strategy for determining the background contribution from electron and muon Inner Detector scatters is to use real Run 2 data and a Z tag-and-probe approach to create Transfer Factor Maps, binned in p_T and η; this is done separately for electrons and muons. (When the backgrounds are estimated, the estimates for electrons and muons are summed together). Both Transfer Factor Maps are produced using $Z \to \ell\ell$ events in data as a Z tag-and-probe method, where one lepton is designated the "tag", used to identify the event, while the other is the "probe" used to measure the lepton (electron or muon) contribution to tracklet misidentification "probability".

6.3.1 Electron Transfer Factor

The electron contribution can be described by the following relation:

$$f^e_{SR}(\eta, p_T) = N^e_{CR}(\eta, p_T) \times TF^e_{\text{tracklet}}(\eta, p_T), \tag{6.1}$$

where f^e_{SR} is the electron scatter background in the signal region, N^e_{CR} is the number of electrons in the Control Region (to be defined below), and TF^e is the Transfer Factor expressing the probability that an electron fakes a signal tracklet.

The Transfer Factor can thus be defined as:

$$TF^e_{\text{tracklet}}(p_T, \eta) = \frac{N_{\text{tracklet}}(p_T, \eta)}{N_{\text{electrons}}(p_T, \eta)}. \tag{6.2}$$

Here, N_{tracklet} refers to the number of electrons which satisfy the disappearing track condition $N_{\text{SCT}} = 0$, while the term $N_{\text{electrons}}$ is the number of electrons satisfying the signal conditions described in Table 6.1.

The idea behind the tag-and-probe method is to identify a clean sample of leptons (electrons in this case) that can be used to determine the probability that an electron is mistakenly reconstructed as a tracklet. In order to do this, we must have *a priori* knowledge that the object is in fact an electron, even if the object is reconstructed as a tracklet. We do this by requiring that the object, when combined with a signal-quality electron, has an invariant mass close to the known mass of the Z. This identifies the object of interest as having a high likelihood of being an electron, and allows us to determine the fake fraction. In addition, tracklets not arising from electrons will not be the result of a Z boson decay so their mass distribution when combined with a signal-quality electron will not exhibit the characteristic peaking behavior associated with the

Z resonance. This allows for a clean subtraction of non-electron backgrounds from the tag-and-probe sample.

The tag-and-probe sample is selected with the single electron triggers described in Table 3.1. The event cleaning cuts described in Section 4.8 are applied to provide a robust and clean sample of Z-boson events. The triggering object is further refined by requiring it to be a signal electron as described in Table 4.1, exceeding a transverse momentum threshold of 30 GeV. The resulting object is called the "tag".

Within the same tagged event, the "probe" is a calorimeter cluster chosen by systematically checking each cluster with *all* of the "baseElectrons", defined according to the criteria in Table 4.2, against the following criteria:

- $\Delta R(\text{cluster}, \text{tag}) > 0.2$: cluster is not spatially matched to the tag
- baseElectron has $\Delta R(\text{cluster}, \text{baseElectron}) < 0.2$: cluster is spatially matched to a baseElectron
- Cluster minimizes $|M_{\text{cluster+tag}} - M_Z|$: cluster is the closest to matching a proper Z-boson out of all the baseElectron-associated clusters

Probes reconstructed in this way are considered reconstructed electrons and form the sample for which the denominator of the transfer factor is drawn. If there is no baseElectron other than the tag (signalElectrons are a subset of baseElectrons) spatially matched to a calorimeter cluster, then a second cluster-matching attempt is made by

systematically comparing each calorimeter cluster with the *leading* tracklet using the following criteria:

- $\Delta R(\text{cluster}, \text{tag}) > 0.2$: cluster is not spatially matched to the tag
- $\Delta R(\text{cluster}, \text{tracklet}) < 0.2$: cluster is spatially matched to the tracklet
- $\Delta R(\text{cluster}, \text{tracklet})$ is minimized: no other cluster is physically closer to the leading tracklet

Probes reconstructed in this way are considered reconstructed electrons and form the sample for which the numerator of the transfer factors is drawn. The decision to use the leading tracklet for the matching is not unquestioned. Though it naïvely makes sense for the highest transverse-momentum tracklet to be the most likely to be real, the momentum resolution of the tracklets is much poorer than for electrons or muons or pretty much anything else, so the "leading" tracklet may not actually be so. The other primary option considered for this matching is "tracklet whose associated cluster, together with the tag object, is closest to the Z mass", in analogy to what is done with the baseElectrons. At the time of writing, this other option had not been thoroughly investigated. However, the Closure Test, in which the same method is applied to MC, indicates that our choice of tracklet is at least adequate.

Table 6.1 summarizes the selection criteria for the numerator and the denominator of the Transfer Factor calculation. In both cases, the calorimeter cluster defines the kinematics of the probe. In particular, the mass of the tag+probe system is calcu-

lated from the calorimeter cluster associated with the probe, and not the reconstructed momentum of the lepton's track or tracklet. This is necessary because the short lever arm of the tracklet provides little information on the magnitude of the tracklet momentum. Events in which *neither* of the above sets of criteria are satisfied are rejected, which is why the term we are calculating is a "Transfer Factor" instead of a pure probability.

6.3.2 Muon Transfer Factor

The muons were handled in an analogous manner to the electrons, with a muon satisfying the "signalMuon" requirements described in Table 4.3 used as the tag and an msTrack used as the probe. The equation describing the muon background is:

$$f^{\mu}_{SR}(p_T, \eta) = N^{\mu}_{CR}(p_T, \eta) \times TF^{\mu}_{\text{tracklet}}(p_T, \eta). \tag{6.3}$$

The Transfer Factor for muons is much the same as for the electrons: it effectively converts from the overall number of muons in the Control Region to the number of muons which fit the disappearing track condition $N_{SCT} = 0$, and so can be written as:

$$TF^{\mu}_{\text{tracklet}}(p_T, \eta) = \frac{N_{\text{tracklet}}(p_T, \eta)}{N_{\text{muons}}(p_T, \eta)}. \tag{6.4}$$

The msTracks other than the one ΔR-matched to the tag are checked for "baseMuons", defined in Table 4.4 as satisfying both the $\Delta R < 0.2$ requirement and the "closest mass to the Z when combined with tag" requirement. And again, if no such baseMuons are found and there is at least one tracklet, then the leading tracklet is checked for spatial matching with any of the Muon Spectrometer tracks other than the one associated with

the tag. Table 6.2 summarizes the selection criteria for the numerator and the denominator of the Transfer Factor calculation.

6.3.3 Fitting the Z Peak

The purpose of this analysis is to determine the rate at which leptons satisfy the disappearing track conditions. It requires knowing with high confidence that a given tracklet originated as a lepton. This is why we fit a Z peak: a Z boson has a clean, two-lepton decay with a mass-distribution peak, so seeing a combination of tag lepton and probe tracklet with an invariant mass near the Z peak identifies the tracklet as having a high likelihood of being reconstructed from the partner lepton to the tag. One might naïvely expect a simple ratio of "Events with one lepton and one tracklet" vs "Events with two leptons" would suffice, however there would be a significant contribution to the Single Lepton Control Region from events in which a hadron produces the tracklet. These events would not show any clear peaking behavior in the "lepton + tracklet" mass-distribution, so we can separate the contribution from signal and background by fitting the data in the region of the Z resonance to a hypothesis of a Z-boson mass peak and a slowly varying background. The resulting integral of the peaking component will be the contribution due to lepton-tracklet fakes.

The RooFit framework is used within a Python wrapper to fit the Z-peak within bins defined by the kinematic variables of the "probe". The probe may be either a calorimeter cluster (for electrons) or Muon Spectrometer track (muons) in order to determine

the respective Transfer Factors. A Breit-Wigner[1] + Landau[2] signal on top of a falling exponential background was used to fit the Z-peak and determine the relative contributions of signal and background.

Within each kinematic bin, two fits were made: a tracklet-probe "numerator" of events with a single tag-lepton and a tracklet, with the invariant mass of the combined tag + probe required to be within a certain range of the mass of the Z, 25 GeV for electrons and 30 GeV for muons; and a lepton-tag "denominator" with two same-flavor leptons in which the tag has triggered the event and with the invariant mass of the combined leptons is within the appropriate range of M_Z for the lepton type. Dividing the signal-component of the "numerator" by that from the "denominator" yields a transfer factor. Doing this in each kinematic variable bin yields the Transfer Factor Maps. The transfer factor being computed within each bin is:

$$TF = \frac{N_{\text{tracklet-probe}}}{N_{\text{lepton-probe}}} \tag{6.6}$$

where $N_{\text{tracklet-probe}}$ means "Number of events within the Z-peak with a lepton tagging the event and a tracklet probe" and $N_{\text{lepton-probe}}$ means "Number of events within the

[1]The Breit-Wigner distribution is a symmetric function describing the systems close to a resonance, for example the decay of a particle, and so is a natural "guess" to use to fit a $Z \to \ell\ell$ decay process. There are two parameters of interest: the width Γ and the resonance value E_0; the equation for Breit-Wigner is:

$$f(E) = \frac{(\frac{\Gamma}{2})^2}{(E_0 - E)^2 + (\frac{\Gamma}{2})^2} \tag{6.5}$$

[2]The Landau distribution is asymmetric, with a steep rise to the peak and "fat tail" on the drop-off. This function is usually used in particle physics to describe the energy deposition of charged particles passing through thin layers of matter. The function describing Landau is too complex to be useful here, for our purposes it is described by the location of the peak and the width, which in RooFit is defined to be 0.25 times the full-width-at-half-maximum. The details of the Landau distribution can be found in [109].

Z-peak with a lepton tagging the event and a same-flavor lepton probe". In principle we want to also require the leptons to be of opposite-sign to reduce the contributions from fakes, however the tracklet p_T resolution is poor enough to render charge identification a rather uncertain enterprise, and the number of events with two real same-sign leptons which sum to the Z-peak is below one percent.

To calculate the numerator $N_{\text{tracklet-probe}}$, the Z-peak is fit with a linear combination of a Breit-Wigner plus Landau signal on a falling exponential background, as described previously, to the probe events in each η and p_T bin. The fit determines the relative size of the signal, which gets multiplied by the integral of the histogram. The same procedure is done to calculate the denominator $N_{\text{lepton-probe}}$.

The set of selection criteria used for the numerator and denominator are described in Tables 6.1 and 6.2.

Two-Electron (Denominator)	**Electron + Tracklet** (Numerator)
Tag is an Electron	Tag is an Electron
Tag triggered the Event	Tag triggered the Event
$\lvert M_{tag+probe} - 91.19\rvert < 25\,\text{GeV}$	$\lvert M_{tag+probe} - 91.19\rvert < 25\,\text{GeV}$
Probe identified by Electron	**Probe identified by Tracklet**

Table 6.1: Electron Z tag-and-probe Selection Criteria

Examples of the electron fit in data, for both numerator and denominator,

Two-Muon (Denominator)	**Muon + Tracklet** (Numerator)
Tag is a Muon	Tag is a Muon
Tag triggered the Event	Tag triggered the Event
$\lvert M_{tag+probe} - 91.19\rvert < 30\,\text{GeV}$	$\lvert M_{tag+probe} - 91.19\rvert < 30\,\text{GeV}$
Probe identified by Muon	**Probe identified by Tracklet**

Table 6.2: Muon Z tag-and-probe Selection Criteria

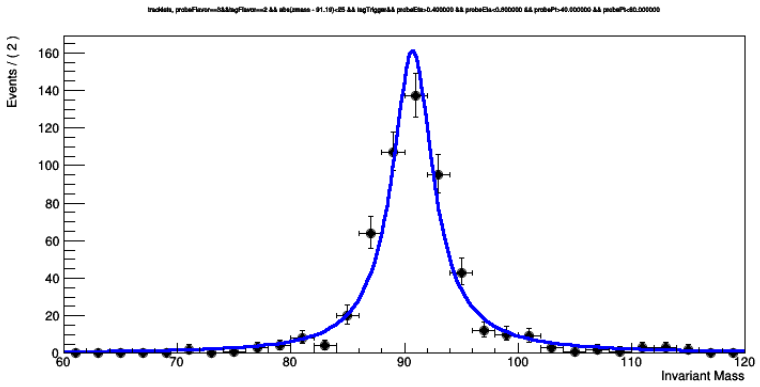

Figure 6.1: Electron Breit-Wigner + Landau Fit for Tracklet Probe, $0.4 < \eta < 0.8$ and $40 < p_T < 60\,\text{GeV}$ bin

are shown in Figures 6.1, 6.2, 6.3, and 6.4. The rest of the fit plots can be found in Appendix D. The final Transfer Factor Maps, for both electrons and muons, are shown in Figure 6.5 and Figure 6.6.

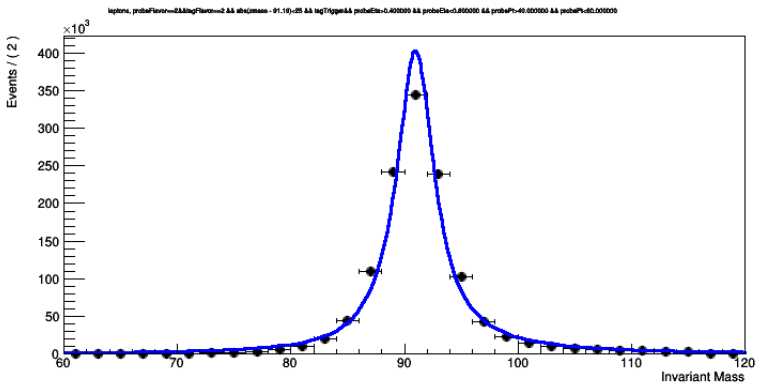

Figure 6.2: Electron Breit-Wigner + Landau Fit for Lepton Probe, $0.4 < \eta < 0.8$ and $40 < p_T < 60\,\text{GeV}$ bin

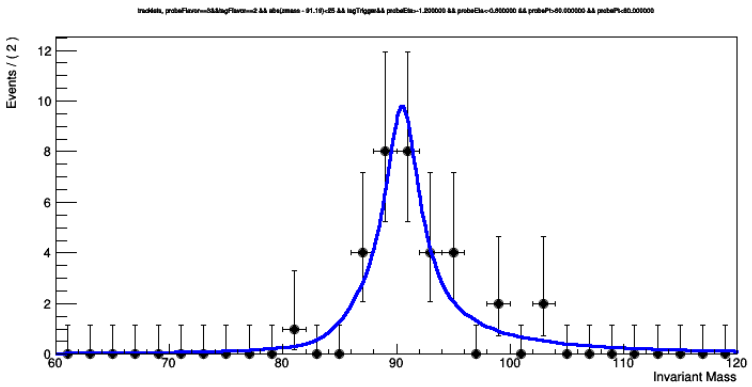

Figure 6.3: Electron Breit-Wigner + Landau Fit for Tracklet Probe, $-1.2 < \eta < -0.8$ and $60 < p_T < 80\,\text{GeV}$ bin

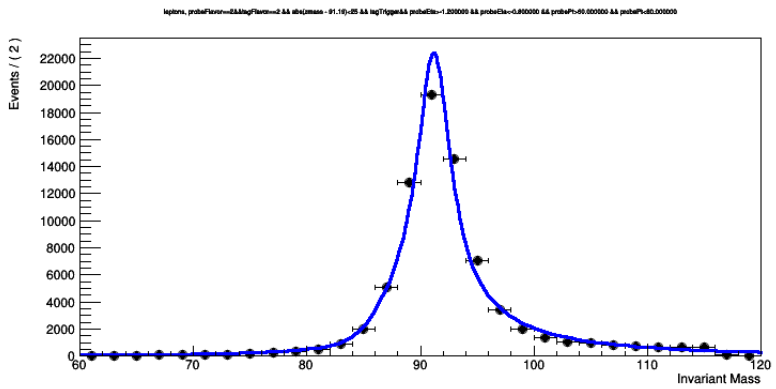

Figure 6.4: Electron Breit-Wigner + Landau Fit for Lepton Probe, $-1.2 < \eta < -0.8$ and $60 < p_T < 80\,\text{GeV}$ bin

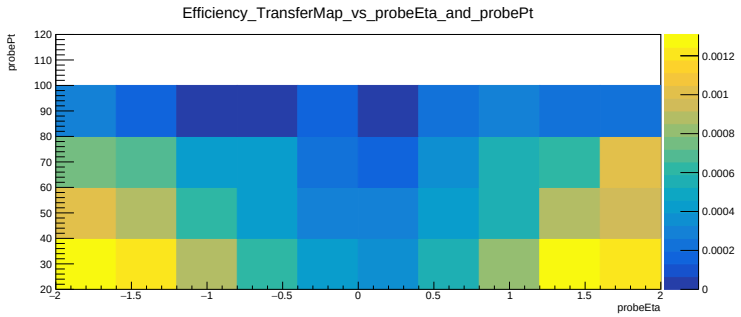

Figure 6.5: Electron Transfer Factor Map

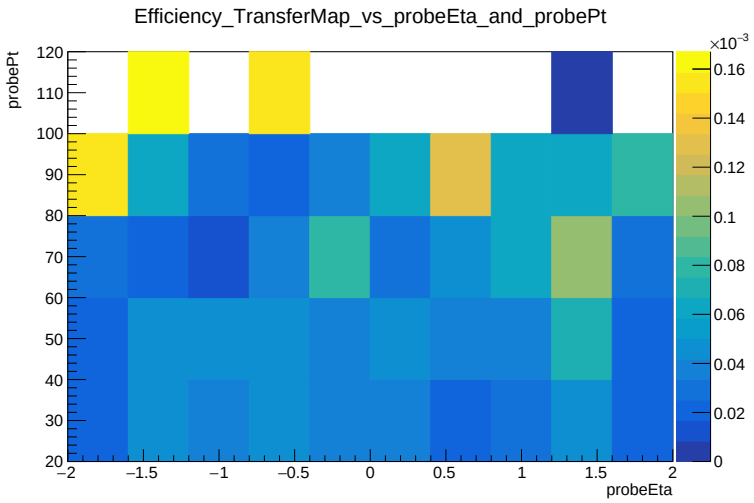

Figure 6.6: Muon Transfer Factor Map

Chapter 7

Estimating the Lepton Scatter Background

Having established the overall background estimation strategy and obtained the Transfer Factor Maps, we establish the Control Region, smear the lepton p_T spectrum to that of the tracklet p_T spectrum, confirm the validity of the strategy via a Closure test, determine systematic uncertainties, and finally extract the lepton scatter background and uncertainties. We then end with a brief consideration of chargino performance in the Signal Region based on Monte Carlo.

7.1 Control Region Definition

For this analysis we use a Single Lepton Control Region made orthogonal to the Signal Region by replacing the Tracklet requirement with a single lepton satisfying

the signal lepton criteria described in Tables 4.1 (electrons) and 4.3 (muons). A point to emphasize is that this Control Region does *not* require $N_{SCT} = 0$, and in addition the transverse momentum minimum is only 10 GeV for electrons or muons, versus 20 GeV for tracklets, in order to ensure the lowest tracklet p_T bin is properly populated after the lepton smearing. The event selection for the Single Lepton Control Region is defined by the following cuts:

- Must have 1 signal lepton
- $E_T^{miss,IL} > 200\,\text{GeV}$
- $p_T^{leadjet} > 150\,\text{GeV}$
- $\Delta\phi(jet, E_T^{\text{miss}}) > 1.0$ for up to 4 jets with $p_T > 50\,\text{GeV}$

The Control Region uses the set of single lepton triggers listed in Table 3.1 and 3.2, as well as the E_T^{miss} triggers described in Table 3.3. It is also important to note that the calculation of E_T^{miss} for the Control Region must treat the lepton as if it were *invisible*, because a scattered lepton would not be reconstructed as a lepton and so would contribute to the E_T^{miss}. This does have the effect of preferentially selecting harder leptons, because a high-p_T lepton will contribute more to the E_T^{miss} if it is treated as invisible than a low-p_T lepton would. This results in the Control Region being moderately enriched in high-p_T leptons relative to the case where the E_T^{miss} is calculated without treating the lepton as invisible.

7.2 Lepton p_T Smearing

Fully reconstructed electrons and muons have much better p_T resolution than tracklets due to the much longer lever-arm, with transverse momentum resolution generally scaling as $\frac{\Delta p_T}{p_T} \propto \frac{1}{L_T^2}$, where L_T is the length of the reconstructed track segment projected into the transverse plane. A tracklet will typically have $L_T = 0.1225\,\text{m}$ while an electron which reaches the ECal has $L_T > 1.0\,\text{m}$. The result is that the electron has a resolution more than 64 times better than the tracklet. Consequently, after weighting by the p_T- and η-dependent Transfer Factor to get the inherent p_T and η distribution, the p_T distribution must be smeared to reflect that of leptons reconstructed as tracklets. Lepton tracks in the control sample were smeared to produce a p_T resolution that reflects that of the reconstructed pixel tracklets. The degree of smearing was determined by re-tracking electrons and muons using only the 4 Pixel Detector hits to create "artificial tracklets"; this was done with Run 2 data using select $Z \to \ell\ell$ events satisfying the following criteria:

- Event must pass the cleaning cuts described earlier and be in the relevant GRL described in Section 3
- Single isolated lepton trigger
- Require two same-flavor leptons and no leptons of any other flavor
- Reconstructed di-lepton mass must satisfy $|M_{\ell\ell} - M_Z| < 10\,\text{GeV}$
- Leading lepton $p_T > 25\,\text{GeV}$

- Sub-leading lepton $p_T > 20\,\text{GeV}$
- Artificial pixel tracklets overlap with lepton-object tracks found by standard tracking, $\Delta R(\text{tracklet}, \text{lepton-object}) < 0.2$

Finally, the disappearing track conditions were also applied to the artificial tracklet, without the lepton veto and p_T requirements.

In ATLAS tracking, $\frac{q}{p_T}$ is the Gaussian-smeared track parameter related to curvature. With the artificial tracklets in hand, the difference

$$\Delta\frac{q}{p_T} = \left|\frac{q}{p_T^{tracklet}}\right| - \left|\frac{q}{p_T^{full}}\right| \tag{7.1}$$

was fit using a double-sided Crystal Ball function [148], described by this equation:

$$f(z) = \begin{cases} exp(\alpha(z + \frac{\alpha}{2})), & (z < -\alpha) \\ exp(-\frac{z^2}{2}), & (-\alpha < z < \alpha) \\ exp(-\alpha(z - \frac{\alpha}{2})), & (z > \alpha) \end{cases} \tag{7.2}$$

The variable z is defined as:

$$z \equiv \frac{\Delta(\frac{q}{p_T}) - \beta}{\sigma}. \tag{7.3}$$

An example fit can be seen in Figure 7.1.

The parameters β, σ, and α define the Crystal Ball function and are the values extracted from the fit to $\Delta\frac{q}{p_T}$; β and σ correspond to the mean and resolution of the core part of the distribution, while α represents the slope of the tail of the distribution. The fit parameters were determined separately for electrons and muons in bins of p_T. The smearing parameters are used to define the smearing in the Control Region in order

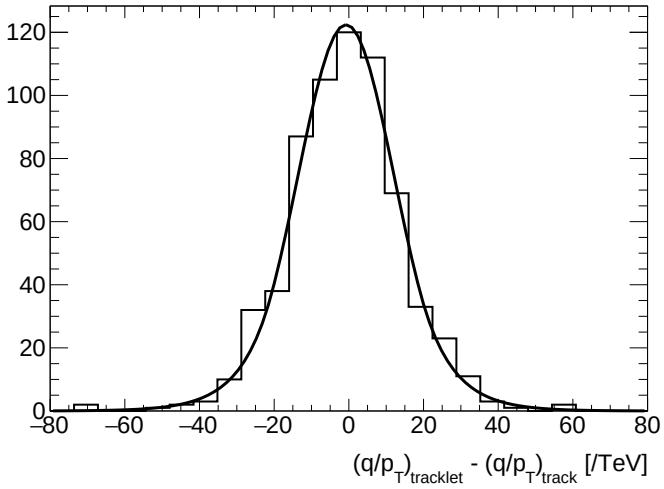

Figure 7.1: Example Fit of $\Delta\frac{q}{p_T} = \left|\frac{q}{p_T^{tracklet}}\right| - \left|\frac{q}{p_T^{full}}\right|$

to match the resolution of a tracklet, according to the following equation:

$$p_T^{\text{smeared}} = \left|\left(\frac{q}{p_T}\right)^{\text{original}} + \text{random}(f(z))\right|^{-1} \tag{7.4}$$

where random($f(z)$) is a random number from the smearing function distribution. The smearing function parameters were varied up and down by their uncertainties to determine the "envelope": the range of the effects of these uncertainties on the final lepton scatter background estimate.

The smearing function parameters, along with their uncertainties, can be found in Tables 7.1 and 7.2. It should be noted the units for these parameters are TeV; the conversion to GeV (or, rather, inverse GeV) is done immediately after applying random($f(z)$).

The effect of smearing the $\frac{q}{p_T}$ on the final p_T distribution can be considered

p_T GeV	β TeV^{-1}	σ TeV^{-1}	α
25 - 35	-0.20 ± 0.07	17.01 ± 1.42	1.86 ± 0.21
35 - 45	-0.15 ± 0.10	15.42 ± 1.07	1.82 ± 0.22
45 - 60	-0.13 ± 0.10	14.49 ± 0.74	1.66 ± 0.19
60 - 100	-0.21 ± 0.10	13.90 ± 0.43	1.54 ± 0.06
100 - 200	-0.21 ± 0.33	14.03 ± 1.16	1.64 ± 0.28

Table 7.1: Fit Parameters for **Electron** Smearing Function

from a purely mathematical perspective, and it can be shown (Appendix B) that for any smearing function which is symmetric about zero and positive definite over $\mathbb{R}$, the median of the smeared p_T distribution will be skewed towards lower values. Our smearing function is a double-sided Crystal Ball, which is symmetric about zero and positive definite over $\mathbb{R}$, and indeed this is precisely the behavior we see. Figures 7.2, 7.3, 7.4, and 7.5 show the effect of our smearing function on mono-energetic electron samples; we can clearly see the tendency is to shift them to lower p_T although there is a "fat tail" heading out to higher values.

The effects of the smearing can be seen by comparing the Control Regions with both smeared (Figure 7.7 for electrons, Figure 7.9 for muons) and unsmeared (Figures 7.6 and 7.8) lepton p_T; we see a general tendency to push p_T downwards, exactly as expected from the mono-energetic samples. Though it may be tempting to view these plots as the actual Backgrounds, neither has been multiplied by the Transfer

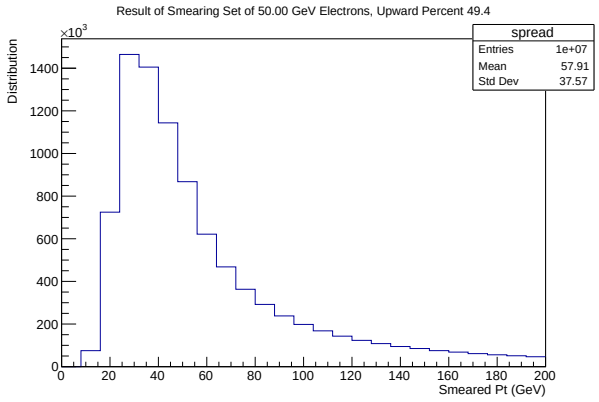

Figure 7.2: Smeared Distribution of 10 Million 50 GeV electrons

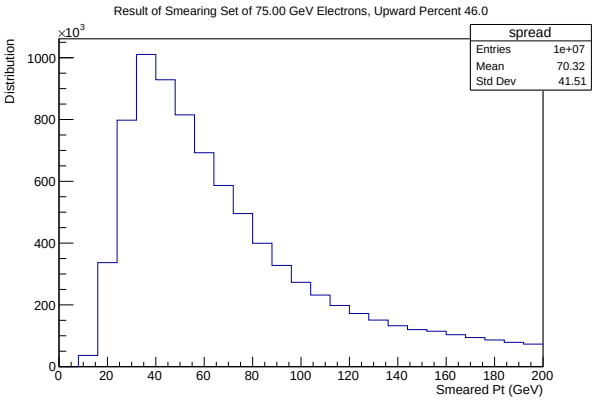

Figure 7.3: Smeared Distribution of 10 Million 75 GeV electrons

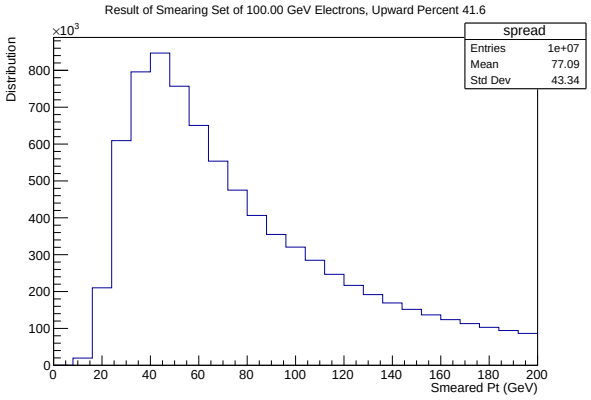

Figure 7.4: Smeared Distribution of 10 Million 100 GeV electrons

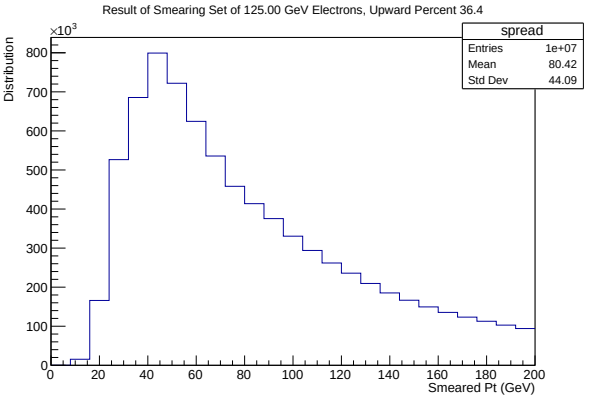

Figure 7.5: Smeared Distribution of 10 Million 125 GeV electrons

p_T GeV	β TeV^{-1}	σ TeV^{-1}	α
25 - 35	-0.25 ± 0.31	14.84 ± 1.21	1.72 ± 0.16
35 - 45	-0.19 ± 0.10	14.21 ± 0.73	1.66 ± 0.05
45 - 60	-0.13 ± 0.37	13.64 ± 1.08	1.62 ± 0.21
60 - 100	-0.28 ± 0.13	13.44 ± 0.41	1.68 ± 0.04
100 - 200	0.00 ± 0.36	13.21 ± 0.60	1.64 ± 0.17

Table 7.2: Fit Parameters for **Muon** Smearing Function

Factor, these plots are effectively what we would see if the Transfer Factor were precisely unity.

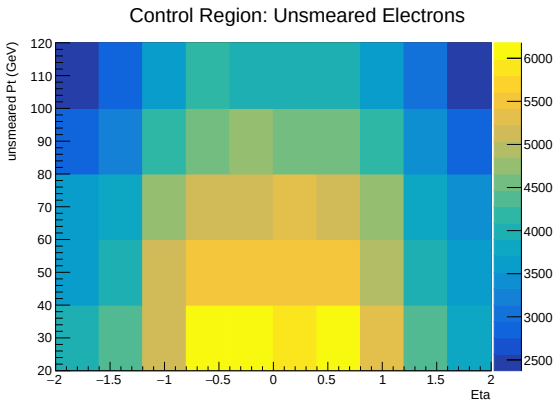

Figure 7.6: Control Region: Unsmeared Electrons

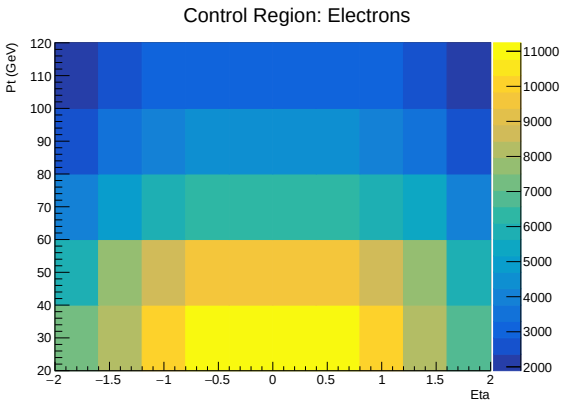

Figure 7.7: Control Region: Smeared Electrons

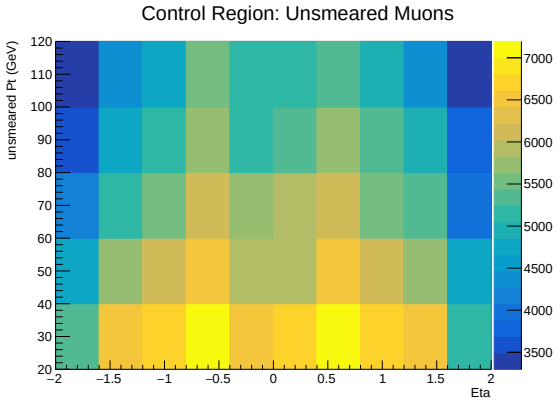

Figure 7.8: Control Region: Unsmeared Muons

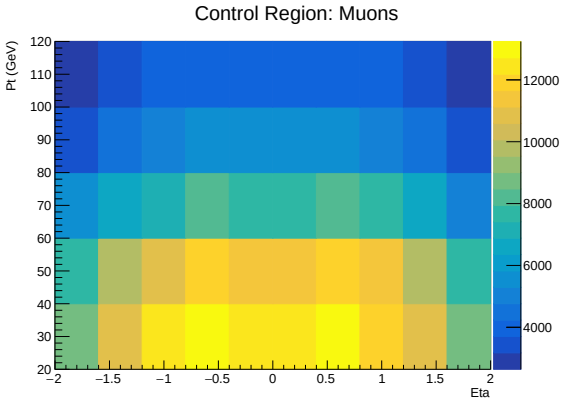

Figure 7.9: Control Region: Smeared Muons

7.3 Closure

In order to estimate the lepton (electron or muon) backgrounds in the Signal Region, we will multiply the number of events in the Control Region by the Transfer Factors derived in Chapter 6. The Transfer Factors should be process independent, an assumption which was tested by conducting a Closure Test on $Z \to \ell\ell$ and $W \to \ell\nu$ Monte Carlo samples, in which 1D proxy Transfer Factor Maps with the same p_T binning as the real ones were created from both samples and compared with each other. If these Transfer Factors are the same, then the background estimation strategy defined above will correctly estimate the $W \to \ell\nu$ background in the Monte Carlo; this will ensure that the background estimation strategy is correct, at least as far as all effects modelled in the MC are concerned.

To create the proxy Transfer Factor Maps from the W sample, we required our "numerator" to have a single tracklet truth-matched to an electron or muon with $\Delta R < 0.2$ between the tracklet and either a calorimeter cluster (for electrons) or MS track segment (for muons), along with a E_T^{miss} trigger. The "denominator" term required a fully reconstructed lepton, the same E_T^{miss} trigger and $\Delta R < 0.2$ requirement versus calorimeter clusters or MS track segments. The proxy map for the Z sample was constructed in exactly the same way as the real Transfer Factor Maps. The final comparison was done by dividing the maps produced by the W by their counterparts from the Z in order to determine the relative scale of any difference. Tables 7.3 and 7.4 summarize these criteria. In an ideal world, the ratio between them would be precisely 1, but alas, reality

is often disappointing. Figures 7.10 and 7.11 show the results of the Closure test.

Due to the nature of the decays, the lower p_T bins hold the majority of the events, hence the much more significant deviations in the high-p_T bins. The reason we do not consider the large deviations at high p_T to be a serious concern is because there are far fewer events in the high p_T bins for $W \to \ell\nu$ and so the ratio in these bins is naturally subject to large variations. We are ultimately concerned only with the deviation from unity in the p_T kinematic variable because that is the variable of interest for the entire analysis. This deviation is conservatively estimated as a flat 20% systematic uncertainty.

Electron (Denominator)	**Tracklet** (Numerator)
E_T^{miss} Trigger	E_T^{miss} Trigger
$\Delta R(electron, caloCluster) < 0.2$	$\Delta R(tracklet, caloCluster) < 0.2$
Signal Electron	**Tracklet truth-matched to electron**

Table 7.3: Closure Test Criteria for the $W \to e\nu$ MC Sample

Muon (Denominator)	**Tracklet** (Numerator)
E_T^{miss} Trigger	E_T^{miss} Trigger
$\Delta R(muon, msTrack) < 0.2$	$\Delta R(tracklet, msTrack) < 0.2$
Signal muon	**Tracklet truth-matched to muon**

Table 7.4: Closure Test Criteria for the $W \to \mu\nu$ MC Sample

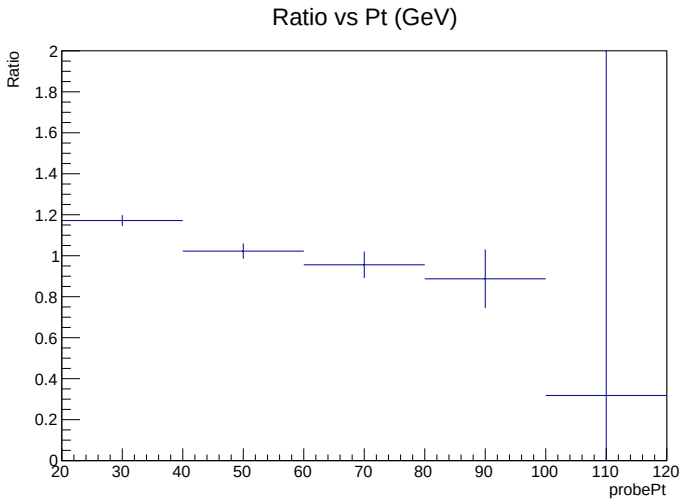

Figure 7.10: Electron Closure: ratio of the Transfer Factor as calculated by $W \to \ell\nu$ vs $Z \to \ell\ell$ in Monte Carlo

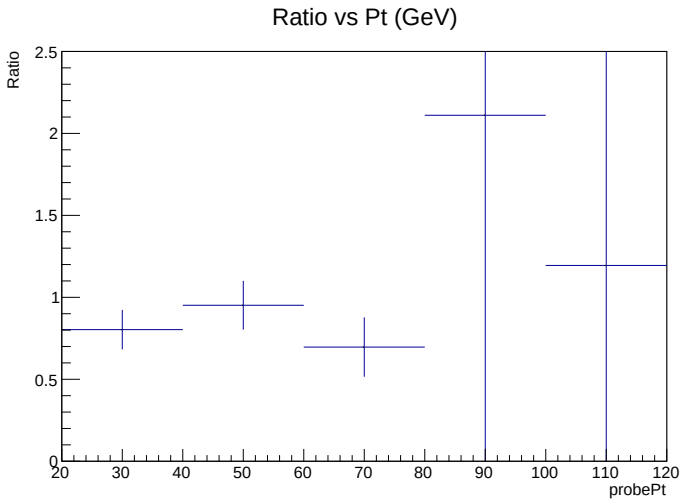

Figure 7.11: Muon Closure: ratio of the Transfer Factor as calculated by $W \to \ell\nu$ vs $Z \to \ell\ell$ in Monte Carlo

7.4 Systematic Uncertainties in the Background Estimation

The two primary systematic uncertainties in the background estimation encountered during the estimation of the lepton scatter background came from the Closure test and the Smearing Functions. The deviation from unity found in the Closure test is of $\mathcal{O}(20\%)$, so a flat 20% relative uncertainty was applied across the entire p_T range as the systematic uncertainty from non-closure.

The parameters used to control the smearing functions (β, σ, and α) were not determined to arbitrarily high precision. This uncertainty has an impact because a change in any of these parameters will shift the apparent p_T of the Control Region leptons and therefore systematically change the Transfer Factor values applied. This was treated via the "envelope" method, where separate weights were created for each extreme of each smearing parameter, for a total of seven weights in each ntuple: one for the nominal values of the parameters, one high value for each parameter, and one low value for each parameter. All seven weights were used to calculate the lepton scatter background in the same way, and within each bin of the smeared p_T the highest and lowest values were retained, in addition to the nominal value. The difference between the nominal value and the high (low) value is taken as the systematic up (down) uncertainty for each bin as seen in Tables 7.5 (electrons) and 7.8.

The systematic uncertainty from non-closure is combined in quadrature with the sys-

tematic up and down uncertainties separately, to produce the final asymmetric up and down systematic uncertainties in each bin of the smeared lepton p_T. All of this is done separately for electrons and muons, before being combined as the final stage of this lepton scatter characterization analysis.

7.5 Data-Driven Background Estimation via Single Lepton Control Region

With the Transfer Factor Maps in hand, a more general selector was run on the 2015 and 2016 data. The events in the Single Lepton Control Region, defined in Section 7.1, are multiplied by the Transfer Factor to determine the expected number of lepton scatter events within the Signal Region. We then smear the lepton p_T to get the final distribution representing the background estimate to the disappearing track signature.

The final thrust of this dissertation is the description of the number of lepton scatters as a function of the smeared lepton p_T, because p_T is likely to have the strongest discriminating power between signal and background. This is because low-momentum leptons are more prone to scattering away at a steep enough angle to produce the disappearing track signature than high-momentum leptons, whereas a chargino is more likely to traverse enough of the detector to produce the 4 Pixel Hits if it has high-momentum. The "epilogue" to this analysis looks at the number of signal charginos as a function of

tracklet transverse momentum to see if there is an obvious threshold which eliminates as many lepton scatters as possible without cutting into the chargino signal, and also to get a rough feel for the overall sensitivity of the Run 2 dataset.

Before calculating the background, it's helpful to have a discussion of the statistical errors that arise from the limited sample sizes in the Control Region and Tag and Probe analysis. There are two components to the statistical uncertainty in this analysis: the uncertainty on the Transfer Factor, resulting from limited statistics in the fit of the Z peak, and the uncertainty on the number of Control Region events. Using standard error propagation for a function $f(x_1, x_2) = x_1 * x_2$, we find the error (σ_B) on the number of background events (within each bin) is given by:

$$\frac{\sigma_B}{B} = \sqrt{\left(\frac{\sigma_{N_{CR}}}{N_{CR}}\right)^2 + \left(\frac{\sigma_{TF}}{TF}\right)^2}, \tag{7.5}$$

where we have N_{CR} as the raw number of Control Region events, TF as the Transfer Factor value, and the two σ terms as their respective uncertainties. The uncertainty on the Transfer Factor comes from the limited statistics of the fit and is calculated as:

$$\sigma_{TF} = TF * \sqrt{\left(\frac{1}{N}\right) + \left(\frac{1}{D}\right)}, \tag{7.6}$$

where N is the numerator term and D the denominator term used in calculating the Transfer Factor itself. The uncertainty on the number of events in the Control Region is simply:

$$\sigma_{N_{CR}} = \sqrt{N_{CR}}. \tag{7.7}$$

The absolute uncertainty on the number of background events is therefore given by:

$$\sigma_B = B\sqrt{\left(\frac{1}{N_{CR}}\right) + \left(\frac{\sigma_{TF}}{TF}\right)^2} \tag{7.8}$$

Within each bin of the smeared lepton p_T, the statistical uncertainty on the number of scatters is determined by adding the statistical uncertainties from each η bin in quadrature.

Multiplying the numbers in the Control Region by the appropriate Transfer Factor, Tables 7.5 (electrons) and 7.8 (muons) show the nominal number of scatters in each bin for their respective particles as well as the systematic uncertainties from non-closure and from the uncertainty in the smearing function parameters separately; the 20% non-closure uncertainty is by far the dominant systematic uncertainty for both lepton flavors. Tables 7.6 (electrons) and 7.9 (muons) show the nominal number of background events in each bin, along with the maximum and minimum variation as determined by adding or subtracting the total systematic uncertainty from the nominal value, with the statistical uncertainties resulting from the limited statistics of the Control Region and the tag-and-probe sample shown in the final column.

The grand totals are shown in Tables 7.7 and 7.10. The numbers in Table 7.11 are obtained by adding the nominal values for electrons and muons linearly, and for the Systematic Up (Down) integral by taking the difference between the electron Systematic Up (Down) and Nominal integrals and adding that in quadrature with the equivalent difference for muons to obtain the "Systematic Up (Down) Delta", which is then linearly

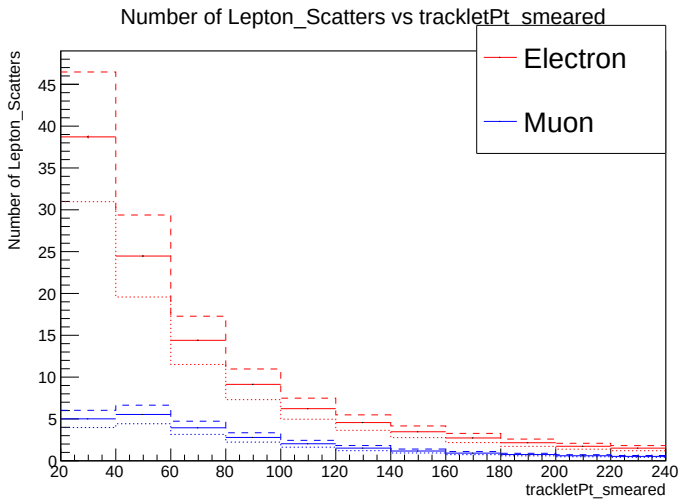

Figure 7.12: Estimated Lepton Scatter Background: solid lines are the nominal estimate, dashed (dotted) lines show the nominal plus (minus) the upward (downward) systematic uncertainty

added to (subtracted from) the sum of the nominal integrals.

Finally, Figure 7.12 plots the p_T dependence of the lepton-scatter background (muons and electrons), showing the one-sigma systematic range. In Figure 7.12 the solid lines are the nominal numbers, while the dashed line is the uppermost systematic and the dotted line is the lowermost systematic.

Smeared p_T (GeV)	**Nominal**	Non-Closure Sys	Smear Sys Up	Smear Sys Down
20 - 40	38.72	7.74	0.47	0.28
40 - 60	24.47	4.89	0.35	0.14
60 - 80	14.40	2.88	0.15	0.18
80 - 100	9.13	1.83	0.21	0.05
100 - 120	6.23	1.25	0.16	0.17
120 - 140	4.57	0.91	0.11	0.16
140 - 160	3.47	0.69	0.05	0.12
160 - 180	2.73	0.55	0.02	0.09
180 - 200	2.16	0.43	0.07	0.03
200 - 220	1.73	0.35	0.08	0.01
220 - 240	1.51	0.30	0.00	0.06
240+	16.43	3.29	0.24	0.56

Table 7.5: Electron Systematic Uncertainty Comparison

Smeared p_T (GeV)	**Nominal**	**Full Sys Up**	**Full Sys Down**	**Stat Uncertainty**
20 - 40	38.72	7.76	7.75	0.438
40 - 60	24.47	4.91	4.90	0.310
60 - 80	14.40	2.88	2.89	0.740
80 - 100	9.13	1.84	1.83	1.73
100 - 120	6.23	1.26	1.26	1.18
120 - 140	4.57	0.92	0.92	0.847
140 - 160	3.47	0.70	0.70	0.644

Table 7.6: Electron Scatter Background Summary

Smeared p_T (GeV)	**Nominal**	Sys Up Uncertainty	Sys Down Uncertainty
60+	62.35	12.53	12.57
80+	47.95	9.65	9.69
100+	38.82	7.81	7.86
120+	32.59	6.73	6.60

Table 7.7: Electron Scatter Background Cumulative Above Particular p_T Thresholds with Full Systematic Uncertainties

Smeared p_T (GeV)	**Nominal**	Non-Closure Sys	Smear Sys Up	Smear Sys Down
20 - 40	5.01	1.00	0.19	0.28
40 - 60	5.54	1.11	0.08	0.07
60 - 80	3.94	0.79	0.004	0.03
80 - 100	2.79	0.56	0.03	0.04
100 - 120	2.03	0.41	0.02	0.06
120 - 140	1.51	0.30	0.05	0.04
140 - 160	1.17	0.23	0.03	0.03
160 - 180	0.92	0.18	0.03	0.01
180 - 200	0.74	0.15	0.02	0.03
200 - 220	0.60	0.12	0.03	0.00
220 - 240	0.53	0.11	0.004	0.02
240+	5.72	1.14	0.18	0.11

Table 7.8: Muon Systematic Uncertainty Comparison

Smeared p_T (GeV)	Nominal	Full Sys Up	Full Sys Down	Stat Uncertainty
20 - 40	5.01	1.02	1.04	0.242
40 - 60	5.54	1.11	1.11	0.295
60 - 80	3.94	0.79	0.79	0.759
80 - 100	2.79	0.56	0.56	0.711
100 - 120	2.03	0.41	0.41	0.522
120 - 140	1.51	0.31	0.31	0.386
140 - 160	1.17	0.24	0.23	0.296

Table 7.9: Muon Scatter Background Summary

Smeared p_T (GeV)	**Nominal**	**Sys Up Uncertainty**	**Sys Down Uncertainty**
60+	19.95	4.02	4.01
80+	16.00	3.23	3.22
100+	13.21	2.68	2.66
120+	11.18	2.27	2.25

Table 7.10: Muon Scatter Background Cumulative Above Particular p_T Thresholds with Full Systematic Uncertainties

Smeared p_T (GeV)	**Nominal**	**Systematic Up**	**Systematic Down**
60+	82.30	13.16	13.19
80+	63.95	10.18	10.21
100+	52.03	8.25	8.30
120+	43.77	6.93	6.97

Table 7.11: Combined Lepton Scatter Background: The Nominal Background the Systematic Up and Down Variations

7.6 Preliminary Comparison with Signal Monte Carlo

In order to give the background described in Figure 7.12 and Table 7.11 a more salient meaning, we compared this result with an AMSB model of a wino-like 500.2 GeV $\tilde{\chi}_1^{\pm}$ chargino with a variety of lifetimes from 0.4 ns up to 4.0 ns, spanning the range in which it is plausible for a chargino to both penetrate the Pixel Detector and decay prior to reaching the SCT. Figures C.3 shows the number of events vs tracklet p_T within the Signal Region scaled to 139 fb^{-1} of integrated luminosity, for a range of different chargino lifetimes.

This plot show a 500.2 GeV mass point with several possible lifetimes, the default (4.0 ns) lifetime along with the 0.4, 0.6, 1.0, 2.0, and 3.0 nanosecond lifetimes. Not all of the lifetimes shown on the plot were produced directly with Monte Carlo, all but the highest were produced by reweighting after the sample had already been produced. Reweighting is only done downwards according to the following equation:

$$w(\tau_{\tilde{\chi}^{\pm}}) = \prod_{i}^{n_{\tilde{\chi}^{\pm}}} \frac{\tau_0}{\tau_{\tilde{\chi}^{\pm}}} \exp\left\{\left[-t_i\left(\frac{1}{\tau_{\tilde{\chi}^{\pm}}} - \frac{1}{\tau_0}\right)\right]\right\}, \tag{7.9}$$

where $n_{\tilde{\chi}^{\pm}}$, τ_0, and t_i are the number of charginos in the event, the chargino mean lifetime, and the proper lifetime of the i^{th} chargino, respectively.

Comparing raw numbers for the full 139 fb^{-1} Run 2 dataset, as shown in Table 7.12 we see the 500.2 GeV mass point is quite visible for a range of lifetimes.

We can estimate the sensitivity using a figure of merit, with results for a

p_T [GeV]	$\tau = 0.4\,\text{ns}$	$\tau = 0.6\,\text{ns}$	$\tau = 1.0\,\text{ns}$	$\tau = 2.0\,\text{ns}$	$\tau = 3.0\,\text{ns}$	$\tau = 4.0\,\text{ns}$	Scaled Background
20	94.4	117	125	106	87.4	73.7	604
40	94.0	116	124	105	86.4	72.8	435
60	92.4	114	121	103	84.7	71.3	318
80	90.7	111	118	98.5	80.7	67.8	247
100	85.4	104	110	91.4	74.7	62.7	201
120	82.7	99.6	103	84.6	68.6	57.3	169
140	71.7	86.9	90.4	74.7	60.9	51.0	146
160	64.5	77.6	80.4	66.8	54.6	45.8	128
180	60.9	72.4	74.4	61.5	50.2	42.0	114
200	56.4	67.2	69.0	56.4	45.6	37.9	102
220	54.5	64.4	65.6	53.0	42.6	35.4	93.4
240	52.3	60.9	60.8	48.2	38.7	32.1	85.5

Table 7.12: Expected Signals for different lifetimes of a 500.2 GeV mass wino-like chargino with $139\,\text{fb}^{-1}$ of Integrated Luminosity

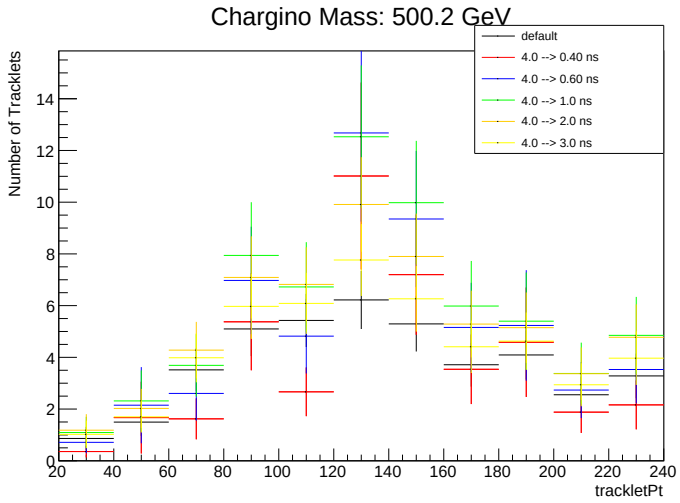

Figure 7.13: Tracklet p_T distribution for a chargino with 500.2 GeV and 4 ns base lifetime, reweighted to lifetimes between 0.4, 1.0, and 3.0 ns with 139 fb^{-1} of integrated luminosity

500.2 GeV chargino in Table 7.13:

$$Z = \sqrt{2((s+b)\ln(1+\frac{s}{b})) - s}, \tag{7.10}$$

where s is the signal and b is the background. This equation comes from Cowan [56], which describes in general how to establish the sensitivity of counting experiment with a background constraint.

Focusing on the one nanosecond lifetime and extending in mass, we get the sensitivities in Table 7.14.

A few other mass points were tested as well. Those results are reported in Appendix C. The general pattern, for all of these mass points and lifetimes, is clear: chargino tracklets are much more common above about 80 GeV than they are below it, with most tracklets occurring between 100 and 200 GeV.

p_T [GeV]	$\tau = 0.4\,\text{ns}$	$\tau = 0.6\,\text{ns}$	$\tau = 1.0\,\text{ns}$	$\tau = 2.0\,\text{ns}$	$\tau = 3.0\,\text{ns}$	$\tau = 4.0\,\text{ns}$
20	3.7	4.6	4.9	4.2	3.5	2.9
40	4.4	5.3	5.7	4.8	4.0	3.4
60	5.0	6.1	6.4	5.5	4.6	3.9
80	5.5	6.6	7.0	5.9	4.9	4.1
100	5.7	6.8	7.2	6.0	5.0	4.2
120	5.9	7.0	7.3	6.1	5.0	4.2
140	5.5	6.6	6.9	5.7	4.7	4.0
160	5.3	6.3	6.5	5.5	4.5	3.8
180	5.3	6.2	6.4	5.3	4.4	3.7
200	5.1	6.1	6.2	5.1	4.2	3.5
220	5.2	6.1	6.2	5.1	4.1	3.5
240	5.2	6.0	6.0	4.8	3.9	3.3

Table 7.13: Estimated sensitivities for different lifetimes of a 500.2 GeV mass wino-like chargino with $139\,\text{fb}^{-1}$ assuming the lepton scatter background is dominant

p_T [GeV]	$m = 500.2\,\text{GeV}$	$m = 599.9\,\text{GeV}$	$m = 700.1\,\text{GeV}$
20	4.9	2.3	1.2
40	5.7	2.7	1.4
60	6.4	3.1	1.6
80	7.0	3.3	1.8
100	7.2	3.4	1.9
120	7.3	3.4	1.9
140	6.9	3.4	1.8
160	6.5	3.4	1.8
180	6.4	3.3	1.8
200	6.2	3.2	1.8
220	6.2	3.2	1.8
240	6.0	3.1	1.7

Table 7.14: Estimated sensitivities for different wino masses with 1.0 ns lifetime

The overall shape comparison between the lepton scatter background in Figure 7.12 vs that of the signal charginos favors requiring tracklet p_T greater than 80 or 100 GeV to best reduce the lepton scatter background without reducing the signal too much. The exact value of the p_T cut should be determined by optimization of an appropriate statistical figure of merit once the full background estimate (including combinatorial fakes and hadronic scatters) is available.

Chapter 8

Conclusion

The lepton scatter background to the disappearing track signature in the ATLAS Detector was characterized using about $36\,\text{fb}^{-1}$ of integrated luminosity with 13 TeV center-of-mass energy proton-proton collisions at the LHC. It was found to be electron-dominated at low-p_T but balanced between electrons and muons at high-p_T. This strongly suggests the tracklet p_T threshold used for the disappearing track analyses should be set to at least 80 GeV to most effectively reduce this background. Preliminary comparison with a representative AMSB model which produces the disappearing track signature shows the lepton scatter background above 80 GeV to be of similar scale to the signal. For a wino-like scenario, under the assumption that the lepton scatter background is dominant, the Run 2 sensitivity approaches a mass scale of 650 GeV.

8.1 Future Prospects

In order to perform the disappearing track analysis and search for the presence of AMSB-like supersymmetry, the important next step will be determining the combinatorial fake background. This is the background produced by unrelated Pixel Hits, primarily arising from overlaid minimum bias tracks. There is also the hadronic background due to mesons scattering in the detector. The combinatorial fake and hadronic scatter background are both believed to be smaller than the lepton scatter background estimated in this analysis. This analysis can be advanced further by incorporating the full Run 2 data set. The Transfer Factor, and by extension the background estimate, is statistics-limited in the region of interest ($p_T > 80\,\text{GeV}$), increasing the available data from 36 to $139\,\text{fb}^{-1}$ should allow for a significant reduction in the uncertainty in this regime.

Bibliography

[1] S. Abachi et al. "Observation of the top quark". In: *Phys. Rev. Lett.* 74 (1995), pp. 2632–2637. DOI: 10.1103/PhysRevLett.74.2632. arXiv: hep-ex/9503003 [hep-ex].

[2] S. Agostinelli et al. "Geant4—a simulation toolkit". In: *Nuclear Instruments and Methods in Physics Research Section A: Accelerators, Spectrometers, Detectors and Associated Equipment* 506.3 (2003), pp. 250–303. ISSN: 0168-9002. DOI: https://doi.org/10.1016/S0168-9002(03)01368-8. URL: http://www.sciencedirect.com/science/article/pii/S0168900203013688.

[3] Y. Aharonov and D. Bohm. "Significance of Electromagnetic Potentials in the Quantum Theory". In: *Phys. Rev.* 115 (3 Aug. 1959), pp. 485–491. DOI: 10.1103/PhysRev.115.485. URL: https://link.aps.org/doi/10.1103/PhysRev.115.485.

[4] M. Aliev et al. "HATHOR – HAdronic Top and Heavy quarks crOss section calculatoR". In: *Comput. Phys. Commun.* 182 (2011), pp. 1034–1046. DOI: 10.1016/j.cpc.2010.12.040. arXiv: 1007.1327 [hep-ph].

[5] Simone Alioli et al. "A general framework for implementing NLO calculations in shower Monte Carlo programs: the POWHEG BOX". In: *JHEP* 06 (2010), p. 043. DOI: 10.1007/JHEP06(2010)043. arXiv: 1002.2581 [hep-ph].

[6] Simone Alioli et al. "NLO single-top production matched with shower in POWHEG: s- and t-channel contributions". In: *JHEP* 09 (2009). [Erratum: JHEP02,011(2010)], p. 111. DOI: 10.1007/JHEP02(2010)011,10.1088/1126-6708/2009/09/111. arXiv: 0907.4076 [hep-ph].

[7] Simone Alioli et al. "NLO vector-boson production matched with shower in POWHEG". In: *JHEP* 07 (2008), p. 060. DOI: 10.1088/1126-6708/2008/07/060. arXiv: 0805.4802 [hep-ph].

[8] J. Alwall et al. "The automated computation of tree-level and next-to-leading order differential cross sections, and their matching to parton shower simulations". In: *JHEP* 07 (2014), p. 079. DOI: 10.1007/JHEP07(2014)079. arXiv: 1405.0301 [hep-ph].

[9] Johan Alwall et al. "A Standard format for Les Houches event files". In: *Comput. Phys. Commun.* 176 (2007), pp. 300–304. DOI: 10.1016/j.cpc.2006.11.010. arXiv: hep-ph/0609017 [hep-ph].

[10] Charalampos Anastasiou et al. "High precision QCD at hadron colliders: Electroweak gauge boson rapidity distributions at NNLO". In: *Phys. Rev. D* 69 (2004), p. 094008. DOI: 10.1103/PhysRevD.69.094008. arXiv: hep-ph/0312266.

[11] Heinz Andernach and Fritz Zwicky. *English and Spanish Translation of Zwicky's (1933) The Redshift of Extragalactic Nebulae*. 2017. arXiv: 1711.01693 [astro-ph.IM].

[12] Carl D. Anderson. "The Apparent Existence of Easily Deflectable Positives". In: *Science* Vol. 76, Issue 1967, pp. 238-239 (1932). DOI: 10.1126/science.76.1967.238. URL: https://science.sciencemag.org/content/76/1967/238.

[13] Bo Andersson et al. "Parton fragmentation and string dynamics". In: *Phys. Rept.* 97 (1983), pp. 31–145. DOI: 10.1016/0370-1573(83)90080-7.

[14] Pierre Artoisenet et al. "Automatic spin-entangled decays of heavy resonances in Monte Carlo simulations". In: *JHEP* 03 (2013), p. 015. DOI: 10.1007/JHEP03(2013)015. arXiv: 1212.3460 [hep-ph].

[15] *ATLAS inner detector: Technical Design Report, 1*. Technical Design Report ATLAS. Geneva: CERN, 1997. URL: https://cds.cern.ch/record/331063.

[16] *ATLAS liquid-argon calorimeter: Technical Design Report*. Technical Design Report ATLAS. Geneva: CERN, 1996. URL: https://cds.cern.ch/record/331061.

[17] *ATLAS Run 1 Pythia8 tunes*. Tech. rep. ATL-PHYS-PUB-2014-021. Geneva: CERN, Nov. 2014. URL: https://cds.cern.ch/record/1966419.

[18] ATLASPMG. "ttV NLO cross section". In: (2017). URL: https://twiki.cern.ch/twiki/bin/view/AtlasProtected/CrossSectionNLOttV.

[19] Richard D. Ball et al. "Parton distributions with LHC data". In: *Nucl. Phys. B* 867 (2013), pp. 244–289. DOI: 10.1016/j.nuclphysb.2012.10.003. arXiv: 1207.1303 [hep-ph].

[20] Peter Bärnreuther, Michal Czakon, and Alexander Mitov. "Percent-Level-Precision Physics at the Tevatron: Next-to-Next-to-Leading Order QCD Corrections to $q\bar{q} \to t\bar{t} + X$". In: *Phys. Rev. Lett.* 109 (2012), p. 132001. DOI: 10.1103/PhysRevLett.109.132001. arXiv: 1204.5201 [hep-ph].

[21] Johannes Bellm et al. "Herwig 7.0/Herwig++ 3.0 release note". In: *Eur. Phys. J. C* 76.4 (2016), p. 196. DOI: 10.1140/epjc/s10052-016-4018-8. arXiv: 1512.01178 [hep-ph].

[22] Johannes Bellm et al. "Herwig 7.1 Release Note". In: (). arXiv: 1705.06919 [hep-ph].

[23] M. Beneke et al. "Hadronic top-quark pair production with NNLL threshold resummation". In: *Nucl. Phys. B* 855 (2012), pp. 695–741. DOI: 10.1016/j.nuclphysb.2011.10.021. arXiv: 1109.1536 [hep-ph].

[24] G. R. Blumenthal, H. Pagels, and J. R. Primack. "Galaxy formation by dissipationless particles heavier than neutrinos". In: 299.5878 (Sept. 1982), pp. 37–38. DOI: 10.1038/299037a0.

[25] E. Boos et al. "Generic user process interface for event generators". In: *Physics at TeV colliders. Proceedings, Euro Summer School, Les Houches, France, May*

21-June 1, 2001. 2001. arXiv: hep-ph/0109068 [hep-ph]. URL: http://lss.fnal.gov/archive/preprint/fermilab-conf-01-496-t.shtml.

[26] Enrico Bothmann et al. "Event Generation with Sherpa 2.2". In: (2019). arXiv: 1905.09127 [hep-ph].

[27] Enrico Bothmann, Marek Schönherr, and Steffen Schumann. "Reweighting QCD matrix-element and parton-shower calculations". In: *Eur. Phys. J. C* 76.11 (2016), p. 590. DOI: 10.1140/epjc/s10052-016-4430-0. arXiv: 1606.08753 [hep-ph].

[28] Michiel Botje et al. "The PDF4LHC Working Group Interim Recommendations". In: (2011). arXiv: 1101.0538 [hep-ph].

[29] J. Butterworth et al. "Les Houches 2013: Physics at TeV Colliders: Standard Model Working Group Report". In: (2014). arXiv: 1405.1067 [hep-ph].

[30] Jon Butterworth et al. "PDF4LHC recommendations for LHC Run II". In: *J. Phys. G* 43 (2016), p. 023001. DOI: 10.1088/0954-3899/43/2/023001. arXiv: 1510.03865 [hep-ph].

[31] Matteo Cacciari. "FastJet: A Code for fast k_t clustering, and more". In: *Deep inelastic scattering. Proceedings, 14th International Workshop, DIS 2006, Tsukuba, Japan, April 20-24, 2006*. [,125(2006)]. 2006, pp. 487–490. arXiv: hep-ph/0607071 [hep-ph].

[32] Matteo Cacciari, Gavin P. Salam, and Gregory Soyez. "The anti-k_t jet clustering algorithm". In: *JHEP* 04 (2008), p. 063. DOI: 10.1088/1126-6708/2008/04/063. arXiv: 0802.1189 [hep-ph].

[33] Matteo Cacciari et al. "Top-pair production at hadron colliders with next-to-next-to-leading logarithmic soft-gluon resummation". In: *Phys. Lett. B* 710 (2012), pp. 612–622. DOI: 10.1016/j.physletb.2012.03.013. arXiv: 1111.5869 [hep-ph].

[34] Fabio Cascioli, Philipp Maierhofer, and Stefano Pozzorini. "Scattering Amplitudes with Open Loops". In: *Phys. Rev. Lett.* 108 (2012), p. 111601. DOI: 10.1103/PhysRevLett.108.111601. arXiv: 1111.5206 [hep-ph].

[35] S. Catani et al. "QCD Matrix Elements + Parton Showers". In: *JHEP* 11 (2001), p. 063. DOI: 10.1088/1126-6708/2001/11/063. arXiv: hep-ph/0109231.

[36] ATLAS Collaboration. "A neural network clustering algorithm for the ATLAS silicon pixel detector". In: *JINST* 9 (2014), P09009. DOI: 10.1088/1748-0221/9/09/P09009. arXiv: 1406.7690 [hep-ex].

[37] ATLAS Collaboration. *Athena*. Version 22.0.1. Apr. 2019. DOI: 10.5281/zenodo.2641997. URL: https://doi.org/10.5281/zenodo.2641997.

[38] ATLAS Collaboration. "ATLAS pixel detector electronics and sensors". In: *Journal of Instrumentation* 3.07 (July 2008), P07007–P07007. DOI: 10.1088/1748-0221/3/07/p07007. URL: https://doi.org/10.1088%2F1748-0221%2F3%2F07%2Fp07007.

[39] ATLAS Collaboration. "Commissioning of the ATLAS Muon Spectrometer with Cosmic Rays". In: *Eur. Phys. J.* C70 (2010), pp. 875–916. DOI: 10.1140/epjc/s10052-010-1415-2. arXiv: 1006.4384 [physics.ins-det].

[40] ATLAS Collaboration. "Jet energy scale measurements and their systematic uncertainties in proton-proton collisions at $\sqrt{s}$ = 13 TeV with the ATLAS detector". In: *Phys. Rev.* D96.7 (2017), p. 072002. DOI: 10.1103/PhysRevD.96.072002. arXiv: 1703.09665 [hep-ex].

[41] ATLAS Collaboration. "Jet reconstruction and performance using particle flow with the ATLAS Detector". In: *Eur. Phys. J.* C77.7 (2017), p. 466. DOI: 10.1140/epjc/s10052-017-5031-2. arXiv: 1703.10485 [hep-ex].

[42] ATLAS Collaboration. "Measurement of the Z/γ^* boson transverse momentum distribution in pp collisions at $\sqrt{s} = 7$ TeV with the ATLAS detector". In: *JHEP* 09 (2014), p. 145. DOI: 10.1007/JHEP09(2014)145. arXiv: 1406.3660 [hep-ex].

[43] ATLAS Collaboration. "Muon reconstruction performance of the ATLAS detector in proton–proton collision data at $\sqrt{s}$ =13 TeV". In: *Eur. Phys. J.* C76.5 (2016), p. 292. DOI: 10.1140/epjc/s10052-016-4120-y. arXiv: 1603.05598 [hep-ex].

[44] ATLAS Collaboration. "Observation of a new particle in the search for the Standard Model Higgs boson with the ATLAS detector at the LHC". In: *Phys. Lett.* B716 (2012), pp. 1–29. DOI: 10.1016/j.physletb.2012.08.020. arXiv: 1207.7214 [hep-ex].

[45] ATLAS Collaboration. "Performance of missing transverse momentum reconstruction with the ATLAS detector using proton-proton collisions at $\sqrt{s}$ = 13

TeV". In: *Eur. Phys. J.* C78.11 (2018), p. 903. DOI: 10.1140/epjc/s10052-018-6288-9. arXiv: 1802.08168 [hep-ex].

[46] ATLAS Collaboration. "Performance of the ATLAS Track Reconstruction Algorithms in Dense Environments in LHC Run 2". In: *Eur. Phys. J.* C77.10 (2017), p. 673. DOI: 10.1140/epjc/s10052-017-5225-7. arXiv: 1704.07983 [hep-ex].

[47] ATLAS Collaboration. "Production and Integration of the ATLAS Insertable B-Layer". In: *JINST* 13.05 (2018), T05008. DOI: 10.1088/1748-0221/13/05/T05008. arXiv: 1803.00844 [physics.ins-det].

[48] ATLAS Collaboration. "The ATLAS Experiment at the CERN Large Hadron Collider". In: *Journal of Instrumentation* 3.08 (Aug. 2008), S08003–S08003. DOI: 10.1088/1748-0221/3/08/s08003. URL: https://doi.org/10.1088%2F1748-0221%2F3%2F08%2Fs08003.

[49] ATLAS Collaboration. "The ATLAS Insertable B-Layer project". In: *Journal of Instrumentation* 9.02 (Feb. 2014), pp. C02018–C02018. DOI: 10.1088/1748-0221/9/02/c02018. URL: https://doi.org/10.1088%2F1748-0221%2F9%2F02%2Fc02018.

[50] ATLAS Collaboration. "The ATLAS SemiConductor Tracker operation and performance". In: *Journal of Instrumentation* 7.04 (Apr. 2012), pp. C04001–C04001. DOI: 10.1088/1748-0221/7/04/c04001. URL: https://doi.org/10.1088%2F1748-0221%2F7%2F04%2Fc04001.

[51] ATLAS Collaboration. "The ATLAS Simulation Infrastructure". In: *Eur. Phys. J.* C70 (2010), pp. 823–874. DOI: 10.1140/epjc/s10052-010-1429-9. arXiv: 1005.4568 [physics.ins-det].

[52] ATLAS Collaboration. "The ATLAS Transition Radiation Tracker (TRT) proportional drift tube: design and performance". In: *Journal of Instrumentation* 3.02 (Feb. 2008), P02013–P02013. DOI: 10.1088/1748-0221/3/02/p02013. URL: https://doi.org/10.1088%2F1748-0221%2F3%2F02%2Fp02013.

[53] ATLAS Collaboration. "The upgraded Pixel detector and the commissioning of the Inner Detector tracking of the ATLAS experiment for Run-2 at the Large Hadron Collider". In: *PoS* EPS-HEP2015 (2015), p. 261. arXiv: 1608.07850 [physics.ins-det].

[54] ATLAS Collaboration. "Topological cell clustering in the ATLAS calorimeters and its performance in LHC Run 1". In: *Eur. Phys. J.* C77 (2017), p. 490. DOI: 10.1140/epjc/s10052-017-5004-5. arXiv: 1603.02934 [hep-ex].

[55] CMS Collaboration. "Observation of a New Boson at a Mass of 125 GeV with the CMS Experiment at the LHC". In: *Phys. Lett.* B716 (2012), pp. 30–61. DOI: 10.1016/j.physletb.2012.08.021. arXiv: 1207.7235 [hep-ex].

[56] G. Cowan. "Discovery sensitivity for a counting experiment with background uncertainty". In: (2012). URL: https://www.pp.rhul.ac.uk/~cowan/stat/notes/medsigNote.pdf.

[57] Michal Czakon, Paul Fiedler, and Alexander Mitov. "Total Top-Quark Pair-Production Cross Section at Hadron Colliders Through $O(\alpha_S^4)$". In: *Phys. Rev. Lett.* 110 (2013), p. 252004. DOI: 10.1103/PhysRevLett.110.252004. arXiv: 1303.6254 [hep-ph].

[58] Michal Czakon and Alexander Mitov. "NNLO corrections to top pair production at hadron colliders: the quark-gluon reaction". In: *JHEP* 01 (2013), p. 080. DOI: 10.1007/JHEP01(2013)080. arXiv: 1210.6832 [hep-ph].

[59] Michal Czakon and Alexander Mitov. "NNLO corrections to top-pair production at hadron colliders: the all-fermionic scattering channels". In: *JHEP* 12 (2012), p. 054. DOI: 10.1007/JHEP12(2012)054. arXiv: 1207.0236 [hep-ph].

[60] Michal Czakon and Alexander Mitov. "Top++: A program for the calculation of the top-pair cross-section at hadron colliders". In: *Comput. Phys. Commun.* 185 (2014), p. 2930. DOI: 10.1016/j.cpc.2014.06.021. arXiv: 1112.5675 [hep-ph].

[61] D. J. Lange. "The EvtGen particle decay simulation package". In: *Nucl. Instrum. Meth. A* 462 (2001), p. 152. DOI: 10.1016/S0168-9002(01)00089-4.

[62] N. Davidson, T. Przedzinski, and Z. Was. "PHOTOS interface in C++: Technical and physics documentation". In: *Comput. Phys. Commun.* 199 (2016), pp. 86–101. DOI: 10.1016/j.cpc.2015.09.013. arXiv: 1011.0937 [hep-ph].

[63] Ansgar Denner, Stefan Dittmaier, and Lars Hofer. "Collier: A fortran-based complex one-loop library in extended regularizations". In: *Comput. Phys. Commun.*

212 (2017), pp. 220–238. DOI: 10.1016/j.cpc.2016.10.013. arXiv: 1604.06792 [hep-ph].

[64] Duane A. Dicus and Vishnu S. Mathur. "Upper Bounds on the Values of Masses in Unified Gauge Theories". In: *Phys. Rev. D* 7 (10 May 1973), pp. 3111–3114. DOI: 10.1103/PhysRevD.7.3111. URL: https://link.aps.org/doi/10.1103/PhysRevD.7.3111.

[65] P. A. M. Dirac. "The Quantum Theory of the Electron". In: *Proceedings of the Royal Society of London Series A* 117.778 (Feb. 1928), pp. 610–624. DOI: 10.1098/rspa.1928.0023.

[66] Sayipjamal Dulat et al. "New parton distribution functions from a global analysis of quantum chromodynamics". In: *Phys. Rev. D* 93.3 (2016), p. 033006. DOI: 10.1103/PhysRevD.93.033006. arXiv: 1506.07443 [hep-ph].

[67] Albert Einstein. "Kosmologische Betrachtungen zur allgemeinen Relativitätstheorie". In: *Sitzungsberichte der Königlich Preußischen Akademie der Wissenschaften (Berlin* (Jan. 1917), pp. 142–152.

[68] *Electron efficiency measurements with the ATLAS detector using the 2015 LHC proton-proton collision data.* Tech. rep. ATLAS-CONF-2016-024. Geneva: CERN, June 2016. URL: https://cds.cern.ch/record/2157687.

[69] *Electron identification measurements in ATLAS using $\sqrt{s}$ = 13 TeV data with 50 ns bunch spacing.* Tech. rep. ATL-PHYS-PUB-2015-041. Geneva: CERN, Sept. 2015. URL: https://cds.cern.ch/record/2048202.

[70] F. Englert and R. Brout. "Broken Symmetry and the Mass of Gauge Vector Mesons". In: *Phys. Rev. Lett.* 13 (9 Aug. 1964), pp. 321–323. DOI: 10.1103/PhysRevLett.13.321. URL: https://link.aps.org/doi/10.1103/PhysRevLett.13.321.

[71] Glennys R. Farrar and Pierre Fayet. "Phenomenology of the production, decay, and detection of new hadronic states associated with supersymmetry". In: *Physics Letters B* 76.5 (1978), pp. 575–579. ISSN: 0370-2693. DOI: https://doi.org/10.1016/0370-2693(78)90858-4. URL: http://www.sciencedirect.com/science/article/pii/0370269378908584.

[72] Richard P. Feynman. "Relativistic Cut-Off for Quantum Electrodynamics". In: *Phys. Rev.* 74 (10 Nov. 1948), pp. 1430–1438. DOI: 10.1103/PhysRev.74.1430. URL: https://link.aps.org/doi/10.1103/PhysRev.74.1430.

[73] D. de Florian et al. "Handbook of LHC Higgs Cross Sections: 4. Deciphering the Nature of the Higgs Sector". In: (2016). DOI: 10.23731/CYRM-2017-002. arXiv: 1610.07922 [hep-ph].

[74] Rikkert Frederix and Stefano Frixione. "Merging meets matching in MC@NLO". In: *JHEP* 12 (2012), p. 061. DOI: 10.1007/JHEP12(2012)061. arXiv: 1209.6215 [hep-ph].

[75] Rikkert Frederix, Davide Pagani, and Marco Zaro. "Large NLO corrections in $t\bar{t}W^{\pm}$ and $t\bar{t}t\bar{t}$ hadroproduction from supposedly subleading EW contributions".

In: *JHEP* 02 (2018), p. 031. DOI: 10.1007/JHEP02(2018)031. arXiv: 1711.02116 [hep-ph].

[76] Rikkert Frederix, Emanuele Re, and Paolo Torrielli. "Single-top t-channel hadroproduction in the four-flavour scheme with POWHEG and aMC@NLO". In: *JHEP* 09 (2012), p. 130. DOI: 10.1007/JHEP09(2012)130. arXiv: 1207.5391 [hep-ph].

[77] Rikkert Frederix et al. "Four-lepton production at hadron colliders: aMC@NLO predictions with theoretical uncertainties". In: *JHEP* 02 (2012), p. 099. DOI: 10.1007/JHEP02(2012)099. arXiv: 1110.4738 [hep-ph].

[78] Stefano Frixione. "Isolated photons in perturbative QCD". In: *Phys. Lett. B* 429 (1998), pp. 369–374. DOI: 10.1016/S0370-2693(98)00454-7. arXiv: hep-ph/9801442.

[79] Stefano Frixione, Paolo Nason, and Carlo Oleari. "Matching NLO QCD computations with Parton Shower simulations: the POWHEG method". In: *JHEP* 11 (2007), p. 070. DOI: 10.1088/1126-6708/2007/11/070. arXiv: 0709.2092 [hep-ph].

[80] Stefano Frixione, Paolo Nason, and Giovanni Ridolfi. "A positive-weight next-to-leading-order Monte Carlo for heavy flavour hadroproduction". In: *JHEP* 09 (2007), p. 126. DOI: 10.1088/1126-6708/2007/09/126. arXiv: 0707.3088 [hep-ph].

[81] Stefano Frixione et al. “Angular correlations of lepton pairs from vector boson and top quark decays in Monte Carlo simulations”. In: *JHEP* 04 (2007), p. 081. DOI: 10.1088/1126-6708/2007/04/081. arXiv: hep-ph/0702198.

[82] Stefano Frixione et al. “Single-top hadroproduction in association with a W boson”. In: *JHEP* 07 (2008), p. 029. DOI: 10.1088/1126-6708/2008/07/029. arXiv: 0805.3067 [hep-ph].

[83] R. Frühwirth. “Application of Kalman filtering to track and vertex fitting”. In: *Nuclear Instruments and Methods in Physics Research Section A: Accelerators, Spectrometers, Detectors and Associated Equipment* 262.2 (1987), pp. 444–450. ISSN: 0168-9002. DOI: https://doi.org/10.1016/0168-9002(87)90887-4. URL: http://www.sciencedirect.com/science/article/pii/0168900287908874.

[84] Jun Gao et al. “CT10 next-to-next-to-leading order global analysis of QCD”. In: *Phys. Rev. D* 89 (2014), p. 033009. DOI: 10.1103/PhysRevD.89.033009. arXiv: 1302.6246 [hep-ph].

[85] G. F. Giudice and R. Rattazzi. “Theories with gauge mediated supersymmetry breaking”. In: *Phys. Rept.* 322 (1999), pp. 419–499. DOI: 10.1016/S0370-1573(99)00042-3. arXiv: hep-ph/9801271 [hep-ph].

[86] S. L. Glashow. “Partial Symmetries of Weak Interactions”. In: *Nucl. Phys.* 22 (1961), pp. 579–588. DOI: 10.1016/0029-5582(61)90469-2.

[87] T. Gleisberg et al. “Event generation with SHERPA 1.1”. In: *JHEP* 02 (2009), p. 007. DOI: 10.1088/1126-6708/2009/02/007. arXiv: 0811.4622 [hep-ph].

[88] Tanju Gleisberg and Stefan Höche. “Comix, a new matrix element generator”. In: *JHEP* 12 (2008), p. 039. DOI: 10.1088/1126-6708/2008/12/039. arXiv: 0808.3674 [hep-ph].

[89] Piotr Golonka and Zbigniew Was. “PHOTOS Monte Carlo: A Precision tool for QED corrections in Z and W decays”. In: *Eur. Phys. J. C* 45 (2006), pp. 97–107. DOI: 10.1140/epjc/s2005-02396-4. arXiv: hep-ph/0506026.

[90] Rudolf Haag, Jan T. Łopuszański, and Martin Sohnius. “All possible generators of supersymmetries of the S-matrix”. In: *Nuclear Physics B* 88.2 (1975), pp. 257–274. ISSN: 0550-3213. DOI: https://doi.org/10.1016/0550-3213(75)90279-5. URL: http://www.sciencedirect.com/science/article/pii/0550321375902795.

[91] Julie Haffner. “The CERN accelerator complex. Complexe des accélérateurs du CERN”. In: (Oct. 2013). General Photo. URL: https://cds.cern.ch/record/1621894.

[92] Keith Hamilton, Paolo Nason, and Giulia Zanderighi. “MINLO: Multi-Scale Improved NLO”. In: *JHEP* 10 (2012), p. 155. DOI: 10.1007/JHEP10(2012)155. arXiv: 1206.3572 [hep-ph].

[93] Keith Hamilton et al. "Merging H/W/Z + 0 and 1 jet at NLO with no merging scale: a path to parton shower + NNLO matching". In: *JHEP* 05 (2013), p. 082. DOI: 10.1007/JHEP05(2013)082. arXiv: 1212.4504 [hep-ph].

[94] L.A. Harland-Lang et al. "Parton distributions in the LHC era: MMHT 2014 PDFs". In: *Eur. Phys. J. C* 75.5 (2015), p. 204. DOI: 10.1140/epjc/s10052-015-3397-6. arXiv: 1412.3989 [hep-ph].

[95] Heribertus B. Hartanto et al. "Higgs boson production in association with top quarks in the POWHEG BOX". In: *Phys. Rev. D* 91.9 (2015), p. 094003. DOI: 10.1103/PhysRevD.91.094003. arXiv: 1501.04498 [hep-ph].

[96] W. Heisenberg. "Über den anschaulichen Inhalt der quantentheoretischen Kinematik und Mechanik". In: *Zeitschrift fur Physik* 43.3-4 (Mar. 1927), pp. 172–198. DOI: 10.1007/BF01397280.

[97] P.W. Higgs. "Broken symmetries, massless particles and gauge fields". In: *Physics Letters* 12.2 (1964), pp. 132–133. ISSN: 0031-9163. DOI: https://doi.org/10.1016/0031-9163(64)91136-9. URL: http://www.sciencedirect.com/science/article/pii/0031916364911369.

[98] Stefan Höche et al. "A critical appraisal of NLO+PS matching methods". In: *JHEP* 09 (2012), p. 049. DOI: 10.1007/JHEP09(2012)049. arXiv: 1111.1220 [hep-ph].

[99] Stefan Höche et al. "QCD matrix elements + parton showers. The NLO case". In: *JHEP* 04 (2013), p. 027. DOI: 10.1007/JHEP04(2013)027. arXiv: 1207.5030 [hep-ph].

[100] Stefan Höche et al. "QCD matrix elements and truncated showers". In: *JHEP* 05 (2009), p. 053. DOI: 10.1088/1126-6708/2009/05/053. arXiv: 0903.1219 [hep-ph].

[101] Masahiro Ibe, Shigeki Matsumoto, and Ryosuke Sato. "Mass Splitting between Charged and Neutral Winos at Two-Loop Level". In: *Phys. Lett.* B721 (2013), pp. 252–260. DOI: 10.1016/j.physletb.2013.03.015. arXiv: 1212.5989 [hep-ph].

[102] J. Illingworth and J. Kittler. "A survey of the hough transform". In: *Computer Vision, Graphics, and Image Processing* 44.1 (1988), pp. 87–116. ISSN: 0734-189X. DOI: https://doi.org/10.1016/S0734-189X(88)80033-1. URL: http://www.sciencedirect.com/science/article/pii/S0734189X88800331.

[103] Dong-Won Jung and Jae Yong Lee. *Anomaly-Mediated Supersymmetry Breaking Demystified*. 2009. arXiv: 0902.0464 [hep-ph].

[104] P. Kant et al. "HatHor for single top-quark production: Updated predictions and uncertainty estimates for single top-quark production in hadronic collisions". In: *Comput. Phys. Commun.* 191 (2015), pp. 74–89. DOI: 10.1016/j.cpc.2015.02.001. arXiv: 1406.4403 [hep-ph].

[105] K. Kodama et al. "Observation of tau neutrino interactions". In: *Phys. Lett.* B504 (2001), pp. 218–224. DOI: 10.1016/S0370-2693(01)00307-0. arXiv: hep-ex/0012035 [hep-ex].

[106] Kamila Kowalska and Enrico Maria Sessolo. "The discreet charm of higgsino dark matter - a pocket review". In: *Adv. High Energy Phys.* 2018 (2018), p. 6828560. DOI: 10.1155/2018/6828560. arXiv: 1802.04097 [hep-ph].

[107] Graham D. Kribs, Takemichi Okui, and Tuhin S. Roy. "Viable Gravity-Mediated Supersymmetry Breaking". In: *Phys. Rev.* D82 (2010), p. 115010. DOI: 10.1103/PhysRevD.82.115010. arXiv: 1008.1798 [hep-ph].

[108] Hung-Liang Lai et al. "New parton distributions for collider physics". In: *Phys. Rev. D* 82 (2010), p. 074024. DOI: 10.1103/PhysRevD.82.074024. arXiv: 1007.2241 [hep-ph].

[109] Lev Davidovich Landau. "On the energy loss of fast particles by ionization". In: *J. Phys.* 8.4 (1944), pp. 201–205. URL: https://cds.cern.ch/record/216256.

[110] LHCTopWG. "NLO single-top channel cross sections". In: (2017). URL: https://twiki.cern.ch/twiki/bin/view/LHCPhysics/SingleTopRefXsec.

[111] LHCTopWG. "NNLO+NNLL top-quark-pair cross sections". In: (2015). URL: https://twiki.cern.ch/twiki/bin/view/LHCPhysics/TtbarNNLO.

[112] Leif Lönnblad. "Correcting the Colour-Dipole Cascade Model with Fixed Order Matrix Elements". In: *JHEP* 05 (2002), p. 046. DOI: 10.1088/1126-6708/2002/05/046. arXiv: hep-ph/0112284.

[113] Leif Lönnblad and Stefan Prestel. "Matching tree-level matrix elements with interleaved showers". In: *JHEP* 03 (2012), p. 019. DOI: 10.1007/JHEP03(2012)019. arXiv: 1109.4829 [hep-ph].

[114] *Luminosity determination in pp collisions at* $\sqrt{s} = 13$ *TeV using the ATLAS detector at the LHC*. Tech. rep. ATLAS-CONF-2019-021. Geneva: CERN, June 2019. URL: http://cds.cern.ch/record/2677054.

[115] M. Bahr et al. "Herwig++ physics and manual". In: *Eur. Phys. J. C* 58 (2008), pp. 639–707. DOI: 10.1140/epjc/s10052-008-0798-9. arXiv: 0803.0883 [hep-ph].

[116] A. D. Martin et al. "Parton distributions for the LHC". In: *Eur. Phys. J. C* 63 (2009), pp. 189–285. DOI: 10.1140/epjc/s10052-009-1072-5. arXiv: 0901.0002 [hep-ph].

[117] A. D. Martin et al. "Uncertainties on α_S in global PDF analyses and implications for predicted hadronic cross sections". In: *Eur. Phys. J. C* 64 (2009), pp. 653–680. DOI: 10.1140/epjc/s10052-009-1164-2. arXiv: 0905.3531 [hep-ph].

[118] Stephen P. Martin. "A Supersymmetry primer". In: (1997). [Adv. Ser. Direct. High Energy Phys.18,1(1998)], pp. 1–98. DOI: 10.1142/9789812839657_0001, 10.1142/9789814307505_0001. arXiv: hep-ph/9709356 [hep-ph].

[119] Tom Melia et al. "W^+W^-, WZ and ZZ production in the POWHEG BOX". In: *JHEP* 11 (2011), p. 078. DOI: 10.1007/JHEP11(2011)078. arXiv: 1107.5051 [hep-ph].

[120] Kirill Melnikov, Markus Schulze, and Andreas Scharf. "QCD corrections to top quark pair production in association with a photon at hadron colliders". In: *Phys. Rev. D* 83 (2011), p. 074013. DOI: 10.1103/PhysRevD.83.074013. arXiv: 1102.1967 [hep-ph].

[121] Michaela Mlynarikova. "Performance of the ATLAS hadronic Tile calorimeter". In: *5th Large Hadron Collider Physics Conference (LHCP 2017) Shanghai, China, May 15-20, 2017*. 2017. arXiv: 1709.00100 [physics.ins-det].

[122] S. Mrenna and P. Skands. "Automated parton-shower variations in PYTHIA 8". In: *Phys. Rev. D* 94 (2016), p. 074005. DOI: 10.1103/PhysRevD.94.074005. arXiv: 1605.08352 [hep-ph].

[123] *Muon Momentum Resolution in First Pass Reconstruction of pp Collision Data Recorded by ATLAS in 2010*. Tech. rep. ATLAS-CONF-2011-046. Geneva: CERN, Mar. 2011. URL: https://cds.cern.ch/record/1338575.

[124] Natsumi Nagata and Satoshi Shirai. "Higgsino Dark Matter in High-Scale Supersymmetry". In: *JHEP* 01 (2015), p. 029. DOI: 10.1007/JHEP01(2015)029. arXiv: 1410.4549 [hep-ph].

[125] Paolo Nason. "A new method for combining NLO QCD with shower Monte Carlo algorithms". In: *JHEP* 11 (2004), p. 040. DOI: 10.1088/1126-6708/2004/11/040. arXiv: hep-ph/0409146.

[126] Paolo Nason and Giulia Zanderighi. "W^+W^- , WZ and ZZ production in the POWHEG-BOX-V2". In: *Eur. Phys. J. C* 74.1 (2014), p. 2702. DOI: 10.1140/epjc/s10052-013-2702-5. arXiv: 1311.1365 [hep-ph].

[127] NNPDF Collaboration, R.D. Ball et al. "Parton distributions for the LHC Run II". In: *JHEP* 04 (2015), p. 040. DOI: 10.1007/JHEP04(2015)040. arXiv: 1410.8849 [hep-ph].

[128] Emmy Noether. "Invariant variation problems". In: *Transport Theory and Statistical Physics* 1.3 (1971), pp. 186–207. DOI: 10.1080/00411457108231446. eprint: https://doi.org/10.1080/00411457108231446. URL: https://doi.org/10.1080/00411457108231446.

[129] Susumu Oda. *Conditions Tag*. URL: https://twiki.cern.ch/twiki/bin/view/AtlasComputing/ConditionsTagOflCondMc16Sdr14.

[130] Michele Papucci, Joshua T. Ruderman, and Andreas Weiler. "Natural SUSY Endures". In: *JHEP* 09 (2012), p. 035. DOI: 10.1007/JHEP09(2012)035. arXiv: 1110.6926 [hep-ph].

[131] C. Patrignani et al. "Review of Particle Physics". In: *Chin. Phys.* C40.10 (2016), p. 100001. DOI: 10.1088/1674-1137/40/10/100001.

[132] S. Perlmutter et al. "Measurements of Ω and Λ from 42 High-Redshift Supernovae". In: 517.2 (June 1999), pp. 565–586. DOI: 10.1086/307221. arXiv: astro-ph/9812133 [astro-ph].

[133] J. Pumplin et al. “New Generation of Parton Distributions with Uncertainties From Global QCD Analysis”. In: *JHEP* 07 (2002), p. 012. DOI: 10.1088/1126-6708/2002/07/012. arXiv: hep-ph/0201195.

[134] Emanuele Re. “Single-top Wt-channel production matched with parton showers using the POWHEG method”. In: *Eur. Phys. J. C* 71 (2011), p. 1547. DOI: 10.1140/epjc/s10052-011-1547-z. arXiv: 1009.2450 [hep-ph].

[135] Adam G. Riess et al. “Observational Evidence from Supernovae for an Accelerating Universe and a Cosmological Constant”. In: 116.3 (Sept. 1998), pp. 1009–1038. DOI: 10.1086/300499. arXiv: astro-ph/9805201 [astro-ph].

[136] V. C. Rubin, Jr. Ford W. K., and N. Thonnard. “Extended rotation curves of high-luminosity spiral galaxies. IV. Systematic dynamical properties, Sa -> Sc.” In: 225 (Nov. 1978), pp. L107–L111. DOI: 10.1086/182804.

[137] Masahiko Saito et al. “Discovery reach for wino and higgsino dark matter with a disappearing track signature at a 100 TeV pp collider”. In: *The European Physical Journal C* 79.6 (June 2019), p. 469. ISSN: 1434-6052. DOI: {10.1140/epjc/s10052-019-6974-2}. URL: %7Bhttps://doi.org/10.1140/epjc/s10052-019-6974-2%7D.

[138] Abdus Salam. “Weak and Electromagnetic Interactions”. In: *Conf. Proc.* C680519 (1968), pp. 367–377. DOI: 10.1142/9789812795915_0034.

[139] E. Schrödinger. "An Undulatory Theory of the Mechanics of Atoms and Molecules". In: *Physical Review* 28.6 (Dec. 1926), pp. 1049–1070. DOI: 10.1103/PhysRev.28.1049.

[140] Steffen Schumann and Frank Krauss. "A Parton shower algorithm based on Catani-Seymour dipole factorisation". In: *JHEP* 03 (2008), p. 038. DOI: 10.1088/1126-6708/2008/03/038. arXiv: 0709.1027 [hep-ph].

[141] P. Schwegler et al. "Improvement of the L1 trigger for the ATLAS muon spectrometer at high luminosity". In: *Nuclear Instruments and Methods in Physics Research Section A: Accelerators, Spectrometers, Detectors and Associated Equipment* 718 (2013). Proceedings of the 12th Pisa Meeting on Advanced Detectors, pp. 245–247. ISSN: 0168-9002. DOI: https://doi.org/10.1016/j.nima.2013.01.023. URL: http://www.sciencedirect.com/science/article/pii/S0168900213000703.

[142] Julian Schwinger. "Quantum Electrodynamics. I. A Covariant Formulation". In: *Phys. Rev.* 74 (10 Nov. 1948), pp. 1439–1461. DOI: 10.1103/PhysRev.74.1439. URL: https://link.aps.org/doi/10.1103/PhysRev.74.1439.

[143] Frank Siegert. "A practical guide to event generation for prompt photon production with Sherpa". In: *J. Phys. G* 44.4 (2017), p. 044007. DOI: 10.1088/1361-6471/aa5f29. arXiv: 1611.07226 [hep-ph].

[144] T. Sjöstrand, S. Mrenna, and P. Skands. "A brief introduction to PYTHIA 8.1". In: *Comput. Phys. Commun.* 178 (2008), pp. 852–867. DOI: 10.1016/j.cpc.2008.01.036. arXiv: 0710.3820 [hep-ph].

[145] Torbjorn Sjöstrand. "Jet fragmentation of multiparton configurations in a string framework". In: *Nucl. Phys. B* 248 (1984), pp. 469–502. DOI: 10.1016/0550-3213(84)90607-2.

[146] Torbjorn Sjöstrand, Stephen Mrenna, and Peter Z. Skands. "PYTHIA 6.4 Physics and Manual". In: *JHEP* 05 (2006), p. 026. DOI: 10.1088/1126-6708/2006/05/026. arXiv: hep-ph/0603175.

[147] Torbjörn Sjöstrand et al. "An introduction to PYTHIA 8.2". In: *Comput. Phys. Commun.* 191 (2015), pp. 159–177. DOI: 10.1016/j.cpc.2015.01.024. arXiv: 1410.3012 [hep-ph].

[148] Tomasz Skwarnicki. "A study of the radiative CASCADE transitions between the Upsilon-Prime and Upsilon resonances". PhD thesis. Cracow, INP, 1986. URL: http://www-library.desy.de/cgi-bin/showprep.pl?DESY-F31-86-02.

[149] Glenn D. Starkman et al. "Opening the window on strongly interacting dark matter". In: *Phys. Rev. D* 41 (12 June 1990), pp. 3594–3603. DOI: 10.1103/PhysRevD.41.3594. URL: https://link.aps.org/doi/10.1103/PhysRevD.41.3594.

[150] Scott D. Thomas and James D. Wells. "Phenomenology of Massive Vectorlike Doublet Leptons". In: *Phys. Rev. Lett.* 81 (1998), pp. 34–37. DOI: 10.1103/PhysRevLett.81.34. arXiv: hep-ph/9804359 [hep-ph].

[151] S. Tomonaga. "On a Relativistically Invariant Formulation of the Quantum Theory of Wave Fields*". In: *Progress of Theoretical Physics* 1.2 (Aug. 1946), pp. 27–42. ISSN: 0033-068X. DOI: 10.1143/PTP.1.27. eprint: http://oup.prod.sis.lan/ptp/article-pdf/1/2/27/24027031/1-2-27.pdf. URL: https://doi.org/10.1143/PTP.1.27.

[152] *Track Reconstruction Performance of the ATLAS Inner Detector at* $\sqrt{s}$ *= 13 TeV*. Tech. rep. ATL-PHYS-PUB-2015-018. Geneva: CERN, July 2015.

[153] Steven Weinberg. "A Model of Leptons". In: *Phys. Rev. Lett.* 19 (1967), pp. 1264–1266. DOI: 10.1103/PhysRevLett.19.1264.

[154] Jan-Christopher Winter, Frank Krauss, and Gerhard Soff. "A modified cluster-hadronization model". In: *Eur. Phys. J. C* 36 (2004), pp. 381–395. DOI: 10.1140/epjc/s2004-01960-8. arXiv: hep-ph/0311085.

PMGRefs

Appendix A

Anomaly-Mediated Supersymmetry Breaking

Minimal AMSB models are characterized by several main parameters: the gravitino mass $m_{\frac{3}{2}}$, the universal scalar mass m_0, the ratio of the Higgs vacuum expectation values at the electroweak scale $tan(\beta)$, and the sign of the higgsino mass term $sgn(\mu)$.

A generic feature of these models is mass-degeneracy between the lightest supersymmetric particle (LSP) and the next to lightest supersymmetric particle (NLSP), which are a neutralino ($\tilde{\chi}_1^0$) and chargino ($\tilde{\chi}_1^{\pm}$), respectively. Radiative corrections from the electroweak gauge bosons increase the mass of the chargino relative to the neutralino by about 165 MeV for charginos with mass greater than a couple hundred GeV; radiative corrections from SUSY particles are too small to be of concern assuming most SUSY

particles have high mass. The chargino decays into the neutralino and a charged pion with decay width given by:

$$\Gamma(\tilde{\chi}_1^{\pm} \to \tilde{\chi}_1^0 \pi^{\pm}) = \frac{2G_F^2}{\pi} cos^2(\theta_c) f_\pi^2 \Delta m_{\tilde{\chi}_1}^3 \left(1 - \frac{m_\pi^2}{\Delta m_{\tilde{\chi}_1}^2}\right)^{\frac{1}{2}} \tag{A.1}$$

where the terms G_F, θ_c, f_π, and m_π are the Fermi coupling constant, the Cabbibo angle, the pion decay constant ($\approx 130\,\text{MeV}$), and the pion mass ($\approx 140\,\text{MeV}$), respectively. This corresponds to a half-life of about $\tau_{\tilde{\chi}_1^{\pm}} \approx 0.2\,\text{ns}$, long enough for a non-negligible number of charginos to make it into the detector before decaying.

Charginos can be produced either directly via electroweak production or from the decay of gluinos via strong production. Electroweak production has the advantage of being independent of gluino mass whereas strong production has the advantage of much higher cross-section if the gluino is relatively light. In minimal AMSB models, the gaugino masses are proportional to the coefficients of the renormalization group equations of their corresponding symmetry group:

$$M_i = -\frac{b_i g_i}{16\pi^2} m_{\frac{3}{2}}, \tag{A.2}$$

where $i = 1, 2, 3$ for symmetry group $U(1)$, $SU(2)$, and $SU(3)$, respectively. This means the mass ratios for the bino, wino, and gluino are $M_1 : M_2 : M_3 \approx 3 : 1 : 7$. The gluino having a mass roughly $7x$ greater than the wino results in electroweak production having a cross-section roughly $1000x$ higher than strong production, as such this analysis focuses entirely on electroweak production.

Appendix B

Generic Effect of the Smearing Function

The effect of smearing the $\frac{q}{p_T}$ on the final p_T distribution can be considered from a purely mathematical perspective. In ATLAS tracking, $\frac{q}{p_T}$ is the gaussian-distributed track parameter related to transverse momentum; therefore it is this inverse term which is actually smeared. The smearing procedure begins by inverting the transverse momentum, yielding a new quantity $d = \frac{1}{p_T}$; the factor q has been dropped because all of the particles under consideration have $|q| = 1$, and the absolute value is taken so the sign of q can be ignored here. We then add a term drawn at random from a distribution $f(z)$:

$$d_{smear} = d + Random(f(z)), \tag{B.1}$$

which is the quantity that gets inverted to yield the smeared transverse momentum:

$$p_T^{smear} = \left| \frac{1}{d_{smear}} \right|. \tag{B.2}$$

Transverse momentum must be either positive or zero, hence the absolute value taken above. This has important consequences for the effect of smearing on the distribution. If the number drawn at random, $R(f(z))$, is positive, then we have:

$$\begin{aligned} d_{smear} &= d + R(f(z)) > d \\ &\rightarrow p_T^{smear} < p_T \end{aligned} \tag{B.3}$$

If the randomly drawn number is negative, the effect depends on its precise value. If $-2d < R(f(z)) < 0$, then:

$$\begin{aligned} d_{smear} &= d + R(f(z)) \\ &\rightarrow -d < d_{smear} < d \\ &\rightarrow p_T^{smear} > p_T, \end{aligned} \tag{B.4}$$

but if we have $R(f(z)) < -2d$, then:

$$\begin{aligned} d_{smear} &= d + R(f(z)) < -d \\ &\rightarrow p_T^{smear} < p_T. \end{aligned} \tag{B.5}$$

All positive values drawn from the smearing function result in a smeared transverse momentum value which is lower than the original, but only *some* negative values result in the smeared value being higher than the original, the rest of the negatives cause $p_T^{smear} < p_T$ as well.

The effect on the overall distribution of smeared vs original transverse momentum depends on the nature of the smearing function $f(z)$: in this case, we see $f(z)$ is symmetric about $z = 0$, positive definite, and continuous along the entire real number

line. This has immediate consequences:

$$\int_{-b}^{0} f(z)dz = \int_{0}^{b} f(z)dz, \, \forall b \in \mathbb{R}, \tag{B.6}$$

as well as

$$\int_{0}^{b+\delta} f(z)dz > \int_{0}^{b} f(z)dz, \, \forall \delta \in \mathbb{R}^{+}. \tag{B.7}$$

In order for the smeared transverse momentum to be higher than the original, we must have $-2d < R(f(z)) < 0$, as described above. The probability for this to happen is proportional to the integral of $f(z)$ in that range, with the proportionality coming from the normalization of the integral across the entire real-number line. We therefore have:

$$P(p_T^{smear} > p_T) = \frac{\int_{-2d}^{0} f(z)dz}{\int_{-\infty}^{\infty} f(z)dz}. \tag{B.8}$$

By the first of the above properties of symmetric, positive definite functions, we can re-write the denominator as:

$$\int_{-\infty}^{\infty} f(z)dz = 2\int_{0}^{\infty} f(z)dz. \tag{B.9}$$

By the second of the above properties of symmetric, positive definite functions, we can say of the numerator:

$$\int_{-2d}^{0} f(z)dz < \int_{0}^{\infty} f(z)dz \quad \forall \, \text{finite} \, d. \tag{B.10}$$

Therefore, we can re-write the numerator as:

$$\int_{-2d}^{0} f(z)dz = \int_{0}^{\infty} f(z)dz - \Delta, \tag{B.11}$$

where Δ is not necessarily small.

Therefore the probability for the smeared transverse momentum to end up higher than

the original transverse momentum is:

$$\begin{aligned} P(p_T^{smear} > p_T) =& \frac{\int_0^\infty f(z)dz - \Delta}{2\int_0^\infty f(z)dz} \\ & \to \frac{1}{2} - \frac{\Delta}{2\int_0^\infty f(z)dz} \\ & \to \frac{1}{2} - \epsilon \\ & \Rightarrow \boxed{P(p_T^{smear} > p_T) < \frac{1}{2} \quad \forall p_T} \end{aligned} \tag{B.12}$$

Appendix C

Example AMSB Mass Points

In addition to the 400.3 GeV mass point, several others were investigated to see how the signal yield declines with increasing chargino mass.

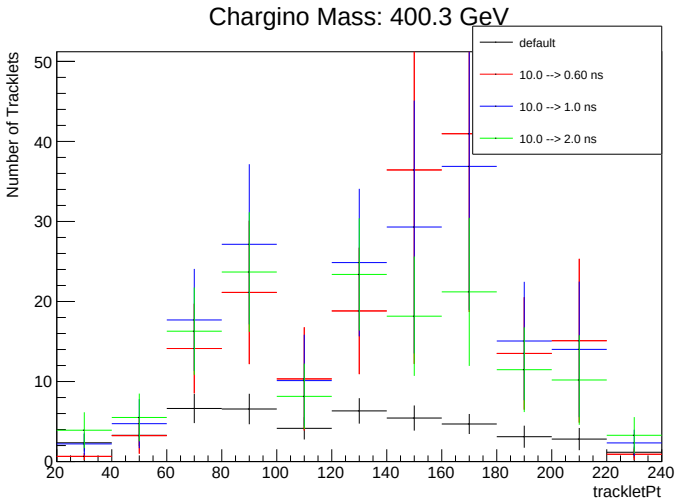

Figure C.1: Tracklet p_T distribution for a chargino with 400.3 GeV and 10 ns base lifetime, reweighted to lifetimes between 0.6, 1.0, and 2.0 ns with 139 fb^{-1} of integrated luminosity

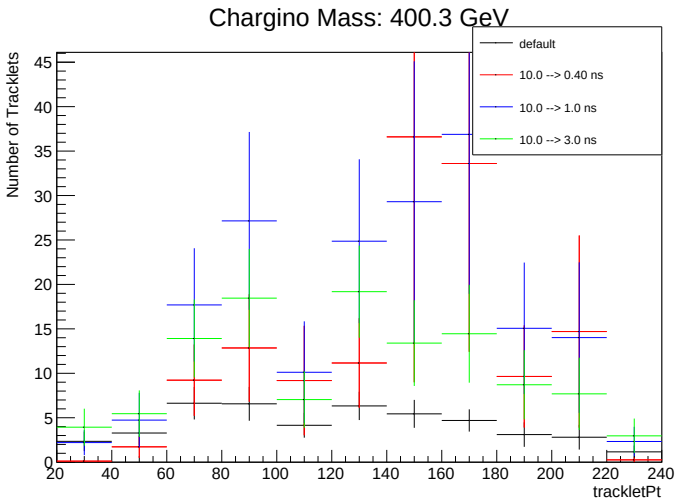

Figure C.2: Tracklet p_T distribution for a chargino with 400.3 GeV mass and 10 ns base lifetime, reweighted to lifetimes of 0.40, 1.0, and 3.0 ns with 139 fb^{-1} of integrated luminosity

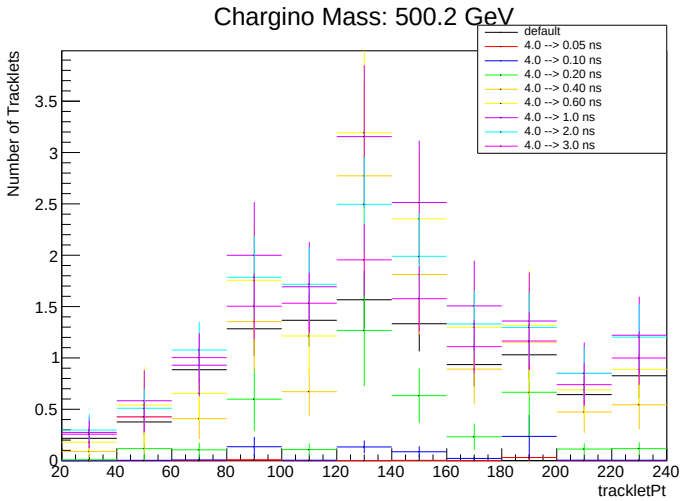

Figure C.3: Tracklet p_T distribution for a Chargino with 500.2 GeV and 4.0 ns base lifetime, reweighted to lifetimes between 0.05 and 3 ns

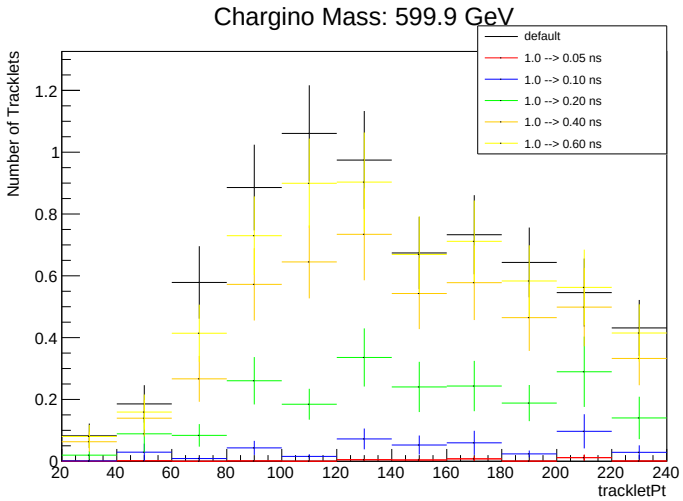

Figure C.4: Tracklet p_T distribution for a Chargino with 599.9 GeV and 1.0 ns base lifetime, reweighted to lifetimes between 0.05 and 0.6 ns

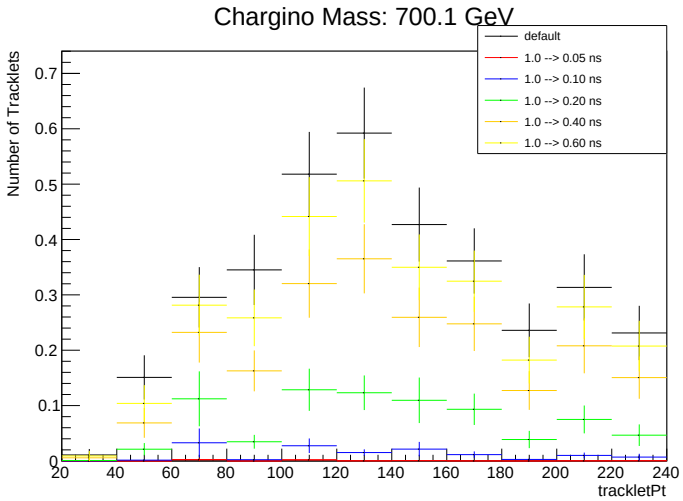

Figure C.5: Tracklet p_T distribution for a Chargino with 700.1 GeV and 1.0 ns base lifetime, reweighted to lifetimes between 0.05 and 0.6 ns

p_T [GeV]	$\tau = 0.4\,\text{ns}$	$\tau = 0.6\,\text{ns}$	$\tau = 1.0\,\text{ns}$	$\tau = 2.0\,\text{ns}$	$\tau = 3.0\,\text{ns}$	$\tau = 10.0\,\text{ns}$	Scaled Background
20	234	290.	310	252	202	78.1	604
40	232	286	305	248	199	75.8	435
60	232	286	303	245	195	72.5	318
80	231	283	298	239	190	65.8	247
100	221	268	280	223	176	59.2	201
120	208	247	253	199	157	55.0	169
140	199	237	242	191	150	48.6	146
160	188	218	217	167	131	43.1	128
180	151	181	188	149	117	38.4	114
200	117	140	151	127	102	35.3	102
220	107	126	136	116	93.7	32.5	93.4
240	92.6	111	121	105	86.0	31.3	85.5

Table C.1: Expected Signals for $m_{\chi^{\pm}} = 400.3\,\text{GeV}$ mass with $139\,\text{fb}^{-1}$ of Integrated Luminosity

Table C.2: Estimated sensitivities for different lifetimes of a 400.3 GeV mass wino-like chargino with 139 fb^{-1} assuming the lepton scatter background is dominant

p_T [GeV]	Sensitivity 0.4 ns	Sensitivity 0.6 ns	Sensitivity 1.0 ns	Sensitivity 2.0 ns	Sensitivity 3.0 ns	Sensitivity 10.0 ns
20	8.99409	11.0133	11.7085	9.63678	7.80072	3.11416
40	10.3229	12.5297	13.2691	10.9839	8.92385	3.53387
60	11.7943	14.2396	14.9941	12.359	10.0378	3.92381
80	12.9868	15.5742	16.3207	13.4107	10.8696	4.01836
100	13.5825	16.102	16.717	13.6514	11.0297	3.99109
120	13.7658	15.98	16.2989	13.2003	10.6889	4.02653
140	13.9987	16.2632	16.6116	13.4666	10.8832	3.8314
160	13.9743	15.8698	15.8574	12.6036	10.1303	3.6285
180	12.0617	14.1193	14.5887	11.897	9.62209	3.42525
200	10.0312	11.7133	12.5217	10.7966	8.90103	3.31098
220	9.62644	11.084	11.813	10.2819	8.51981	3.18757
240	8.73152	10.2361	11.0906	9.79741	8.16618	3.20303

Chargino Mass: 500.2 GeV						
p_T	$\tau = 0.4\,\text{ns}$	$\tau = 0.6\,\text{ns}$	$\tau = 1.0\,\text{ns}$	$\tau = 2.0\,\text{ns}$	$\tau = 3.0\,\text{ns}$	$\tau = 4.0\,\text{ns}$
60	23.255782	28.700810	30.535678	25.882246	21.319621	17.955005
80	22.847449	28.045004	29.606514	24.804866	20.316623	17.069894
100	21.494249	26.289026	27.606801	23.019516	18.813065	15.786179
120	20.822881	25.075454	25.91397	21.302165	17.280551	14.419591

Table C.3: Expected Signal for $m_{\chi^\pm} = 500.2\,\text{GeV}$ with $35\,\text{fb}^{-1}$ of Integrated Luminosity

Chargino Mass: 599.9 GeV				
p_T	$\tau = 0.2\,\text{ns}$	$\tau = 0.4\,\text{ns}$	$\tau = 0.6\,\text{ns}$	$\tau = 1.0\,\text{ns}$
60	4.142222	10.077075	12.899340	14.174302
80	4.058472	9.810457	12.485126	13.595750
100	3.798021	9.238105	11.755335	12.710078
120	3.613550	8.593151	10.855886	11.649318

Table C.4: Expected Signal for $m_{\chi^\pm} = 599.9\,\text{GeV}$ with $35\,\text{fb}^{-1}$ of Integrated Luminosity

Chargino Mass: 700.1 GeV				
p_T	$\tau = 0.2\,\text{ns}$	$\tau = 0.4\,\text{ns}$	$\tau = 0.6\,\text{ns}$	$\tau = 1.0\,\text{ns}$
60	1.847589	4.913110	6.551843	7.506866
80	1.735374	4.680883	6.270475	7.211332
100	1.700716	4.518186	6.012011	6.866225
120	1.572167	4.197837	5.570472	6.348202

Table C.5: Expected Signal for $m_{\chi^\pm} = 700.1\,\text{GeV}$ with $35\,\text{fb}^{-1}$ of Integrated Luminosity

Appendix D

Z-peak Fit Plots

This is the full set of plots fitting the Z-peak. See Table 6.1 and Table 6.2 the selection criteria which went into producing these plots. These plots can be found in the two root files here: `https://github.com/Astromax/ATLAS_DisappearingTrack_logs` The parameters for the Z peak fit are found in the respective log files in that same link.

Appendix E

Plots showing the differential impact of $E_T^{miss,IL}$ on smeared vs unsmeared p_T

These plots show the effect of applying a $E_T^{miss,IL}$ selection on the distributions of smeared and unsmeared p_T in a simplified Control Region which requires only the existence of a single signal lepton which is identified as an electron. In all of these plots, unsmeared is the blue line and smeared is the red line.

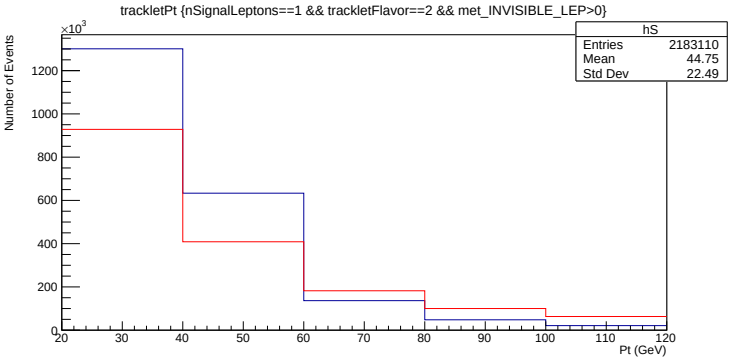

Figure E.1: Distributions with no $E_T^{miss,IL}$ requirement

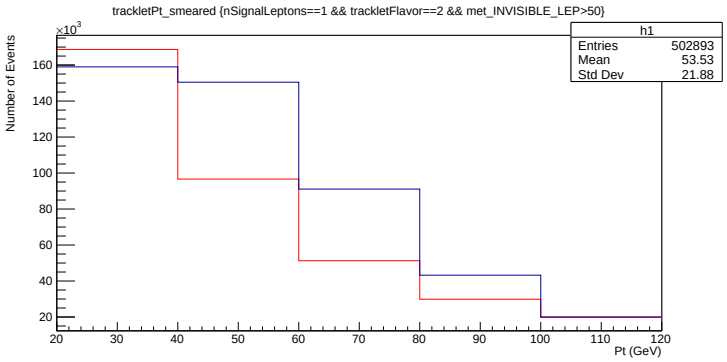

Figure E.2: Distributions with $E_T^{miss,IL} > 50\,\text{GeV}$ requirement

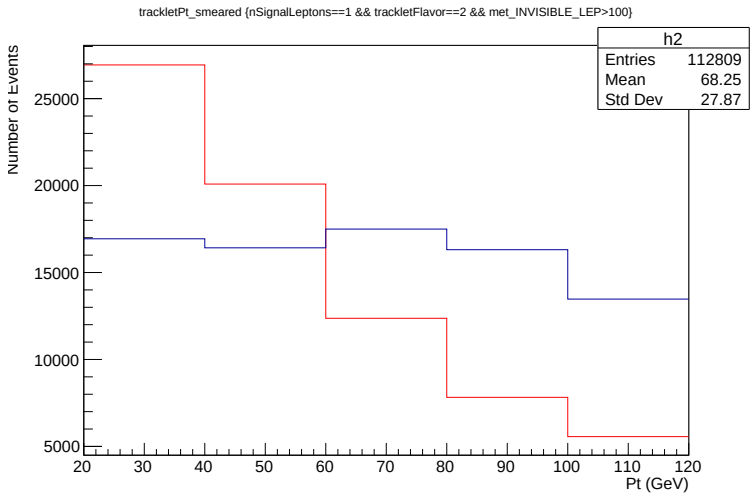

Figure E.3: Distributions with $E_T^{miss,IL} > 100\,\text{GeV}$ requirement

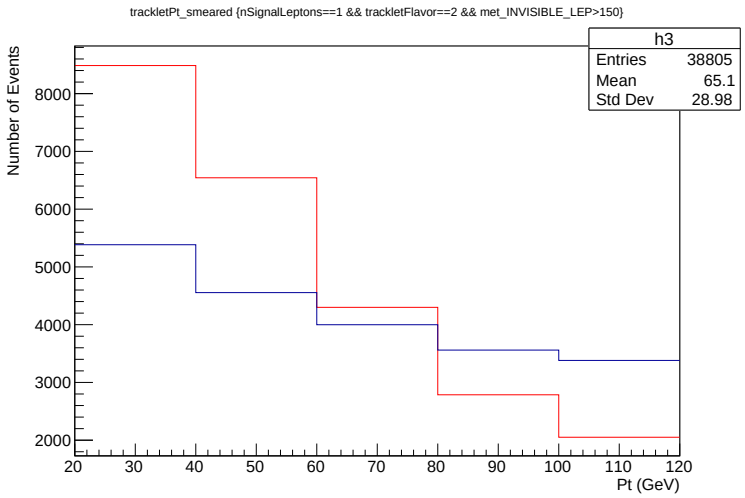

Figure E.4: Distributions with $E_T^{miss,IL} > 150\,\text{GeV}$ requirement

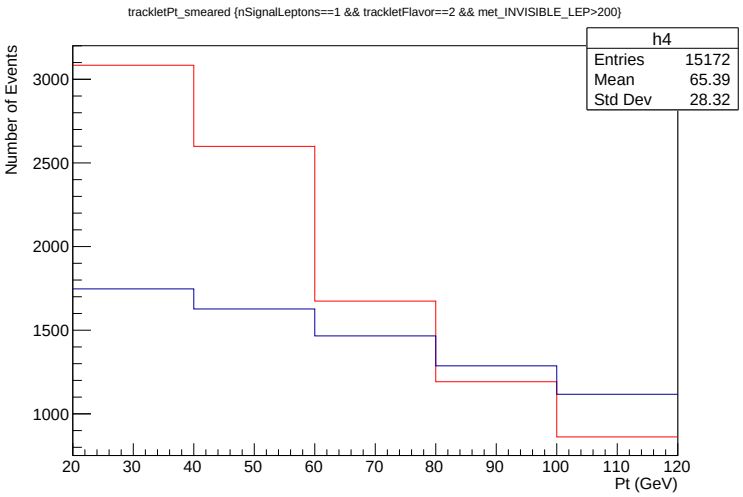

Figure E.5: Distributions with $E_T^{miss,IL} > 200\,\text{GeV}$ requirement

Appendix F

Data and Monte Carlo

This page blank because the tables are too long to fit anything else.

Dataset ID	Process	Tags	$\sigma \times \epsilon$ [pb]	k-factor	Generator efficiency	$\mathcal{L}_{int}$[fb^{-1}]
361106	PowhegPythia8EvtGen_AZNLOCTEQ6L1_Zee	e3601_s3126_r9364_r9315_p3736	1901.1000	1.03	1.000	40.985
361107	PowhegPythia8EvtGen_AZNLOCTEQ6L1_Zmumu	e3601_s3126_r9364_r9315_p3736	1901.1000	1.03	1.000	33.847
361108	PowhegPythia8EvtGen_AZNLOCTEQ6L1_Ztautau	e3601_s3126_r9364_r9315_p3736	1901.1000	1.03	1.000	20.247

Table F.1: $Z \to \ell\ell$ used to test Z tag-and-probe

Dataset ID	Process	Tags	$\sigma \times \epsilon$ [pb]	k-factor	Generator efficiency	$\mathcal{L}_{int}$[fb^{-1}]
364156	Sherpa_221_NNPDF30NNLO_Wmunu_MAXHTPTV0_70_CVetoBVeto	e5340_s3126_r9364_r9315_p3736	19149.0000	0.97	0.825	1.630
364157	Sherpa_221_NNPDF30NNLO_Wmunu_MAXHTPTV0_70_CFilterBVeto	e5340_s3126_r9364_r9315_p3736	19144.0000	0.97	0.131	4.103
364158	Sherpa_221_NNPDF30NNLO_Wmunu_MAXHTPTV0_70_BFilter	e5340_s3126_r9364_r9315_p3736	19138.0000	0.97	0.045	21.095
364159	Sherpa_221_NNPDF30NNLO_Wmunu_MAXHTPTV70_140_CVetoBVeto	e5340_s3126_r9364_r9315_p3736	945.5200	0.97	0.674	24.191
364160	Sherpa_221_NNPDF30NNLO_Wmunu_MAXHTPTV70_140_CFilterBVeto	e5340_s3126_r9364_r9315_p3736	945.3800	0.97	0.244	44.660
364161	Sherpa_221_NNPDF30NNLO_Wmunu_MAXHTPTV70_140_BFilter	e5340_s3126_r9364_r9315_p3736	944.8000	0.97	0.085	257.036
364162	Sherpa_221_NNPDF30NNLO_Wmunu_MAXHTPTV140_280_CVetoBVeto	e5340_s3126_r9364_r9315_p3736	339.7300	0.97	0.600	50.558
364163	Sherpa_221_NNPDF30NNLO_Wmunu_MAXHTPTV140_280_CFilterBVeto	e5340_s3126_r9364_r9315_p3736	339.8000	0.97	0.293	77.761
364164	Sherpa_221_NNPDF30NNLO_Wmunu_MAXHTPTV140_280_BFilter	e5340_s3126_r9364_r9315_p3736	339.6400	0.97	0.110	543.537
364165	Sherpa_221_NNPDF30NNLO_Wmunu_MAXHTPTV280_500_CVetoBVeto	e5340_s3126_r9364_r9315_p3736	72.0790	0.97	0.548	130.523
364166	Sherpa_221_NNPDF30NNLO_Wmunu_MAXHTPTV280_500_CFilterBVeto	e5340_s3126_r9364_r9315_p3736	72.1000	0.97	0.320	133.463
364167	Sherpa_221_NNPDF30NNLO_Wmunu_MAXHTPTV280_500_BFilter	e5340_s3126_r9364_r9315_p3736	72.0580	0.97	0.125	335.246
364168	Sherpa_221_NNPDF30NNLO_Wmunu_MAXHTPTV500_1000	e5340_s3126_r9364_r9315_p3736	15.0060	0.97	1.000	411.950

Table F.2: $W \to \ell\nu$ used to test Z tag-and-probe

Dataset ID	Process	Tags	$\sigma \times \epsilon$ [pb]	k-factor	Generator efficiency	$\mathcal{L}_{int}$[fb^{-1}]
364169	Sherpa_221_NNPDF30NNLO_Wmunu_MAXHTPTV1000_E_CMS	e5340_s3126_r9364_r9315_p3736	1.2348	0.97	1.000	3337.220
364171	Sherpa_221_NNPDF30NNLO_Wenu_MAXHTPTV0_70_CFilterBVeto	e5340_s3126_r9364_r9315_p3736	19144.0000	0.97	0.131	4.081
364172	Sherpa_221_NNPDF30NNLO_Wenu_MAXHTPTV0_70_BFilter	e5340_s3126_r9364_r9315_p3736	19138.0000	0.97	0.045	21.007
364173	Sherpa_221_NNPDF30NNLO_Wenu_MAXHTPTV70_140_CVetoBVeto	e5340_s3126_r9364_r9315_p3736	944.9800	0.97	0.675	23.946
364175	Sherpa_221_NNPDF30NNLO_Wenu_MAXHTPTV70_140_BFilter	e5340_s3126_r9364_r9315_p3736	945.7700	0.97	0.103	104.291
364176	Sherpa_221_NNPDF30NNLO_Wenu_MAXHTPTV140_280_CVetoBVeto	e5340_s3126_r9364_r9315_p3736	339.7500	0.97	0.599	50.682
364177	Sherpa_221_NNPDF30NNLO_Wenu_MAXHTPTV140_280_CFilterBVeto	e5340_s3126_r9364_r9315_p3736	339.8000	0.97	0.288	78.957
364178	Sherpa_221_NNPDF30NNLO_Wenu_MAXHTPTV140_280_BFilter	e5340_s3126_r9364_r9315_p3736	339.6400	0.97	0.109	692.290
364179	Sherpa_221_NNPDF30NNLO_Wenu_MAXHTPTV280_500_CVetoBVeto	e5340_s3126_r9364_r9315_p3736	72.0740	0.97	0.548	130.379
364180	Sherpa_221_NNPDF30NNLO_Wenu_MAXHTPTV280_500_CFilterBVeto	e5340_s3126_r9364_r9315_p3736	72.1050	0.97	0.320	134.115
364181	Sherpa_221_NNPDF30NNLO_Wenu_MAXHTPTV280_500_BFilter	e5340_s3126_r9364_r9315_p3736	72.0910	0.97	0.137	312.737
364183	Sherpa_221_NNPDF30NNLO_Wenu_MAXHTPTV1000_E_CMS	e5340_s3126_r9364_r9315_p3736	1.2344	0.97	1.000	3339.137
364184	Sherpa_221_NNPDF30NNLO_Wtaunu_MAXHTPTV0_70_CVetoBVeto	e5340_s3126_r9364_r9315_p3736	19155.0000	0.97	0.825	1.626
364187	Sherpa_221_NNPDF30NNLO_Wtaunu_MAXHTPTV70_140_CVetoBVeto	e5340_s3126_r9364_r9315_p3736	945.0200	0.97	0.676	24.213
364189	Sherpa_221_NNPDF30NNLO_Wtaunu_MAXHTPTV70_140_BFilter	e5340_s3126_r9364_r9315_p3736	945.7100	0.97	0.104	104.877
364190	Sherpa_221_NNPDF30NNLO_Wtaunu_MAXHTPTV140_280_CVetoBVeto	e5340_s3126_r9364_r9315_p3736	339.6900	0.97	0.599	50.517
364191	Sherpa_221_NNPDF30NNLO_Wtaunu_MAXHTPTV140_280_CFilterBVeto	e5340_s3126_r9364_r9315_p3736	339.8400	0.97	0.285	79.876
364192	Sherpa_221_NNPDF30NNLO_Wtaunu_MAXHTPTV140_280_BFilter	e5340_s3126_r9364_r9315_p3736	339.3100	0.97	0.106	717.921
364193	Sherpa_221_NNPDF30NNLO_Wtaunu_MAXHTPTV280_500_CVetoBVeto	e5340_s3126_r9364_r9315_p3736	72.0780	0.97	0.562	127.267
364194	Sherpa_221_NNPDF30NNLO_Wtaunu_MAXHTPTV280_500_CFilterBVeto	e5340_s3126_r9364_r9315_p3736	71.9900	0.97	0.319	134.732

Table F.3: Remaining $W \to \ell\nu$ used to test Z tag-and-probe

Dataset ID	Process	Tags	$\sigma \times \epsilon$ [pb]	k-factor	Generator efficiency	$\mathcal{L}_{int}$[fb^{-1}]
448486	MGPy8EG_A14N23LO_mAMSB_C1N1_5000_137400_LL0p2_MET60	e7157_s3353_r9364_p3759	0.1179	1.00	0.363	233.770
448487	MGPy8EG_A14N23LO_mAMSB_C1C1_5000_137400_LL0p2_MET60	e7157_s3353_r9364_p3759	0.0568	1.00	0.355	496.395
448496	MGPy8EG_A14N23LO_mAMSB_C1N1_5000_208000_LL1p0_MET60	e7157_s3353_r9364_p3759	0.0194	1.00	0.407	1269.273
448503	MGPy8EG_A14N23LO_mAMSB_C1C1_5000_172600_LL4p0_MET60	e7157_s3353_r9364_p3759	0.0213	1.00	0.384	1224.839
448502	MGPy8EG_A14N23LO_mAMSB_C1N1_5000_172600_LL4p0_MET60	e7157_s3353_r9364_p3759	0.0447	1.00	0.389	574.961
448506	MGPy8EG_A14N23LO_mAMSB_C1N1_5000_137400_LL10p0_MET60	e7157_s3353_r9364_p3759	0.1179	1.00	0.362	233.977
448507	MGPy8EG_A14N23LO_mAMSB_C1C1_5000_137400_LL10p0_MET60	e7157_s3353_r9364_p3759	0.0568	1.00	0.357	493.308
448498	MGPy8EG_A14N23LO_mAMSB_C1N1_5000_243800_LL1p0_MET60	e7157_s3353_r9364_p3759	0.0090	1.00	0.423	2621.791
448499	MGPy8EG_A14N23LO_mAMSB_C1C1_5000_243800_LL1p0_MET60	e7157_s3353_r9364_p3759	0.0042	1.00	0.422	5654.188
448497	MGPy8EG_A14N23LO_mAMSB_C1C1_5000_208000_LL1p0_MET60	e7157_s3353_r9364_p3759	0.0091	1.00	0.406	2699.628

Table F.4: Chargino samples used in final comparison with background

Dataset ID	Process	Tags	$\sigma \times \epsilon$ [pb]	k-factor	Generator efficiency	$\mathcal{L}_{int}$[fb^{-1}]
410644	PowhegPythia8EvtGen_A14_singletop_schan_lept_top	e6527_e5984_s3126_r9364_r9315_p3736	2.0270	1.02	1.000	970.187
410645	PowhegPythia8EvtGen_A14_singletop_schan_lept_antitop	e6527_e5984_s3126_r9364_r9315_p3736	1.2674	1.02	1.000	1552.113
410647	PowhegPythia8EvtGen_A14_Wt_DR_inclusive_antitop	e6552_e5984_s3126_r9364_r9315_p3736	37.9050	0.95	1.000	139.455

Table F.5: Single t MC samples

Dataset ID	Process	Tags	$\sigma \times \epsilon$ [pb]	k-factor	Generator efficiency	$\mathcal{L}_{int}$[fb^{-1}]
364142	Sherpa_221_NNPDF30NNLO_Znunu_MAXHTPTV0_70_CVetoBVeto	e5308_s3126_r9364_r9315_p3736	10706.0000	0.97	0.821	1.169
364143	Sherpa_221_NNPDF30NNLO_Znunu_MAXHTPTV0_70_CFilterBVeto	e5308_s3126_r9364_r9315_p3736	10705.0000	0.97	0.112	6.810
364144	Sherpa_221_NNPDF30NNLO_Znunu_MAXHTPTV0_70_BFilter	e5308_s3126_r9364_r9315_p3736	10707.0000	0.97	0.067	11.314
364145	Sherpa_221_NNPDF30NNLO_Znunu_MAXHTPTV70_140_CVetoBVeto	e5308_s3126_r9364_r9315_p3736	607.8300	0.97	0.691	33.514
364146	Sherpa_221_NNPDF30NNLO_Znunu_MAXHTPTV70_140_CFilterBVeto	e5308_s3126_r9364_r9315_p3736	606.9000	0.97	0.190	127.195
364147	Sherpa_221_NNPDF30NNLO_Znunu_MAXHTPTV70_140_BFilter	e5308_s3126_r9364_r9315_p3736	608.5500	0.97	0.120	273.486
364148	Sherpa_221_NNPDF30NNLO_Znunu_MAXHTPTV140_280_CVetoBVeto	e5308_s3126_r9364_r9315_p3736	222.3600	0.97	0.614	108.650
364149	Sherpa_221_NNPDF30NNLO_Znunu_MAXHTPTV140_280_CFilterBVeto	e5308_s3126_r9364_r9315_p3736	222.3500	0.97	0.233	245.946
364150	Sherpa_221_NNPDF30NNLO_Znunu_MAXHTPTV140_280_BFilter	e5308_e5984_s3126_r9364_r9315_p3736	222.3800	0.97	0.158	585.829
364151	Sherpa_221_NNPDF30NNLO_Znunu_MAXHTPTV280_500_CVetoBVeto	e5308_s3126_r9364_r9315_p3736	47.4230	0.97	0.561	192.962
364152	Sherpa_221_NNPDF30NNLO_Znunu_MAXHTPTV280_500_CFilterBVeto	e5308_s3126_r9364_r9315_p3736	47.4010	0.97	0.265	271.367
364153	Sherpa_221_NNPDF30NNLO_Znunu_MAXHTPTV280_500_BFilter	e5308_s3126_r9364_r9315_p3736	47.4260	0.97	0.180	1064.574
364154	Sherpa_221_NNPDF30NNLO_Znunu_MAXHTPTV500_1000	e5308_s3126_r9364_r9315_p3736	9.9091	0.97	1.000	1037.390
364155	Sherpa_221_NNPDF30NNLO_Znunu_MAXHTPTV1000_E_CMS	e5308_s3126_r9364_r9315_p3736	0.8180	0.97	1.000	6283.377

Table F.6: $Z \to \nu\nu$ MC samples

Dataset ID	Process	Tags	$\sigma \times \epsilon$ [pb]	k-factor	Generator efficiency	$\mathcal{L}_{int}$[fb^{-1}]
407342	PhPy8EG_A14_ttbarHT1k5_hdamp258p75_nonallhad	e6414_e5984_s3126_r9364_r9315_p3736	729.7700	1.14	0.001	3894.816
407343	PhPy8EG_A14_ttbarHT1k_1k5_hdamp258p75_nonallhad	e6414_e5984_s3126_r9364_r9315_p3736	729.7700	1.14	0.004	2705.251
407344	PhPy8EG_A14_ttbarHT6c_1k_hdamp258p75_nonallhad	e6414_e5984_s3126_r9364_r9315_p3736	729.7700	1.14	0.026	469.026
407345	PhPy8EG_A14_ttbarMET200_300_hdamp258p75_nonallhad	e6414_e5984_s3126_r9364_r9315_p3736	729.7700	1.14	0.008	2493.731
407346	PhPy8EG_A14_ttbarMET300_400_hdamp258p75_nonallhad	e6414_e5984_s3126_r9364_r9315_p3736	729.7700	1.14	0.001	3229.423
407347	PhPy8EG_A14_ttbarMET400_hdamp258p75_nonallhad	e6414_e5984_s3126_r9364_r9315_p3736	729.7700	1.14	0.000	7611.939
410470	PhPy8EG_A14_ttbar_hdamp258p75_nonallhad	e6337_e5984_s3126_r9364_r9315_p3736	729.7600	1.14	0.544	264.028
410471	PhPy8EG_A14_ttbar_hdamp258p75_allhad	e6337_e5984_s3126_r9364_r9315_p3736	729.7700	1.14	0.456	105.107

Table F.7: $t\bar{t}$ MC Samples

Dataset ID	Process	Tags	$\sigma \times \epsilon$ [pb]	k-factor	Generator efficiency	$\mathcal{L}_{int}$[fb^{-1}]
345705	Sherpa_222_NNPDF30NNLO_gglll_0M4l130	e6213_e5984_s3126_r9364_r9315_p3736	0.0100	1.00	1.000	10042.479
345706	Sherpa_222_NNPDF30NNLO_gglll_130M4l	e6213_e5984_s3126_r9364_r9315_p3736	0.0102	1.00	1.000	97313.789
345715	Sherpa_222_NNPDF30NNLO_ggllvvInt	e6525_e5984_s3126_r9364_r9315_p3736	0.2685	1.00	1.000	1117.318
345718	Sherpa_222_NNPDF30NNLO_ggllvvWW	e6525_e5984_s3126_r9364_r9315_p3736	0.4823	1.00	1.000	1036.699
345723	Sherpa_222_NNPDF30NNLO_ggllvvZZ	e6213_e5984_s3126_r9364_r9315_p3736	0.0071	1.00	1.000	14073.605
363355	Sherpa_221_NNPDF30NNLO_ZqqZvv	e5525_s3126_r9364_r9315_p3736	15.5610	1.00	0.277	1253.373
363356	Sherpa_221_NNPDF30NNLO_ZqqZll	e5525_s3126_r9364_r9315_p3736	15.5640	1.00	0.142	2450.590
363357	Sherpa_221_NNPDF30NNLO_WqqZvv	e5525_s3126_r9364_r9315_p3736	6.7975	1.00	1.000	882.677
363358	Sherpa_221_NNPDF30NNLO_WqqZll	e5525_s3126_r9364_r9315_p3736	3.4328	1.00	1.000	1573.060
363359	Sherpa_221_NNPDF30NNLO_WpqqWmlv	e5583_s3126_r9364_r9315_p3736	24.7080	1.00	1.000	291.161
363360	Sherpa_221_NNPDF30NNLO_WplvWmqq	e5983_s3126_r9364_r9315_p3736	24.7240	1.00	1.000	290.730
363494	Sherpa_221_NNPDF30NNLO_vvvv	e5332_s3126_r9364_r9315_p3736	0.6029	1.00	1.000	4974.043
364250	Sherpa_222_NNPDF30NNLO_llll	e5894_s3126_r9364_r9315_p3736	1.2523	1.00	1.000	14248.104
364253	Sherpa_222_NNPDF30NNLO_lllv	e5916_s3126_r9364_r9315_p3736	4.5790	1.00	1.000	3393.295
364254	Sherpa_222_NNPDF30NNLO_llvv	e5916_s3126_r9364_r9315_p3736	12.5010	1.00	1.000	1199.584
364255	Sherpa_222_NNPDF30NNLO_lvvv	e5916_s3126_r9364_r9315_p3736	3.2344	1.00	1.000	1854.749
364283	Sherpa_222_NNPDF30NNLO_llljj_EW6	e6055_e5984_s3126_r9364_r9315_p3736	0.0105	1.00	1.000	28440.018
364284	Sherpa_222_NNPDF30NNLO_lllvjj_EW6	e6055_e5984_s3126_r9364_r9315_p3736	0.0471	1.00	1.000	2124.676
364285	Sherpa_222_NNPDF30NNLO_llvvjj_EW6	e6055_e5984_s3126_r9364_r9315_p3736	0.1163	1.00	1.000	2578.038
364286	Sherpa_222_NNPDF30NNLO_llvvjj_ss_EW4	e6055_e5984_s3126_r9364_r9315_p3736	0.0252	1.00	1.000	39627.133
364287	Sherpa_222_NNPDF30NNLO_llvvjj_ss_EW6	e6055_e5984_s3126_r9364_r9315_p3736	0.0409	1.00	1.000	2447.741
364302	Sherpa_222_NNPDF30NNLO_ggZllZqq	e6273_e5984_s3126_r9364_r9315_p3736	0.9233	1.00	0.142	1905.071
364303	Sherpa_222_NNPDF30NNLO_ggZvvZqq	e6273_e5984_s3126_r9364_r9315_p3736	0.9249	1.00	0.280	959.045
364304	Sherpa_222_NNPDF30NNLO_ggWmlvWpqq	e6273_e5984_s3126_r9364_r9315_p3736	0.6219	1.00	1.000	527.382
364305	Sherpa_222_NNPDF30NNLO_ggWplvWmqq	e6273_e5984_s3126_r9364_r9315_p3736	0.6219	1.00	1.000	562.828

Table F.8: Diboson MC samples

Dataset ID	Process	Tags	$\sigma \times \epsilon$ [pb]	k-factor	Generator efficiency	$\mathcal{L}_{int}$[fb^{-1}]
2669	physics_Main	r9264_p3083_p3850	-1.0000	-1.00	-1.000	-1.000
2669	physics_Main	r9264_p3083_p3850	-1.0000	-1.00	-1.000	-1.000
2670	physics_Main	r9264_p3083_p3850	-1.0000	-1.00	-1.000	-1.000
2671	physics_Main	r9264_p3083_p3850	-1.0000	-1.00	-1.000	-1.000
2671	physics_Main	r9264_p3083_p3850	-1.0000	-1.00	-1.000	-1.000
2671	physics_Main	r9264_p3083_p3850	-1.0000	-1.00	-1.000	-1.000
2676	physics_Main	r9264_p3083_p3850	-1.0000	-1.00	-1.000	-1.000
2676	physics_Main	r9264_p3083_p3850	-1.0000	-1.00	-1.000	-1.000
2704	physics_Main	r9264_p3083_p3850	-1.0000	-1.00	-1.000	-1.000
2704	physics_Main	r9264_p3083_p3850	-1.0000	-1.00	-1.000	-1.000
2705	physics_Main	r9264_p3083_p3850	-1.0000	-1.00	-1.000	-1.000
2708	physics_Main	r9264_p3083_p3850	-1.0000	-1.00	-1.000	-1.000
2708	physics_Main	r9264_p3083_p3850	-1.0000	-1.00	-1.000	-1.000
2709	physics_Main	r9264_p3083_p3850	-1.0000	-1.00	-1.000	-1.000
2709	physics_Main	r9264_p3083_p3850	-1.0000	-1.00	-1.000	-1.000
2710	physics_Main	r9264_p3083_p3850	-1.0000	-1.00	-1.000	-1.000
2712	physics_Main	r9264_p3083_p3850	-1.0000	-1.00	-1.000	-1.000
2713	physics_Main	r9264_p3083_p3850	-1.0000	-1.00	-1.000	-1.000
2714	physics_Main	r9264_p3083_p3850	-1.0000	-1.00	-1.000	-1.000
2715	physics_Main	r9264_p3083_p3850	-1.0000	-1.00	-1.000	-1.000
2715	physics_Main	r9264_p3083_p3850	-1.0000	-1.00	-1.000	-1.000
2717	physics_Main	r9264_p3083_p3850	-1.0000	-1.00	-1.000	-1.000
2760	physics_Main	r9264_p3083_p3850	-1.0000	-1.00	-1.000	-1.000
2761	physics_Main	r9264_p3083_p3850	-1.0000	-1.00	-1.000	-1.000
2761	physics_Main	r9264_p3083_p3850	-1.0000	-1.00	-1.000	-1.000
2761	physics_Main	r9412_p3083_p3850	-1.0000	-1.00	-1.000	-1.000
2761	physics_Main	r9412_p3083_p3850	-1.0000	-1.00	-1.000	-1.000
2761	physics_Main	r9264_p3083_p3850	-1.0000	-1.00	-1.000	-1.000
2761	physics_Main	r9264_p3083_p3850	-1.0000	-1.00	-1.000	-1.000
2762	physics_Main	r9264_p3083_p3850	-1.0000	-1.00	-1.000	-1.000
2762	physics_Main	r9264_p3083_p3850	-1.0000	-1.00	-1.000	-1.000
2763	physics_Main	r9264_p3083_p3850	-1.0000	-1.00	-1.000	-1.000
2763	physics_Main	r9264_p3083_p3850	-1.0000	-1.00	-1.000	-1.000
2763	physics_Main	r9264_p3083_p3850	-1.0000	-1.00	-1.000	-1.000
2764	physics_Main	r9264_p3083_p3850	-1.0000	-1.00	-1.000	-1.000
2765	physics_Main	r9264_p3083_p3850	-1.0000	-1.00	-1.000	-1.000
2766	physics_Main	r9264_p3083_p3850	-1.0000	-1.00	-1.000	-1.000

Table F.9: Data samples 1

Dataset ID	Process	Tags	$\sigma \times \epsilon$ [pb]	k-factor	Generator efficiency	$\mathcal{L}_{int}$[fb^{-1}]
2767	physics_Main	r9264_p3083_p3850	-1.0000	-1.00	-1.000	-1.000
2767	physics_Main	r9264_p3083_p3850	-1.0000	-1.00	-1.000	-1.000
2767	physics_Main	r9264_p3083_p3850	-1.0000	-1.00	-1.000	-1.000
2769	physics_Main	r9264_p3083_p3850	-1.0000	-1.00	-1.000	-1.000
2769	physics_Main	r9264_p3083_p3850	-1.0000	-1.00	-1.000	-1.000
2787	physics_Main	r9264_p3083_p3850	-1.0000	-1.00	-1.000	-1.000
2787	physics_Main	r9264_p3083_p3850	-1.0000	-1.00	-1.000	-1.000
2788	physics_Main	r9264_p3083_p3850	-1.0000	-1.00	-1.000	-1.000
2789	physics_Main	r9264_p3083_p3850	-1.0000	-1.00	-1.000	-1.000
2789	physics_Main	r9264_p3083_p3850	-1.0000	-1.00	-1.000	-1.000
2789	physics_Main	r9264_p3083_p3850	-1.0000	-1.00	-1.000	-1.000
2789	physics_Main	r9264_p3083_p3850	-1.0000	-1.00	-1.000	-1.000
2791	physics_Main	r9264_p3083_p3850	-1.0000	-1.00	-1.000	-1.000
2792	physics_Main	r9264_p3083_p3850	-1.0000	-1.00	-1.000	-1.000
2792	physics_Main	r9264_p3083_p3850	-1.0000	-1.00	-1.000	-1.000
2792	physics_Main	r9264_p3083_p3850	-1.0000	-1.00	-1.000	-1.000
2793	physics_Main	r9264_p3083_p3850	-1.0000	-1.00	-1.000	-1.000
2795	physics_Main	r9264_p3083_p3850	-1.0000	-1.00	-1.000	-1.000
2795	physics_Main	r9264_p3083_p3850	-1.0000	-1.00	-1.000	-1.000
2796	physics_Main	r9264_p3083_p3850	-1.0000	-1.00	-1.000	-1.000
2797	physics_Main	r9264_p3083_p3850	-1.0000	-1.00	-1.000	-1.000
2798	physics_Main	r9264_p3083_p3850	-1.0000	-1.00	-1.000	-1.000
2798	physics_Main	r9264_p3083_p3850	-1.0000	-1.00	-1.000	-1.000
2799	physics_Main	r9264_p3083_p3850	-1.0000	-1.00	-1.000	-1.000
2799	physics_Main	r9264_p3083_p3850	-1.0000	-1.00	-1.000	-1.000
2799	physics_Main	r9264_p3083_p3850	-1.0000	-1.00	-1.000	-1.000
2802	physics_Main	r9264_p3083_p3850	-1.0000	-1.00	-1.000	-1.000
2802	physics_Main	r9264_p3083_p3850	-1.0000	-1.00	-1.000	-1.000
2803	physics_Main	r9264_p3083_p3850	-1.0000	-1.00	-1.000	-1.000
2803	physics_Main	r9264_p3083_p3850	-1.0000	-1.00	-1.000	-1.000
2804	physics_Main	r9264_p3083_p3850	-1.0000	-1.00	-1.000	-1.000
2804	physics_Main	r9264_p3083_p3850	-1.0000	-1.00	-1.000	-1.000
2805	physics_Main	r9264_p3083_p3850	-1.0000	-1.00	-1.000	-1.000
2805	physics_Main	r9264_p3083_p3850	-1.0000	-1.00	-1.000	-1.000
2806	physics_Main	r9264_p3083_p3850	-1.0000	-1.00	-1.000	-1.000
2806	physics_Main	r9264_p3083_p3850	-1.0000	-1.00	-1.000	-1.000
2807	physics_Main	r9264_p3083_p3850	-1.0000	-1.00	-1.000	-1.000

Table F.10: Data Samples 2

Dataset ID	Process	Tags	$\sigma \times \epsilon$ [pb]	k-factor	Generator efficiency	$\mathcal{L}_{int}$[fb^{-1}]
2808	physics_Main	r9264_p3083_p3850	-1.0000	-1.00	-1.000	-1.000
2808	physics_Main	r9264_p3083_p3850	-1.0000	-1.00	-1.000	-1.000
2809	physics_Main	r9264_p3083_p3850	-1.0000	-1.00	-1.000	-1.000
2809	physics_Main	r9264_p3083_p3850	-1.0000	-1.00	-1.000	-1.000
2810	physics_Main	r9264_p3083_p3850	-1.0000	-1.00	-1.000	-1.000
2810	physics_Main	r9264_p3083_p3850	-1.0000	-1.00	-1.000	-1.000
2810	physics_Main	r9264_p3083_p3850	-1.0000	-1.00	-1.000	-1.000
2811	physics_Main	r9264_p3083_p3850	-1.0000	-1.00	-1.000	-1.000
2811	physics_Main	r9264_p3083_p3850	-1.0000	-1.00	-1.000	-1.000
2813	physics_Main	r9264_p3083_p3850	-1.0000	-1.00	-1.000	-1.000
2813	physics_Main	r9264_p3083_p3850	-1.0000	-1.00	-1.000	-1.000
2813	physics_Main	r9264_p3083_p3850	-1.0000	-1.00	-1.000	-1.000
2814	physics_Main	r9264_p3083_p3850	-1.0000	-1.00	-1.000	-1.000
2826	physics_Main	r9264_p3083_p3850	-1.0000	-1.00	-1.000	-1.000
2826	physics_Main	r9264_p3083_p3850	-1.0000	-1.00	-1.000	-1.000
2827	physics_Main	r9264_p3083_p3850	-1.0000	-1.00	-1.000	-1.000
2827	physics_Main	r9264_p3083_p3850	-1.0000	-1.00	-1.000	-1.000
2829	physics_Main	r9264_p3083_p3850	-1.0000	-1.00	-1.000	-1.000
2830	physics_Main	r9264_p3083_p3850	-1.0000	-1.00	-1.000	-1.000
2832	physics_Main	r9264_p3083_p3850	-1.0000	-1.00	-1.000	-1.000
2834	physics_Main	r9264_p3083_p3850	-1.0000	-1.00	-1.000	-1.000
2836	physics_Main	r9264_p3083_p3850	-1.0000	-1.00	-1.000	-1.000
2837	physics_Main	r9264_p3083_p3850	-1.0000	-1.00	-1.000	-1.000
2840	physics_Main	r9264_p3083_p3850	-1.0000	-1.00	-1.000	-1.000
2841	physics_Main	r9264_p3083_p3850	-1.0000	-1.00	-1.000	-1.000
2842	physics_Main	r9264_p3083_p3850	-1.0000	-1.00	-1.000	-1.000
2842	physics_Main	r9264_p3083_p3850	-1.0000	-1.00	-1.000	-1.000
2844	physics_Main	r9264_p3083_p3850	-1.0000	-1.00	-1.000	-1.000
2844	physics_Main	r9264_p3083_p3850	-1.0000	-1.00	-1.000	-1.000
2844	physics_Main	r9264_p3083_p3850	-1.0000	-1.00	-1.000	-1.000
2844	physics_Main	r9264_p3083_p3850	-1.0000	-1.00	-1.000	-1.000
2977	physics_Main	r9264_p3083_p3850	-1.0000	-1.00	-1.000	-1.000
2985	physics_Main	r9264_p3083_p3850	-1.0000	-1.00	-1.000	-1.000
2986	physics_Main	r9264_p3083_p3850	-1.0000	-1.00	-1.000	-1.000
2986	physics_Main	r9264_p3083_p3850	-1.0000	-1.00	-1.000	-1.000
2986	physics_Main	r9264_p3083_p3850	-1.0000	-1.00	-1.000	-1.000
2986	physics_Main	r9264_p3083_p3850	-1.0000	-1.00	-1.000	-1.000

Table F.11: Data Samples 3

Dataset ID	Process	Tags	$\sigma \times \epsilon$ [pb]	k-factor	Generator efficiency	$\mathcal{L}_{int}$[fb^{-1}]
2987	physics_Main	r9264_p3083_p3850	-1.0000	-1.00	-1.000	-1.000
2987	physics_Main	r9264_p3083_p3850	-1.0000	-1.00	-1.000	-1.000
2988	physics_Main	r9264_p3083_p3850	-1.0000	-1.00	-1.000	-1.000
2989	physics_Main	r9264_p3083_p3850	-1.0000	-1.00	-1.000	-1.000
2990	physics_Main	r9264_p3083_p3850	-1.0000	-1.00	-1.000	-1.000
2991	physics_Main	r9264_p3083_p3850	-1.0000	-1.00	-1.000	-1.000
2991	physics_Main	r9264_p3083_p3850	-1.0000	-1.00	-1.000	-1.000
2991	physics_Main	r9264_p3083_p3850	-1.0000	-1.00	-1.000	-1.000
2992	physics_Main	r9264_p3083_p3850	-1.0000	-1.00	-1.000	-1.000
2992	physics_Main	r9264_p3083_p3850	-1.0000	-1.00	-1.000	-1.000
2992	physics_Main	r9264_p3083_p3850	-1.0000	-1.00	-1.000	-1.000
2993	physics_Main	r9264_p3083_p3850	-1.0000	-1.00	-1.000	-1.000
2995	physics_Main	r9264_p3083_p3850	-1.0000	-1.00	-1.000	-1.000
3002	physics_Main	r9264_p3083_p3850	-1.0000	-1.00	-1.000	-1.000
3003	physics_Main	r9264_p3083_p3850	-1.0000	-1.00	-1.000	-1.000
3004	physics_Main	r9264_p3083_p3850	-1.0000	-1.00	-1.000	-1.000
3004	physics_Main	r9264_p3083_p3850	-1.0000	-1.00	-1.000	-1.000
3004	physics_Main	r9264_p3083_p3850	-1.0000	-1.00	-1.000	-1.000
3005	physics_Main	r9264_p3083_p3850	-1.0000	-1.00	-1.000	-1.000
3005	physics_Main	r9264_p3083_p3850	-1.0000	-1.00	-1.000	-1.000
3006	physics_Main	r9264_p3083_p3850	-1.0000	-1.00	-1.000	-1.000
3006	physics_Main	r9264_p3083_p3850	-1.0000	-1.00	-1.000	-1.000
3006	physics_Main	r9264_p3083_p3850	-1.0000	-1.00	-1.000	-1.000
3007	physics_Main	r9264_p3083_p3850	-1.0000	-1.00	-1.000	-1.000
3008	physics_Main	r9264_p3083_p3850	-1.0000	-1.00	-1.000	-1.000
3008	physics_Main	r9264_p3083_p3850	-1.0000	-1.00	-1.000	-1.000
3009	physics_Main	r9264_p3083_p3850	-1.0000	-1.00	-1.000	-1.000
3019	physics_Main	r9264_p3083_p3850	-1.0000	-1.00	-1.000	-1.000
3019	physics_Main	r9264_p3083_p3850	-1.0000	-1.00	-1.000	-1.000
3019	physics_Main	r9264_p3083_p3850	-1.0000	-1.00	-1.000	-1.000
3019	physics_Main	r9264_p3083_p3850	-1.0000	-1.00	-1.000	-1.000
3019	physics_Main	r9264_p3083_p3850	-1.0000	-1.00	-1.000	-1.000
3020	physics_Main	r9264_p3083_p3850	-1.0000	-1.00	-1.000	-1.000
3021	physics_Main	r9264_p3083_p3850	-1.0000	-1.00	-1.000	-1.000
3022	physics_Main	r9264_p3083_p3850	-1.0000	-1.00	-1.000	-1.000
3022	physics_Main	r9264_p3083_p3850	-1.0000	-1.00	-1.000	-1.000

Table F.12: Data Samples 4

Dataset ID	Process	Tags	$\sigma \times \epsilon$ [pb]	k-factor	Generator efficiency	$\mathcal{L}_{int}$[fb^{-1}]
3023	physics_Main	r9264_p3083_p3850	-1.0000	-1.00	-1.000	-1.000
3023	physics_Main	r9264_p3083_p3850	-1.0000	-1.00	-1.000	-1.000
3023	physics_Main	r9264_p3083_p3850	-1.0000	-1.00	-1.000	-1.000
3023	physics_Main	r9264_p3083_p3850	-1.0000	-1.00	-1.000	-1.000
3023	physics_Main	r9264_p3083_p3850	-1.0000	-1.00	-1.000	-1.000
3027	physics_Main	r9264_p3083_p3850	-1.0000	-1.00	-1.000	-1.000
3028	physics_Main	r9264_p3083_p3850	-1.0000	-1.00	-1.000	-1.000
3028	physics_Main	r9264_p3083_p3850	-1.0000	-1.00	-1.000	-1.000
3028	physics_Main	r9264_p3083_p3850	-1.0000	-1.00	-1.000	-1.000
3029	physics_Main	r9264_p3083_p3850	-1.0000	-1.00	-1.000	-1.000
3029	physics_Main	r9264_p3083_p3850	-1.0000	-1.00	-1.000	-1.000
3029	physics_Main	r9264_p3083_p3850	-1.0000	-1.00	-1.000	-1.000
3030	physics_Main	r9264_p3083_p3850	-1.0000	-1.00	-1.000	-1.000
3030	physics_Main	r9264_p3083_p3850	-1.0000	-1.00	-1.000	-1.000
3030	physics_Main	r9264_p3083_p3850	-1.0000	-1.00	-1.000	-1.000
3032	physics_Main	r9264_p3083_p3850	-1.0000	-1.00	-1.000	-1.000
3032	physics_Main	r9264_p3083_p3850	-1.0000	-1.00	-1.000	-1.000
3032	physics_Main	r9264_p3083_p3850	-1.0000	-1.00	-1.000	-1.000
3032	physics_Main	r9264_p3083_p3850	-1.0000	-1.00	-1.000	-1.000
3032	physics_Main	r9264_p3083_p3850	-1.0000	-1.00	-1.000	-1.000
3033	physics_Main	r9264_p3083_p3850	-1.0000	-1.00	-1.000	-1.000
3033	physics_Main	r9264_p3083_p3850	-1.0000	-1.00	-1.000	-1.000
3034	physics_Main	r9264_p3083_p3850	-1.0000	-1.00	-1.000	-1.000
3034	physics_Main	r9264_p3083_p3850	-1.0000	-1.00	-1.000	-1.000
3035	physics_Main	r9264_p3083_p3850	-1.0000	-1.00	-1.000	-1.000
3036	physics_Main	r9264_p3083_p3850	-1.0000	-1.00	-1.000	-1.000
3038	physics_Main	r9264_p3083_p3850	-1.0000	-1.00	-1.000	-1.000
3038	physics_Main	r9264_p3083_p3850	-1.0000	-1.00	-1.000	-1.000
3039	physics_Main	r9264_p3083_p3850	-1.0000	-1.00	-1.000	-1.000
3040	physics_Main	r9264_p3083_p3850	-1.0000	-1.00	-1.000	-1.000
3040	physics_Main	r9264_p3083_p3850	-1.0000	-1.00	-1.000	-1.000
3041	physics_Main	r9264_p3083_p3850	-1.0000	-1.00	-1.000	-1.000
3041	physics_Main	r9264_p3083_p3850	-1.0000	-1.00	-1.000	-1.000
3041	physics_Main	r9264_p3083_p3850	-1.0000	-1.00	-1.000	-1.000
3042	physics_Main	r9264_p3083_p3850	-1.0000	-1.00	-1.000	-1.000
3042	physics_Main	r9264_p3083_p3850	-1.0000	-1.00	-1.000	-1.000

Table F.13: Data Samples 5

Dataset ID	Process	Tags	$\sigma \times \epsilon$ [pb]	k-factor	Generator efficiency	$\mathcal{L}_{int}$[fb^{-1}]
3043	physics_Main	r9264_p3083_p3850	-1.0000	-1.00	-1.000	-1.000
3043	physics_Main	r9264_p3083_p3850	-1.0000	-1.00	-1.000	-1.000
3044	physics_Main	r9264_p3083_p3850	-1.0000	-1.00	-1.000	-1.000
3044	physics_Main	r9264_p3083_p3850	-1.0000	-1.00	-1.000	-1.000
3044	physics_Main	r9264_p3083_p3850	-1.0000	-1.00	-1.000	-1.000
3053	physics_Main	r9264_p3083_p3850	-1.0000	-1.00	-1.000	-1.000
3055	physics_Main	r9264_p3083_p3850	-1.0000	-1.00	-1.000	-1.000
3055	physics_Main	r9264_p3083_p3850	-1.0000	-1.00	-1.000	-1.000
3056	physics_Main	r9264_p3083_p3850	-1.0000	-1.00	-1.000	-1.000
3056	physics_Main	r9264_p3083_p3850	-1.0000	-1.00	-1.000	-1.000
3056	physics_Main	r9264_p3083_p3850	-1.0000	-1.00	-1.000	-1.000
3057	physics_Main	r9264_p3083_p3850	-1.0000	-1.00	-1.000	-1.000
3057	physics_Main	r9264_p3083_p3850	-1.0000	-1.00	-1.000	-1.000
3057	physics_Main	r9264_p3083_p3850	-1.0000	-1.00	-1.000	-1.000
3057	physics_Main	r9264_p3083_p3850	-1.0000	-1.00	-1.000	-1.000
3058	physics_Main	r9264_p3083_p3850	-1.0000	-1.00	-1.000	-1.000
3059	physics_Main	r9264_p3083_p3850	-1.0000	-1.00	-1.000	-1.000
3062	physics_Main	r9264_p3083_p3850	-1.0000	-1.00	-1.000	-1.000
3062	physics_Main	r9264_p3083_p3850	-1.0000	-1.00	-1.000	-1.000
3063	physics_Main	r9264_p3083_p3850	-1.0000	-1.00	-1.000	-1.000
3063	physics_Main	r9264_p3083_p3850	-1.0000	-1.00	-1.000	-1.000
3064	physics_Main	r9264_p3083_p3850	-1.0000	-1.00	-1.000	-1.000
3064	physics_Main	r9264_p3083_p3850	-1.0000	-1.00	-1.000	-1.000
3064	physics_Main	r9264_p3083_p3850	-1.0000	-1.00	-1.000	-1.000
3064	physics_Main	r9264_p3083_p3850	-1.0000	-1.00	-1.000	-1.000
3071	physics_Main	r9264_p3083_p3850	-1.0000	-1.00	-1.000	-1.000
3071	physics_Main	r9264_p3083_p3850	-1.0000	-1.00	-1.000	-1.000
3072	physics_Main	r9264_p3083_p3850	-1.0000	-1.00	-1.000	-1.000
3073	physics_Main	r9264_p3083_p3850	-1.0000	-1.00	-1.000	-1.000
3073	physics_Main	r9264_p3083_p3850	-1.0000	-1.00	-1.000	-1.000
3073	physics_Main	r9264_p3083_p3850	-1.0000	-1.00	-1.000	-1.000
3073	physics_Main	r9264_p3083_p3850	-1.0000	-1.00	-1.000	-1.000
3074	physics_Main	r9264_p3083_p3850	-1.0000	-1.00	-1.000	-1.000
3075	physics_Main	r9264_p3083_p3850	-1.0000	-1.00	-1.000	-1.000
3075	physics_Main	r9264_p3083_p3850	-1.0000	-1.00	-1.000	-1.000
3075	physics_Main	r9264_p3083_p3850	-1.0000	-1.00	-1.000	-1.000

Table F.14: Data Samples 6

Dataset ID	Process	Tags	$\sigma \times \epsilon$ [pb]	k-factor	Generator efficiency	$\mathcal{L}_{int}$[fb^{-1}]
3076	physics_Main	r9264_p3083_p3850	-1.0000	-1.00	-1.000	-1.000
3076	physics_Main	r9264_p3083_p3850	-1.0000	-1.00	-1.000	-1.000
3076	physics_Main	r9264_p3083_p3850	-1.0000	-1.00	-1.000	-1.000
3077	physics_Main	r9264_p3083_p3850	-1.0000	-1.00	-1.000	-1.000
3077	physics_Main	r9264_p3083_p3850	-1.0000	-1.00	-1.000	-1.000
3077	physics_Main	r9264_p3083_p3850	-1.0000	-1.00	-1.000	-1.000
3078	physics_Main	r9264_p3083_p3850	-1.0000	-1.00	-1.000	-1.000
3079	physics_Main	r9264_p3083_p3850	-1.0000	-1.00	-1.000	-1.000
3080	physics_Main	r9264_p3083_p3850	-1.0000	-1.00	-1.000	-1.000
3080	physics_Main	r9264_p3083_p3850	-1.0000	-1.00	-1.000	-1.000
3093	physics_Main	r9264_p3083_p3850	-1.0000	-1.00	-1.000	-1.000
3093	physics_Main	r9264_p3083_p3850	-1.0000	-1.00	-1.000	-1.000
3094	physics_Main	r9264_p3083_p3850	-1.0000	-1.00	-1.000	-1.000
3095	physics_Main	r9264_p3083_p3850	-1.0000	-1.00	-1.000	-1.000
3096	physics_Main	r9264_p3083_p3850	-1.0000	-1.00	-1.000	-1.000
3096	physics_Main	r9264_p3083_p3850	-1.0000	-1.00	-1.000	-1.000
3097	physics_Main	r9264_p3083_p3850	-1.0000	-1.00	-1.000	-1.000
3100	physics_Main	r9264_p3083_p3850	-1.0000	-1.00	-1.000	-1.000
3102	physics_Main	r9264_p3083_p3850	-1.0000	-1.00	-1.000	-1.000
3102	physics_Main	r9264_p3083_p3850	-1.0000	-1.00	-1.000	-1.000
3103	physics_Main	r9264_p3083_p3850	-1.0000	-1.00	-1.000	-1.000
3103	physics_Main	r9264_p3083_p3850	-1.0000	-1.00	-1.000	-1.000
3104	physics_Main	r9264_p3083_p3850	-1.0000	-1.00	-1.000	-1.000
3104	physics_Main	r9264_p3083_p3850	-1.0000	-1.00	-1.000	-1.000
3104	physics_Main	r9264_p3083_p3850	-1.0000	-1.00	-1.000	-1.000
3106	physics_Main	r9264_p3083_p3850	-1.0000	-1.00	-1.000	-1.000
3106	physics_Main	r9264_p3083_p3850	-1.0000	-1.00	-1.000	-1.000
3107	physics_Main	r9264_p3083_p3850	-1.0000	-1.00	-1.000	-1.000
3108	physics_Main	r9264_p3083_p3850	-1.0000	-1.00	-1.000	-1.000
3108	physics_Main	r9264_p3083_p3850	-1.0000	-1.00	-1.000	-1.000
3108	physics_Main	r9264_p3083_p3850	-1.0000	-1.00	-1.000	-1.000
3109	physics_Main	r9264_p3083_p3850	-1.0000	-1.00	-1.000	-1.000
3110	physics_Main	r9264_p3083_p3850	-1.0000	-1.00	-1.000	-1.000
3111	physics_Main	r9264_p3083_p3850	-1.0000	-1.00	-1.000	-1.000
3112	physics_Main	r9264_p3083_p3850	-1.0000	-1.00	-1.000	-1.000

Table F.15: Data Samples 7

Dataset ID	Process	Tags	$\sigma \times \epsilon$ [pb]	k-factor	Generator efficiency	$\mathcal{L}_{int}$[fb^{-1}]
3112	physics_Main	r9264_p3083_p3850	-1.0000	-1.00	-1.000	-1.000
3113	physics_Main	r9264_p3083_p3850	-1.0000	-1.00	-1.000	-1.000
3113	physics_Main	r9264_p3083_p3850	-1.0000	-1.00	-1.000	-1.000
3114	physics_Main	r9264_p3083_p3850	-1.0000	-1.00	-1.000	-1.000
3114	physics_Main	r9264_p3083_p3850	-1.0000	-1.00	-1.000	-1.000
3114	physics_Main	r9264_p3083_p3850	-1.0000	-1.00	-1.000	-1.000

Table F.16: Data Samples 8